LIÈGE université
Sciences Appliquées

Nanoindentation for sub-miniaturized testing of irradiated materials: FEM analysis and experiments

A thesis submitted in partial fulfillment of the requirements
for the degree of Doctor of Philosophy (PhD) in Engineering Science

by

Tymofii KHVAN

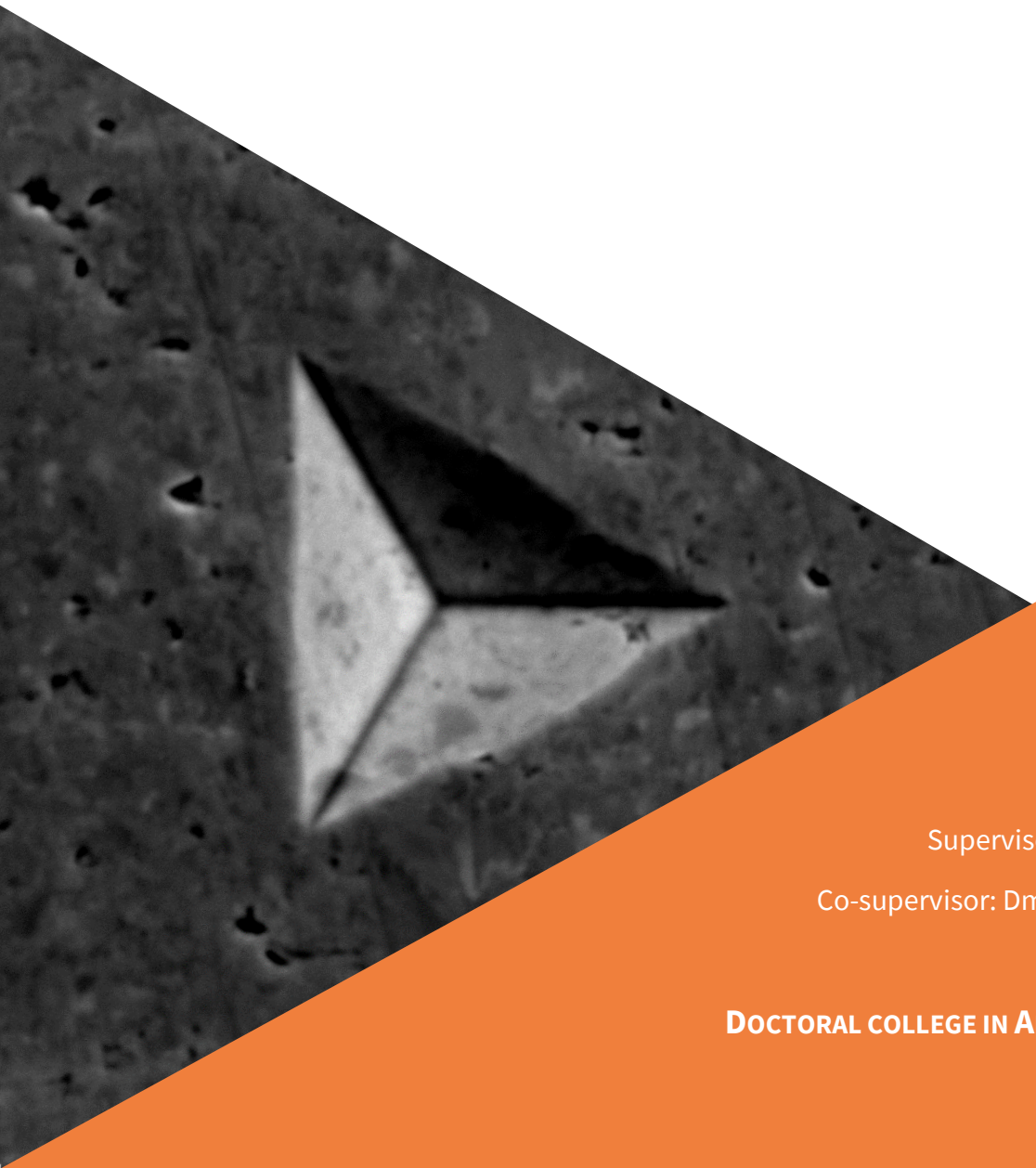

Supervisor: Ludovic NOELS (ULiège)

Co-supervisor: Dmitry TERENTYEV (SCK-CEN)

DOCTORAL COLLEGE IN AEROSPACE AND MECHANICS

OCTOBER 2023

This manuscript has been written with the help of the Writefull AI academic language tool for revising and correcting grammar, vocabulary, punctuation, spelling, and style of the text. As a non-native English speaker in the world of AI boom, I think it is meaningful to let such tools for our aid in daily tasks, especially if the purpose is to simplify life of the reader. Unless they are not used to generate the text from scratch, as in the given work.

More information about the tool can be found on writefull.com.

Tymofii Khvan

UNIVERSITY OF LIÈGE

Abstract

School of Engineering
Aerospace & Mechanical Engineering Department

Doctor in Engineering Sciences

Nanoindentation for sub-miniaturized testing of irradiated materials: FEM analysis and experiments

By Tymofii KHVAN

Materials chosen for the construction of structural components in nuclear reactors require careful selection and characterization, as their operational conditions presume the constant influence of harmful neutron irradiation and high temperatures. It inadvertently degrades the mechanical properties of the material and eventually may lead to the failure of the component. Therefore, we need to ensure that the margin of safety of a material is enough to sustain a certain amount of neutron damage. However, high-temperature neutron irradiation for research purposes is a very expensive, long, and complicated process, so the possibilities of imitating the damage of neutrons by other types of irradiation are of high interest. In this research, we set the goal to substitute complicated neutron irradiation with relatively cheap, fast, and safe (in terms of residual activity) ion irradiation, to analyze its impact on the mechanical properties, and to compare it with existing data done with neutrons. We aim to establish an experimentally computational procedure aimed at the effective characterization of the consequences of ion irradiation as a surrogate for neutron irradiation. This may significantly accelerate the delivery of new research data on structural materials for nuclear applications. The procedure is based on nanoindentation testing, as a highly informative technique to characterize the mechanical properties of materials on the nano-/microscale levels. It is highly useful in testing of thin subsurface regions with variative properties, which is the case for ion irradiation. The performed nanoindentation experiments are used to establish and validate the crystal plasticity finite element model that simulates the nanoindentation deformation process in pure α-iron (as a basic material with a "simple" microstructure) and Eurofer97 reduced activation ferritic/martensitic steel (as the reference material for future fusion and Gen IV reactors), while the latter is in the as-received and ion-irradiated states.

Within the project, both materials are experimentally characterized with macro-tensile and nanocompressive deformations; their microstructures are studied excessively using a variety of microscopy techniques. The data obtained are used to establish the constitutive laws of the materials to feed the nanoindentation FEM models. The correct set of the constitutive parameters confirmed experimentally allows us to semi-empirically link the nano-/microscale and macroscale deformations. Moreover, the radiation-modified material laws based on the tensile tests of neutron-irradiated Eurofer97 found in literature have shown a high accuracy in simulations of ion-irradiated material, which points to the interconnection of the two types of radiation-induced damage.

Globally, the execution of the proposed research is driven by the substantial complexities of using neutron irradiation for research purposes. The outcoming results are expected to pace the delivery of new research data in the field of nuclear materials and give rise to similar studies. The project shall also positively contribute to the stability of the European energy sector and the accessibility to future stable energy sources.

Acknowledgements

This doctoral thesis is the result of not only my dedication, but the joint efforts of many related people. I am infinitively grateful to everyone, regardless of whether their contribution resulted as a part of the presented research or was simply based on trust and mental support.

Definitely, the first gratitude must be addressed to my supervisors: Dr. Dmitry Terentyev and Prof. Ludovic Noels for their responsiveness, guidance, and objective assessment of my present skills and potential. I have learned a broad number of useful lessons from their professionalism, which will consequently become a core of my personality as a researcher. Special thanks to these outstanding scientists for understanding and patience, which they expressed during a terrible year-long period of my life, providing me with additional time and trust that I can gather my strength and accomplish this work.

I would also like to express my gratitude to all the members of the jury: Prof. Anne-Marie Habraken and Prof. Anne Mertens from the University of Liege; Prof. Thomas Pardoen from the Catholic University of Louvain; and Dr. Peter Hähner from JRC-Petten for dedicating time and efforts to read and review this work.

Many brilliant researchers have somehow directly contributed to this work, for which I want to thank: Dr. Wouter Van Renterghem, Dr. Andrii Dubinko, Dr. Aleksandr Zinovev, Chih-Cheng Chang, Olga Kachko – my former colleagues from SCK-CEN; Dr. Ude Hangen and Dr. Douglas Stauffer from Bruker Nano; Dr. Enrico Corniani from JRC-Petten; Dr. Frank Bergner from HZDR; Prof. Laurent Delannay from the Catholic University of Louvain.

Many thanks to the LHMA building of SCK-CEN, where I had the pleasure to work and share space with many wonderful and helpful people, so that from the office and lab activities to lunch or coffee breaks I could spend my time with enjoyment.

This project would not exist without the SCK-CEN Academy, the University of Liege Doctoral School, and the H2020 project M4F who established the idea, the concept, the funding, and the organization, for which I am very grateful.

And, of course, special thanks to my family and friends who had never uncrossed their fingers for me until the last step. For their trust and support, being far from the world of nuclear physics and material engineering, and just knowing inside that I can comprehend this success. A big thanks to my mother Svitlana and my father Volodymyr, who fairly consider my accomplishment as our common achievement, and never get tired of being proud.

I express my gratitude to several generations of Boeretang inhabitants who helped me to pass through these years living in an isolated community with joy. For one generation I am finishing Ph.D. being the last, for another being the first, but all of you became highly important to me and I will always be waiting for our next meeting.

All these directly and indirectly mentioned people made this Ph.D. journey happen, and if it was possible to split the degree into many pieces – everyone would deserve a small part.

Warsaw, October 2023
Tymofii Khvan

Contents

List of Figures

List of Tables

List of Acronyms

AFM - Atomic force microscope
BCC - Body-centered cubic
BSE - Backscattered electrons
CAD - Computer-aided design
CP - Crystal plasticity
CPFEM - Crystal plasticity finite element method
CRSS - Critical resolved shear stress
CSM - Continuous stiffness measurement
EBSD - Electron backscattered diffraction
EMC - Elastic modulus correction technique
DEMO - Demonstrative power plant
DPA - Displacement per atom
DSA - Dynamic strain aging
DT - Deuterium-tritium fusion reaction
FCC - Face-centered cubic
FEA - Finite element analysis
FEM - Finite element method
FIB - Focused ion beam
F/M - Ferritic/martensitic steel
GNDs - Geometrically necessary dislocations
HZDR - Helmholtz-Zentrum Dresden-Rossendorf
IPFZ - Inverse pole figure EBSD map with respect to *z* axis
ISE - Indentation size effect
ITER - International Thermonuclear Experimental Reactor
JET - Joint European Torus experimental fusion reactor
MD - Molecular dynamics simulations
NI - Nanoindentation
PAG - Prior austenite grain
PKA - Primary knock-on atom
TBM - Test blanket module
RAFM - Reduced activation ferritic/martensitic steel
RPV - Reactor pressure vessel
RT - Room temperature
SE - Secondary electrons
SEM - Scanning electron microscope
SRIM - Stopping Range of Ions in Matter software
SSDs - Statistically stored dislocations
TEM - Transmission electron microscope
UTS - Ultimate tensile stress

Chapter 1. Introduction

In this chapter, information about the global problem driving this research and a short overview of potential solutions will be given. The necessary information to understand minimal engineering and scientific aspects is covered, including a description of the subject of study. The second section outlines the features of the presented research. This part will be dedicated to the main objective of the thesis, the innovative methodology used, the introduced novelty, and the disseminated knowledge.

1.1 Context

Due to the improvement in average living standards, the increase in consumerism and, therefore, the production of goods, the lack of sufficient and effective "green" policies, the global energy demand increases steadily every day. This problem is amplified even more by the constant growth of the world population, as the number of users becomes higher. Therefore, in order to satisfy the growing energy demand, to stabilize it during global economic threats or to improve it in any means, we need to look towards new sources of clean, accessible and sustainable energy. This fact makes the future role of controlled nuclear fusion for commercial applications more and more meaningful.

Application of controlled nuclear fusion, the same reaction which powers our Sun and other stars in the Universe, as the alternative source of energy was proposed in the 1950s. It is based on the coalescence of light nuclei into heavier ones, releasing a relatively huge amount of energy as the result of the reaction. This process is opposite to the reaction that occurs in widely applicable modern fission reactors, which have been serving humanity since the middle of the twentieth century. Additionally, it is much more efficient (once considering the amount of energy normalized to a fuel mass). As only the lightest elements are used as the fuel for the fusion reaction (H, He, and their isotopes) nuclear fusion does not produce any long-term radioactive waste, and because of their high availability on our planet, it can be considered as a virtually unlimited source of energy.

The worldwide scientific community aims to build a fusion device that could provide a stable and commercially justified energy production. This ultimate goal consists of milestones, whereas the most significant ones can be connected with the construction of demonstrative and experimental fusion devices, namely, JET, ITER and DEMO. JET – the Joint European Torus, constructed in the UK in the early 1980s was the first device ever to achieve the controlled fusion reaction and is the most powerful of its kind nowadays. ITER, the International Thermonuclear Experimental Reactor, is being constructed these days in southern France and planned to be finished in late 2025. ITER is expected to overcome the fusion power obtained with JET in around 15 times; however, the crucial feature of this device is the ability to self-maintain, as the produced power will be high enough to exclude the external power sources required to keep the reaction stable. DEMO, or DEMOnstrative Power Plant, is the fusion device which will first introduce the commercial production levels of fusion energy, however, not earlier than in 2050s.

Many related scientific questions have yet to be answered. The most essential one in terms of nuclear materials science, including the presented thesis, is the careful selection of the structural materials to be applied in the construction of structural components and efficient and accurate characterization of their mechanical properties in harsh operational conditions. These operational conditions generally include thermomechanical cyclic stresses and high-energy neutron irradiation. Only a thorough approach to study material candidates affected by the listed

effects can confirm the operational stability of a structural component and, therefore, of a whole fusion device.

1.1.1 Nuclear Fusion

As was mentioned, nuclear fusion is the reaction based on the merging of two light nuclei into a heavier one with a release of energy. The concept is to bring two positively charged nuclei so close to each other that they will overcome the electrostatic barrier (Coulomb's repulsion) and let them act on the forces of strong interaction (intra-nuclear forces). To achieve this, the nuclei must have a huge kinetic energy, which is thermodynamically comparable to the interior of the Sun (~15 million K). A schematic representation of the fusion reaction is shown in Figure 1.

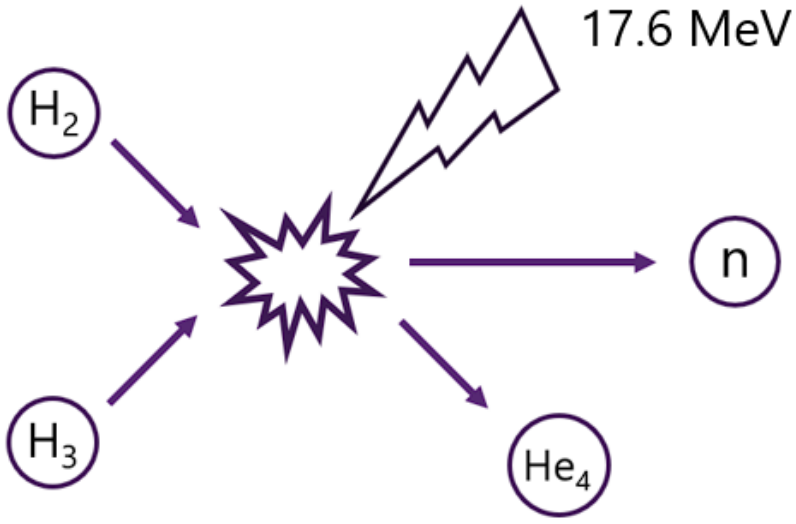

Figure 1. Model of a fusion reaction.

To make a nuclear fusion reaction happen, two nuclei must overcome Coulomb's repulsion and reach close to each other at $10^{-14} – 10^{-15}$ m. As the Coulomb barrier increases with the charge of a nucleus, the selection of practically possible fusion reactions is limited to the use of the lightest ones: isotopes of hydrogen, lithium, and helium. Even so, there are many types of nuclei combinations that exist. The most favorable for controlled fusion is the reaction between deuterium and tritium (DT) as it has the highest cross-section, as can be seen in Figure 2. A magnitude of the cross-section basically describes the probability of a nuclear reaction: the higher the cross-section, the more probable for the reaction to occur.

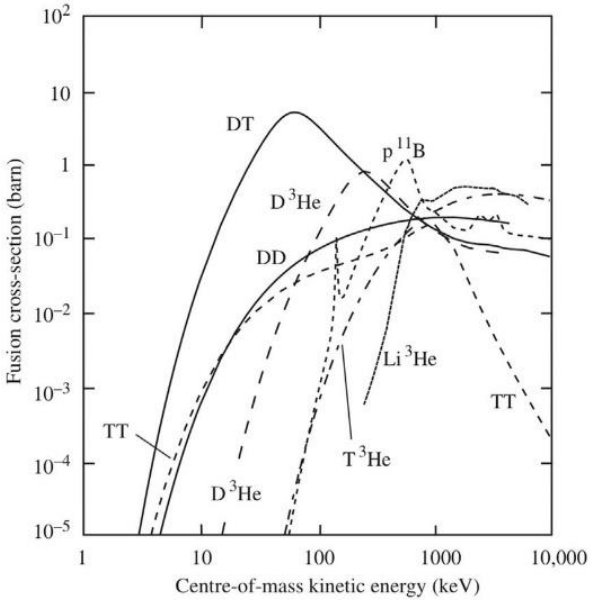

Figure 2. Cross-sections for various fusion reactions; Reprinted from EPJ Web of Conferences, 98 (2015), Ongena J., "Fusion: A true challenge for an enormous reward", licensed under CC BY 4.0 [1].

The DT reaction is expressed as follows:

$$T(^3_1H) + D(^2_1H) \rightarrow {}^4_2He + {}^1_0n + 17.6\,MeV \quad (1.1)$$

One of the fuel components, deuterium, is naturally present in seawater in virtually unlimited amounts. Another one, tritium, is unstable and must be produced artificially. A commercial fusion power plant presumes the use of a special concept called a tritium breeding blanket. It is a secondary lithium-containing layer of the plasma chamber where the fusion reaction occurs. Neutrons produced by the reaction will interact with lithium-producing tritium according to one of the following relations:

$$^7_3Li + {}^1_0n \rightarrow {}^4_2He + {}^3_1T + {}^1_0n - 2.47\,MeV \quad (1.2)$$

$$^6_3Li + {}^1_0n \rightarrow {}^4_2He + {}^3_1T + 4.8\,MeV \quad (1.3)$$

1.1.2 Tritium breeding

Major objectives of ITER include the development and testing of essential technologies necessary for the stable and safe employment of a fusion device. Moreover, many potential concepts for the same solution are being developed by different countries-ITER project members. They will be applied simultaneously or separately during the ITER operational regime, and consequently their efficiency will be analyzed to establish the understanding on the further applicability. A good example of such a case is the variety of concepts of tritium feed to fuel the fusion reaction. Thus, utilizing ITER different concepts of tritium breeding blankets under the form of Test Blanket Modules (TBMs) will be tested to find the best solution on tritium self-supply.

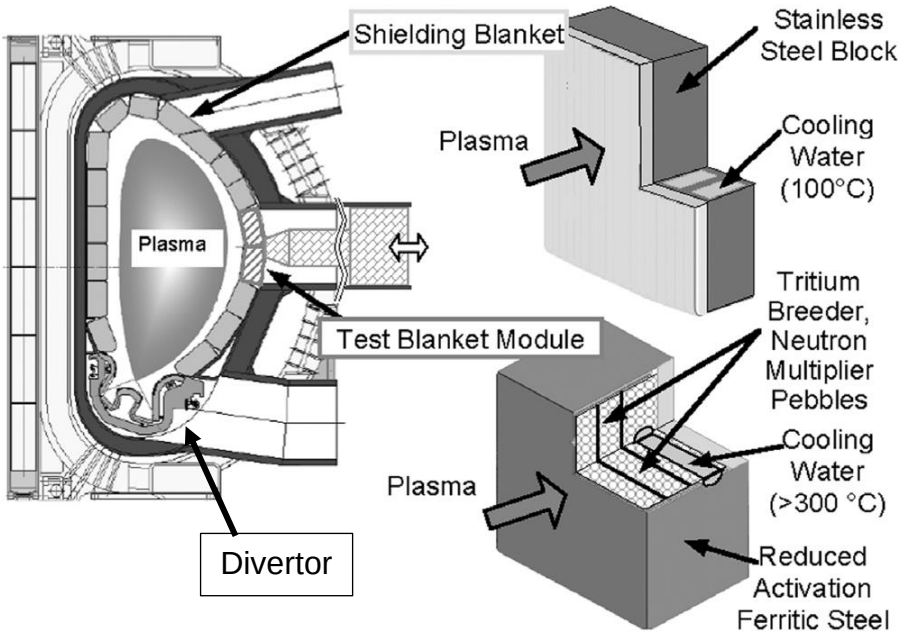

Figure 3. Structure and location of TBM inside the plasma chamber of ITER; Reprinted from Nuclear Fusion, 57(9), 092014 (2017), Konishi S., Enoeda M., Nakamichi M., Hoshino T. Ying A., Sharafat S., Smolentsev S., "Functional materials for breeding blankets – status and developments", with permission from the IAEA / Divertor indication added to the original [2].

Figure 3 shows the composition of the plasma chamber of ITER. It mainly consists of a divertor, 440 shielding Blanket Modules and 4 more complex Test Blanket Modules containing lithium. The design of shielding Blanket Modules is relatively simple, as they are made of two main components: the First Wall plasma-facing panels made of beryllium and steel Shield Blocks designed to provide the connections for the supply of cooling water, in-vessel coils, manifolds, and diagnostics to the First Wall. The Test Blanket Modules have a more sophisticated structure and up to six different concepts that can be simultaneously tested in ITER [3]. The concept presented in Figure 3 was proposed by the European Union and identified as the Helium Cooled Pebble Bed Test Blanket System (HCPB TBS). It provides separated sections for Li_4SiO_4 or Li_2TiO_3 pebbles as tritium breeder and for beryllium pebbles as neutron multiplier (which will allow one to additionally transform the kinetic energy of the neutrons into thermal one, thus increasing the overall useful energy production). The module itself will be made of reduced activation ferritic/martensitic (RAFM) steel Eurofer97 [4].

ITER will also employ and study the usage of divertor, a complex plasma-facing component. As the magnetic confinement is not perfect it will cause the plasma to occasionally interact with the surrounding vessel walls. It will lead to their erosion and consequent contamination of plasma with impurities. To prevent this, the magnetic lines of the tokamak will be creating an additional magnetic field curvature into a separate chamber which is the divertor. Impurities will follow these lines and become trapped in the divertor, eventually evacuating from the vessel with a pump system.

1.1.3 Consequences of irradiation

The quality data of materials chosen for the design of nuclear devices must also be ensured by studying their performance during constant exposure to harmful neutron irradiation. This is

even more important for structural materials, as they are supposed to establish the structural integrity and safe operating regime of a reactor during its lifetime.

During the irradiation, an emitted energetic particle (neutron, ion, proton, etc.) collides with a structural atom of a material. This collision initiates the interactive process by displacing a so-called primary knock-on atom (PKA). The PKA then collides with other atoms, creating a cascade of point defects in the matrix of the material. Such defects can be vacancies (replacement of an atom from its position, leaving an empty space), self-interstitials (the replaced atom takes an unstable position between other atoms), transmutations (an atom changes its nucleus composition by releasing neutron or proton), or Frenkel defects (a combination of vacancy and self-interstitial). The number of neutrons passing through the material with the given energy is characterized by their fluence Φ, which is equivalent to the number of neutrons dN penetrating the sphere with the cross-section da:

$$\Phi = \frac{dN}{da} \tag{1.4}$$

However, in mechanics and nuclear materials sciences the displacement per atom (dpa) [5] is commonly used, as it provides a better estimation of the irradiation effects. It is defined as the number of times that an atom is displaced during the irradiation period of a given fluence. The dpa measure does not depend on the energetic spectrum of neutrons [6] and is applicable to ion irradiation.

When any of the listed defects reach a large number in a limited volume they may collapse into higher-scale defects, which can be listed as following:

- Dislocation loops – a concentration of many point defects that collapse into a lower energy structure. It is similar to the edge dislocation defect because it is also an extra plane of atoms (or its absence). However, the dislocation line of the loop is closed on itself, thus giving it a circular shape. The formation of dislocation loops is schematically presented in Figure 4.

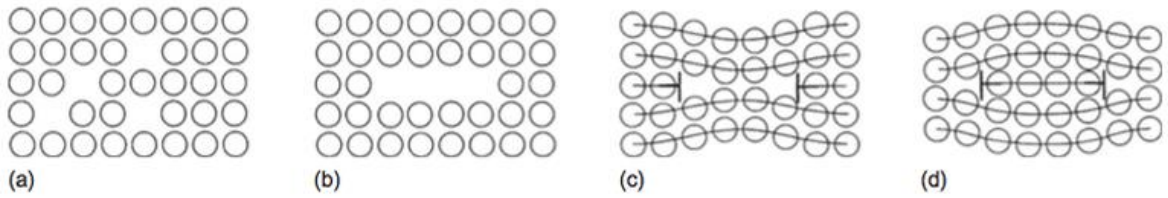

Figure 4. Formation of a prismatic dislocation loop. (a) Represents a crystal with a large nonequilibrium concentration of vacancies. In (b) the vacancies have been collected on a close-packed plane, and in (c) the disc has collapsed to form an edge dislocation loop. (d) Loop formed by a platelet of self-interstitial atoms; Reprinted from Introduction to Dislocations (Fifth Edition), Hull D., Bacon D.J., Chapter 3 – Movement of Dislocations, 43-62, Copyright (2011), with permission from Elsevier [7].

- Voids – a concentration of vacancies that can accumulate and form empty spaces in the material matrix.

- Precipitates and solute-rich clusters – a concentration of point defects can act as a sink for solute atoms of an alloy. The solutes then precipitate on the sink and may transform into new phases.

This list is usually assumed when referring to the term “radiation-induced defects”. All these defects lead to undesirable changes in the mechanical properties of the materials. These changes can be structured and described as well:

- Hardening and embrittlement: Hardening is the increase in resistance to the elastoplastic transition. This phenomenon is the main issue addressed in the presented work. Controlled hardening can be used for useful purposes, such as increasing the strength of the material to avoid plastic deformation, and it is commonly performed by the corresponding thermomechanical treatment (e.g. quenching). However, radiation-induced hardening is a constant accumulative process, and its excessive magnitudes can lead to the state when the theoretical onset of plastic deformation is higher than the onset of cracking. The material will eventually break through brittle fracturing, which is highly dangerous, as this will immediately destroy a component instead of having a safety margin provided by plasticity. A tightly associated embrittlement is the reduction of plastic capacity, which leads to the reduction of the amounts of plastic deformation that a material can withstand. Both phenomena are associated with the accumulation of previously discussed radiation-induced defects, which act as additional blocking mechanisms for dislocations, thus increasing the stress required for their movement.

- Irradiation creep: In addition to thermal creep, irradiation can cause additional losses in creep resistance. Creep is the plastic deformation of a material that can also occur below the stress values needed to initiate dislocation movement. Point defects created by irradiation are absorbed by dislocations, thus exhibiting dislocation climb and yielding a creep deformation.

- Void swelling: Coalescence of voids leads to their significant growth and consequent reduction of material density.

- Post-yield softening: Gliding dislocations locally annihilate radiation-induced defects, thus creating defect-free channels. These channels are more favorable for other dislocations to move, which leads to localized deformation zones.

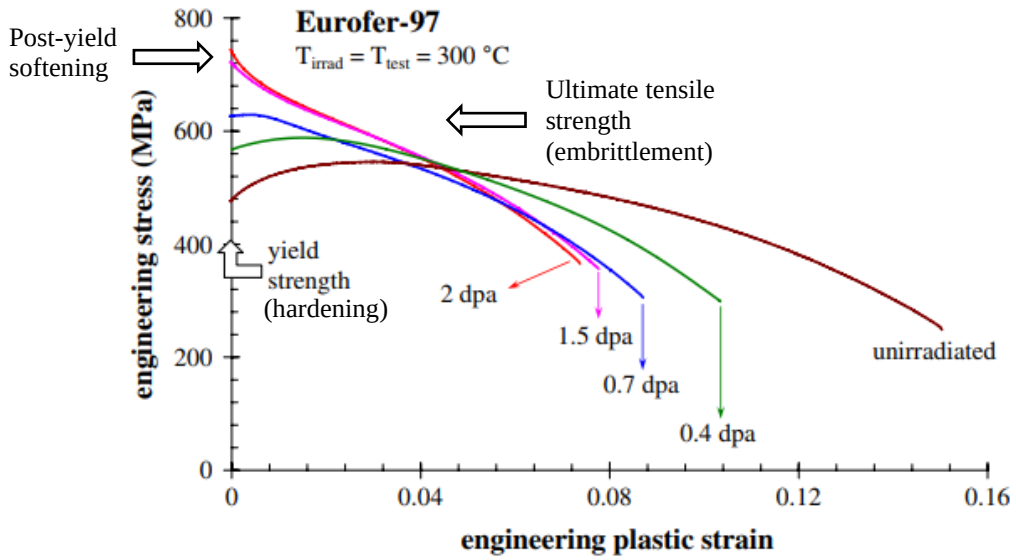

Figure 5. Tensile stress-strain curves of neutron-irradiated Eurofer97 affected by irradiation hardening, embrittlement, and post-yield softening; Reprinted from Journal of Nuclear Materials, 372, Chaouadi R., "Effect of irradiation-induced plastic flow localization on ductile crack resistance behavior of a 9%Cr tempered martensitic steel", 379-390, Copyright (2008), with permission from Elsevier [8] / Adapted from the original to indicate post-yield softening and embrittlement.

Figure 5 shows the experimental tensile tests data (plastic strain) for Eurofer97 steel irradiated with neutrons to different doses. One can see how yield stress gradually increases with the introduced dose, which is the phenomenon of irradiation hardening. Concurrently, the reduction of uniform elongation can be observed, which is the irradiation embrittlement. Once the dose reaches 1.5 dpa or more, the uniform elongation fades and the post-yield softening begins.

One can find a sufficient description of the radiation-induced changes in the microstructure and mechanical properties of the metallic materials in Refs. [9] [10] [11] [12] [13] [14] [15].
In conclusion, the ideal material for nuclear applications could be one that provides proven resistance to the listed effects during a significant and commercially justified lifetime of a reactor. However, the performance of the materials differs from one advantage to another. Nuclear engineers must perform a thorough selection of materials from the available databases to compromise dangerous effects where they are expected the most. Meanwhile, nuclear scientists must characterize materials in terms of their resistance to radiation-induced effects. For these purposes, the testing reactors are used.

1.1.3.1 Complexities of neutron irradiation for scientific purposes

Neutron irradiation as an experimental condition is a very limiting factor for the constant delivery of new research data. This comes from the high cost and time of an irradiation run, the limited amount of irradiation space for samples, and the very strict and complicated requirements for post-irradiation testing due to activation, which include specially trained personnel and constant use of bulky protective equipment. The partial solution to space and funds problems is achieved by the attractive miniaturization concept [16] [17] [18], an approach within the fields of nuclear materials science which lays in the reduction of the sample dimensions, thus allowing the irradiation of more samples in one irradiation run. However,

another problem is the magnitudes of the irradiation damage: their values of research interest and limited technically achievable possibilities.

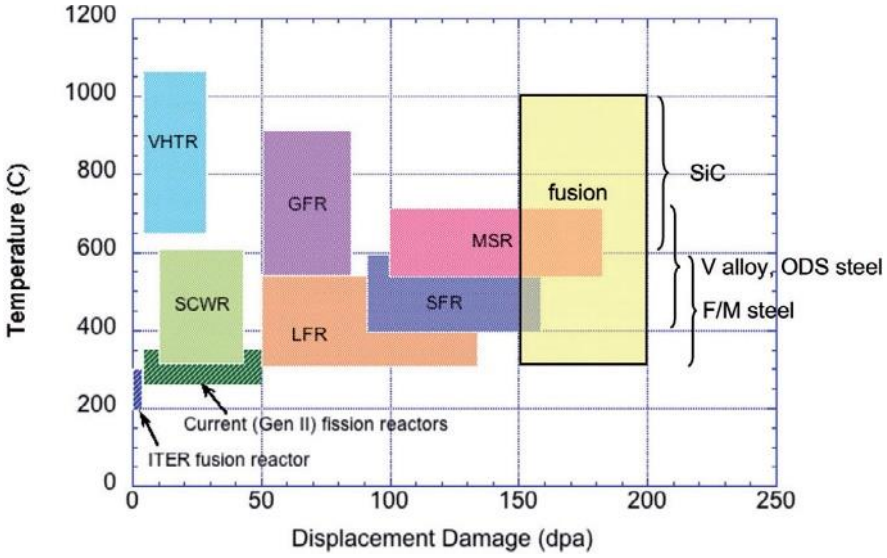

Figure 6. Expected doses in Gen IV and fusion reactors. Legend: VHTR – Very High Temperature Reactor; SCWR – Super Critical Water Reactor; LFR – Lead Fast Reactor; GFR – Gas Fast Reactor; SFR – Sodium Fast Reactor; MSR – Molten Salt Reactor; Reprinted from Materials Today, 12, Zinkle S.J., "Structural materials for fission & fusion energy", 12-19, Copyright (2009), with permission from Elsevier [19].

Figure 6 provides the operational temperatures and expected lifetime doses in terms of displacements per atom for a set of different types of reactors, including modern Gen II fission reactors, future Gen IV reactors, ITER, and a commercial fusion reactor, the follower of DEMO. DEMO itself would take an area on this chart at 50 – 80 dpa by the displacement damage *x* axis and 300 – 600°C by the temperature *y* axis [20]. The main idea this chart is used to reflect is that the magnitudes of damage doses are incredibly high for any modern testing reactor to be achieved in a reasonable time. Today, testing reactors are capable of providing 3-5 dpa/year, commercial fast-neutron reactors up to 20 dpa/year [21], however their use is even more limited for research purposes. Therefore, the nuclear materials scientific community is looking increasingly towards the attractive solution of ion irradiation.

1.1.3.2 Ion irradiation

Irradiation with ions is virtually unlimited in terms of damage scales, as the magnitudes can reach tens of dpa in hours. It is 100-1000 times cheaper than neutron irradiation [21], as it requires a particle accelerator instead of a complete nuclear fuel-powered fission reactor. The use of ions gives almost no residual activity, so the irradiated samples can be used for testing almost immediately after the irradiation run and without additional precautions. Although ion irradiation is safe, relatively cheap, and fast, it has its own limitations. The most substantial one is the penetration ability of the ions, as the charged particle is almost immediately stopped by the magnetic field of the material, thus distributing the damage on the sub-surface (<10 μm) of the irradiated spot non-uniformly. It results in the variation of post-irradiation properties with respect to the depth into sample volume, and the appearance of an important characteristic such as the damage-depth profile. Calculation of such profile is usually performed using Stopping

Range of Ions in Matter (SRIM) [22] binary collision code, which on top of the dpa damage profile also provides the fraction of interstitial atoms injected, as shown in Figure 7.

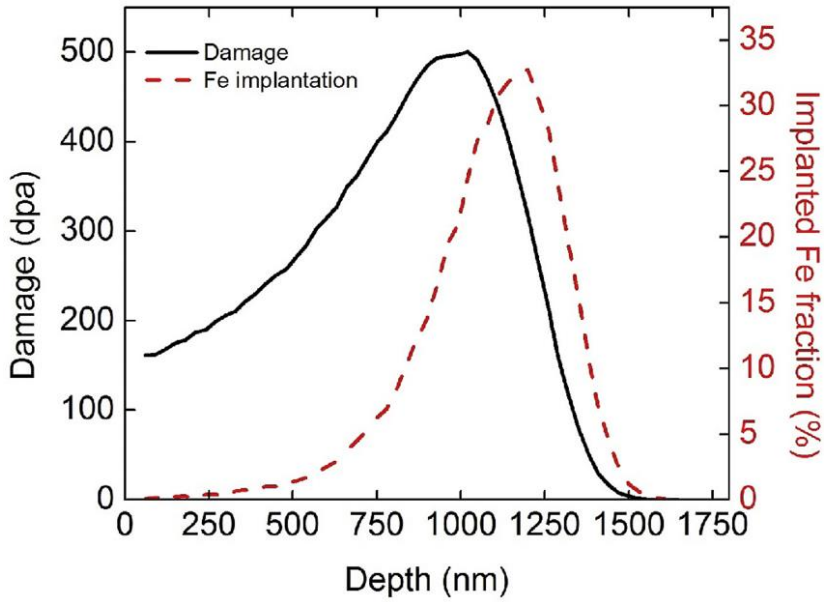

Figure 7. An example of SRIM-calculated depth profiles of irradiation damage and implanted atoms in pure iron irradiated with 3.5 MeV Fe^{2+} ions to 500 peak dpa; Reprinted from Acta Materialia, 134, Aydogan, E., Maloy, S.A., Anderoglu, O., Sun, C., Gigax, J., Shao, L., Garner, F.A., Anderson, I., Lewandowski, J.J., "Effect of tube processing methods on microstructure, mechanical properties and irradiation response of 14YWT nanostructured ferritic alloys", 116-127, Copyright (2017), with permission from Elsevier [23].

Therefore, to qualitatively estimate the impact of ion damage, one has to use a good characterization experimental tool applicable on the nanoscale or microscale and capable of providing standardized mechanical properties, such as nanoindentation (NI) tests.

1.1.4 Structural steels for nuclear applications & Eurofer97

High chromium ferritic/martensitic steels are a hot topic in nuclear materials sciences, as they provide vital advantages compared to austenitic steels commonly employed in early fission reactors. Now, they are considered as structural materials for key nuclear components in both future fusion and Gen IV reactors. They do not experience high neutron-induced swelling, have significantly higher thermal conductivity, and lower thermal expansion [24] [25]. Moreover, the concept of reduced activation ferritic/martensitic steels which presumes substitution of high activation alloying elements (Mo, Nb, Ni, and Co) with equivalent low activation elements (Ta, W, and V) allows the eventual activity of the material to be reduced after being imposed to irradiation. Many studies are oriented towards the development of new combinations of chemical compositions and subsequent thermomechanical treatments to discover new materials with better properties, however, still based on the reference examples (Eurofer97, T91, F82H, etc.) [26] [27] [28] [29].

Eurofer97 is a 9% chromium reduced activation ferritic/martensitic steel based on the Japanese variant F82H. Its development was driven by the need of the European Union to obtain its own low activation structural material for testing fusion concepts. It was developed in 1997 as a systematic optimization of 9%CrWTa alloys [30] and since then it has been widely studied and characterized by different means of thermomechanical tests and computational analyses,

including under post-neutron irradiation conditions. The experimental studies done on Eurofer97 have been collected and summarized in a single database [31].

Generally, the chemical composition of Eurofer97 steel must comply with the requirements provided in Table 1.

	C	S	P	Si	Mn	Ni	Cr	Mo	W	As+Sn+ Sb+Zr %
Min.	0.09	-	-	-	0.2	-	8.5	-	1.0	-
Max.	0.12	0.005	0.005	0.05	0.6	0.01	9.5	0.005	1.2	0.05
	Ta	**V**	**Nb**	**Cu**	**B**	**Al**	**Co**	**N_2**	**Ti**	**Fe**
Min.	0.1	0.15	-	-	-	-	-	0.015	-	Balance
Max.	0.14	0.25	0.005	0.01	0.002	0.01	0.01	0.045	0.02	Balance

Table 1. Required chemical composition of Eurofer97 in wt. %.

The standard industrial procedure for Eurofer97 production consists of hot rolling and subsequent heat treatments: austenitization at 980°C for 30 min, air cooling and tempering at 760°C for 90 min.

Eurofer97 is considered as the primary structural material for Test Blanket Modules in ITER [3], and for breeding blankets together with divertor cassette in DEMO [32] [33]. This material plays a crucial role in the structural integrity assessments of the in-vessel components. Therefore, there must be sufficient quality data to allow component design. However, the operational design window for DEMO in-vessel components goes far beyond those of ITER Test Blanket Modules [3]. There are significant data gaps on the material performance of Eurofer97 to cover DEMO requirements. Some of the failure mechanisms for the in-vessel components are expected after irradiation aging, and there are insufficient data on the effects of neutron irradiation on Eurofer97, especially at higher doses, with correct fluence or under the fusion neutron spectrum [34].

In addition to the direct planned application of Eurofer97 in ITER and other fusion devices, it is a good reference material for the development of new approaches for faster, safer and cheaper characterization of materials for nuclear applications.

1.1.5 Overview of nanoindentation for testing of ion-irradiated materials

The use of nanoindentation in nuclear materials science is rapidly emerging nowadays, as it is able to characterize the properties of the material using the minimum testing volume, which fits well into the mentioned miniaturization concept. Furthermore, the characteristic depth lies within the range of hundreds of nanometers to tens micrometers, which makes nanoindentation a perfect tool to study the impact of ion irradiation and its potential linkage with neutron irradiation. Moreover, some nanoindentation testing setups can provide the continuous stiffness measurement (CSM) technique, which allows measuring hardness with respect to depth (hardness-depth profile) and precisely analyzing the irradiation hardening at each nanometer of depth. The most common properties that can be obtained with this technique are hardness and Young's modulus; however, it can also be applied to analyze creep properties, or with additional tools, even fracture toughness. In order to study ion irradiation damage, testing parameters have to be carefully selected, as during the indentation a plastically deformed hemisphere is created and moving in front of the indenter tip. Its radius is usually longer than the indentation depth by the factor 5-10 for metals [35] [36], so the ion damage-depth profile must be considered. The mentioned factors are presented schematically in Figure 8.

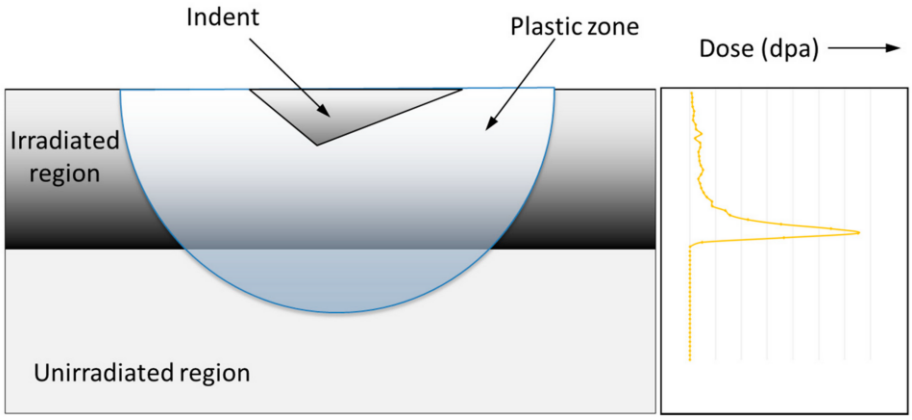

Figure 8. Schematic view of the nanoindentation process and damage distribution according to the damage-depth profile; Reprinted from Metals, 8(9) (2018), Saleh M., Zaidi Z., Hurt C., Ionescu M., Munroe P., Bhattacharyya D., "Comparative Study of Two Nanoindentation Approaches for Assessing Mechanical Properties of Ion-Irradiated Stainless Steel 316", licensed under CC BY 4.0 [37].

Nanoindentation testing itself can be used to estimate the irradiation hardening, but once it is used with complementary techniques, it becomes even more informative. Thereby, focused ion milling (FIB) in combination with transmission and scanning electron microscopies (TEM/SEM) can be used to study microstructural features of the subsurface associated with the ion damage or indentation process. Moreover, in combination with computational analysis using molecular dynamics (MD) or finite element method (FEM) calculations, one can additionally expand the understanding of the underlying processes occurring during the deformation and their differences between the reference and irradiated states of the material.

Some literature examples of nanoindentation simulations of ion-irradiated metals applied to recover their tensile behavior after neutron irradiation are discussed. In [38] P. Lin et al. study the impact of ion damage on the stress-strain response of A508-3 reactor pressure vessel (RPV) steel with body-centered cubic (BCC) structure by means of crystal plasticity FEM and nanoindentation. They introduce the hardening effect into the plasticity mechanism based on the empirical relation of the evolution of dislocation loops due to the magnitude of the irradiation damage [39], and simulate the nanoindentation process with different attack angles of the indenter tip. Upon confirmation of the validity with the experimental data for only one tip angle, the rest of the simulation results are considered correct, and the ratio of hardness to yield stress for each tip angle is established, according to the contact mechanics of self-similar indenters. The same contact mechanics are used to calculate the indentation strain for each tip angle. Eventually, the variety of yield stresses – indentation strains is obtained, and once interpolated or polynomially fitted, it matches very well with the corresponding tensile tests, but done on neutron-irradiated samples. Other examples are the works of X. Xiao et al. where the face-centered cubic (FCC) and BCC metals are frequently studied by means of complementary crystal plasticity FEM. In [40] the nanoindentation of ion-irradiated FCC Cu single crystals is simulated involving strain gradient theory, which allows one to correctly calibrate and separate the indentation size effect (ISE) typical for nanoindentation scales from the radiation-induced hardening. The hardening matrix is introduced as a complex term, which consists of the irradiation defect density, geometrically necessary, and statistically stored dislocations. Tensile test simulations are performed to calibrate the set of parameters responsible for the complex function of the hardening matrix and, once obtained, are transferred into nanoindentation simulations of the material to precisely recover and study the deformation

process. It must be added that in addition to the recovery of the mechanical properties, such approaches provide a complete picture of the ion-irradiated crystal behavior under the microcompressive deformation, and eventually allow reproduction and analysis of the microstructure evolution mechanisms in detail.

More general examples of the applications of microscopy or modeling techniques to support nanoindentation testing for nuclear materials, including ion-irradiated, are provided in Refs. [37] [41] [42] [43] [44] [45] [46]. Briefly, the mentioned works were aimed at prediction of the plastic properties from tests done below the ductile-to-brittle transition temperature, irradiation hardening, grain boundary effects, etc. Accordingly, FEM modeling is widely used for nanoindentation simulations. With a correct experimental validation, it can provide an underlying knowledge about the distribution and behavior of fundamental quantities associated with the deformation process (stress, strain, dislocation density, etc.). Furthermore, microscopy techniques such as S/TEM or atomic force microscopy (AFM) are generally applied to support the experimental process and reconfirm the measured data. For example, in [44] TEM was used to analyze the evolution of the subsurface microstructure due to irradiation, where the depth of the hardening peaks was found to be in good correlation with the highest concentration of irradiation defects. In [45] a systematic study of the indentation pile-ups heights is performed using AFM, providing their dependence on the microstructural state of the indented specimen.

1.2 Contributions of the thesis

In this thesis manuscript, the problem of evaluation of radiation-induced damage on plasticity of metals and metallic alloys for nuclear applications is addressed. The challenge is to find time- and cost-efficient techniques capable of predicting the effect of neutron irradiation, which normally requires lengthy and expensive experiments. It is proposed to combine a set of experimental and computational tools oriented towards the simplification of the materials characterization process, and validate the obtained approach using a reference, well-studied material Eurofer97 steel.

1.2.1 General objective of the thesis

The proposed research aims to develop a methodology that allows one to evaluate the properties of neutron-irradiated material using nanoindentation tests applied to an ion-irradiated material. These properties are assumed to be representative for materials exposed to neutron irradiation at the same dose and irradiation temperature. The correctly obtained (experimentally validated) hardening-dose function introduced to the subsurface layer of the nanoindentation model may be used as a modification law for the material laws of the unirradiated material. Thus, a predictive tool is established, allowing one to experimentally characterize the irradiated material in a financially efficient and safe (i.e. no radiation-induced activation) way in order to use these data to computationally model its macroscale behavior under operational conditions and desired geometry.

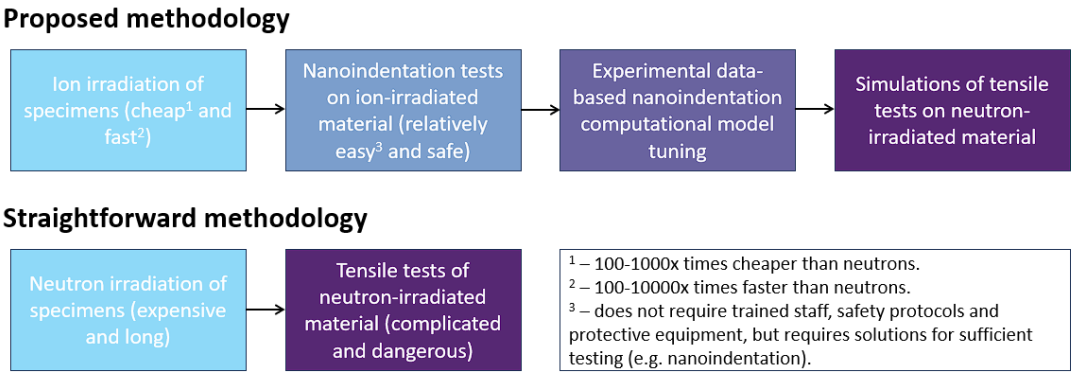

Figure 9. Schematic comparison of the methodologies for testing irradiated materials.

Figure 9 gives a comparison of the methodology developed in this study and the straightforward testing of irradiated materials. Although the usage of ion irradiation adds extra steps, their implementation tremendously saves time, costs, and human resources. Therefore, such approaches are of great interest to the nuclear materials community.

Presumably, the development of similar methods is not commonly achieved because of the focus on more fundamental comparison of the ion and neutron impacts. While delivering similar magnitudes of dpa damage, the effects of these particles have differences from each other. First of all, it comes from the clear difference in the PKA energy spectrum between ion and neutron irradiation, which affects the formation of high-order defects (e.g. dislocation loops). Second, ion irradiation does not produce transmutation reactions in a material, thus neglecting their contribution to the evolution of the material microstructure. Moreover, self-ions also produce additional interstitials in the material matrix, which makes the eventual microstructure even more different from the case of neutron irradiation. It is completely meaningful to study the physics of the mentioned processes; however, the high complexity of the models and the deep fundamental incomparability of both irradiations make them challenging to interconnect. The presented work takes the risk of finding a balance between the fundamental aspects required for the implementation of the method and the empirical simplicity of the input and output data. Therefore, this method is proposed to be called “semi-empirical” due to its basing on accurate analytical equations of dislocation dynamics, while its purpose is to predict one experimental response from another.

Another reason could be that the development of similar methods does not aim to build a self-sufficient multidisciplinary approach. Commonly, the works available in literature are limited by covering just one aspect (i.e. experiments or simulations) per research team, thus superficially accessing important data (e.g. validation tests from another research group). On the other hand, the works which are fully performed under the total control of a research team are usually satisfied with tuning their models to correctly reproduce nanoindentation experiments on ion-irradiated materials, rarely giving suggestions on how to use this data to predict neutron-affected mechanical properties. The philosophy of this work considers comprehensive access to research data as of high importance, thus reducing the possible issues that arise from misinterpretations of other works. At the same time, the validated nanoindentation simulations are intermediate data on the way to the simulations of the more important conventional tests of neutron-irradiated material. Therefore, the emerging method is eventually seen as a research tool to be applied, rather than a single investigation.

The global objective, eventually, can be stated as: establishment and experimental validation of the nanoindentation CPFEM model for characterization of irradiation damage in ion-irradiated structural steel at elevated temperatures for the prediction of neutron-induced irradiation hardening through simulations of tensile tests.

1.2.2 Methodology

Mechanical testing built around nanoindentation experiments will be simulated with crystal plasticity finite element method (CPFEM) modeling and supported by different types of electron microscopy to comprehensively study the nano/microscale performance of the material before and after irradiation. The constitutive parameters responsible for the irradiation effects in the experimentally validated nanoindentation CPFEM model can then be transferred to simulations of conventional tests (tensile tests in the presented case) to derive the macroscale behavior of the irradiated material. This is driven by the fact that the usage of crystal plasticity (CP) provides a good connectivity between deformation mechanisms on mesoscopic and macroscopic scales [47] [48] [49].

However, the presented research has been done in an inverse way (Figure 10). The known magnitudes of irradiation hardening from the experiments performed on neutron-irradiated material are used as input for the CPFEM nanoindentation models to simulate the experimental nanoindentation data performed on ion-irradiated material. In other words, the known valuable engineering data of interest is used to recover the intermediate parameters important for deducing those data. This has been done to confirm the validity of the approach while avoiding a time-consuming fitting procedure as well as establishment of this procedure. It is meaningful considering limited time ranges allocated for the research and CPU power of the used computational setup. Nevertheless, an attempt to establish a "correct" algorithm will be presented in the thesis, as well as suggestions for its improvements in the future.

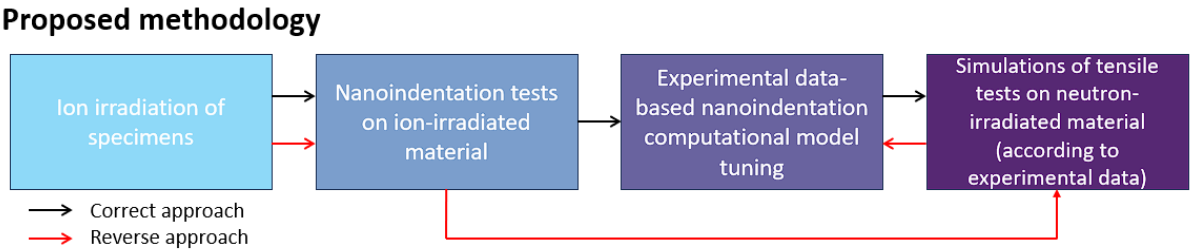

Figure 10. Schematic comparison of the proposed methodology done in the correct and reversed way.

In the ideal case, virtually safe ion irradiation must be used to imitate the effects of neutron damage and consequently deduce the mechanical properties of neutron-irradiated material, as shown in Figure 10 as the correct approach. Such an approach would allow a user to estimate the irradiation hardening in a structural steel (or other metallic material once the efficiency of the method is demonstrated) while **avoiding neutron irradiation**. Each similar methodology is a success for nuclear materials sciences, as they can accelerate the research pace by neglecting the negative sides of the neutron irradiation process described in §1.1.3.1.

Given the complicated microstructure of Eurofer97 steel, the CPFEM model of the nanoindentation process will first be established and validated on a "simpler" material, which is pure α-iron. The approach of using α-iron as a surrogate for materials with a more complicated microstructure is widely applied for multiscale modeling and related experimental campaigns within European projects (e.g. PERFECT [50], GETMAT [51], M4F [52]). Within the performed study, pure iron is used to establish the model only in the non-irradiated state, in order to familiarize with the incoming complexities and overall efficiency of the proposed methodology. Once it is achieved and demonstrated, the performed steps are applied to computationally reproduce the mechanical response to the nanoindentation process of non-unirradiated Eurofer97. As the last general step, the ion-irradiated substrate is geometrically

represented as a domain with variational, depth-dependent subsurface properties, typical for ion-irradiated specimens in reality. The subsurface properties are assigned as the function of the irradiation damage dose expressed in dpa. Apparently, they are supposed to be transferred to simulations of macro-tensile tests to predict the irradiation hardening in the neutron-irradiated material, i.e. the increase of yield stress. However, as stated before, the problem in this research is solved inversely, so the tensile tests from the literature are used to establish and validate the intermediate procedure steps based on the simulations of the nanoindentation process in ion-irradiated Eurofer97.

1.2.2.1 Experimental part

The experimental side of the proposed protocol to characterize any ion-irradiated material is as follows. Tensile testing in a range of temperatures is used to obtain the constitutive laws of the non-irradiated material and its temperature-dependent behavior. Nanoindentation experiments on the non-irradiated material are performed in the same temperature range to associate the nano/microscale compressive deformation process with the macroscale tension. Nanoindentation of the ion-irradiated material in the temperature range is performed to distinguish the difference caused by the irradiated damage. Both sets of the experimental data obtained are also used as the validation unit for further CPFEM calculations. Microstructural investigations are performed using SEM to analyze the topologies of indentation imprints and pile-ups; electron backscatter diffraction (EBSD) to obtain an idea of the grain size of the material (to account for the Hall-Petch effects further) and the positions of the imprints with respect to the surface orientation (for more accurate study of the pile-up behavior and to predict the possible issues associated with the crystal anisotropy); TEM to estimate the dislocation density of the material in reference and preferably in the deformed state (essential for dislocation density-based plasticity models). Additionally, FIB can be used to cut and study subsurface regions beneath the indented area for complementary analysis of the deformation processes during the indentation, thus providing a better quality of the deduced constitutive parameters. Moreover, as can be concluded from the presented work, in order to utilize the predictivity of the method, the SEM and EBSD characterizations can be avoided, thus providing additional simplicity. This is because the former is used to justify possible measurements corrections; whereas the latter is mainly applied to study the anisotropy effects and to account for quantities which can be a subject of an ordinary fitting. Therefore, in the case of a smooth experiment which gives no doubts about its correctness, these techniques can be avoided.

1.2.2.2 Computational part

The computational part consists of finite element analysis based on crystal plasticity theory. CPFEM is an essential approach to simulate the nanoindentation process in irradiated materials. First of all, it allows to correctly capture the effects of anisotropy appropriate for the nanoindentation testing scales, as even the finest microstructure of a material will be still comparable to the nanoindentation deformation levels. Second, the interactions between dislocations and irradiation defects can be deeply studied using other techniques, such as MD simulations, to obtain an insight into the energy potentials of these interactions [53] [54], and consequently transfer them to CPFEM models to correctly reproduce the behavior of the defects with respect to their orientations. Such interconnection of techniques contributes to the important approach of multiscale modeling, allowing to simultaneously study irradiation defects at different scales [52] [55]. Third, the surface topology under constant nanoindentation parameters varies with the surface orientation [56], which can be crucial in the determination of hardness [57].

The constitutive model implementing the condition for plastic slip in a material is parametrized with respect to the previously performed microstructural investigations (dislocation density, Hall-Petch effect), literature insights (kink-formation enthalpy, elastic coefficients, etc.) and fitting. The validation is performed by simulating the uniaxial tension of a virtual polycrystal and comparison of the outcoming true stress-strain curve with the previously obtained tensile experimental data until a good fit is obtained. Once validated, the constitutive parameters are transferred into the CPFEM simulations of the nanoindentation process. It is assumed that the screw dislocation slip dynamics is enough to represent and interlink the macro-tensile and nano-/micro-compressive deformations, as it is the main carrier of plasticity in the BCC metals. Force-displacement curves obtained by means of nanoindentation CPFEM simulations are compared with their experimental alternatives to confirm the reproducibility.

1.2.2.3 Combined experimentally numerical approach to estimate radiation-induced hardening

Simulations of the ion-irradiated material are based on the division of the ion-irradiated subsurface into differentiated layers, where each layer is assigned with a modified constitutive law of non-irradiated material. These modifications will be made in correspondence with the magnitude of radiation-induced hardening typical for an average damage dose in dpa in that region (i.e. layer) according to the tensile tests data on neutron-irradiated material from the literature (reversed approach); see Figure 11. Eventually, if the nanoindentation simulations recover their experimental analogue, a proof-of-concept will be obtained, allowing one to use macroscale tensile data with neutron damage to simulate nanoindentation with ion damage, and vice versa. Consequently, a single ion-irradiated specimen can be potentially used for the characterization of radiation-induced hardening in a material in the range of doses, the selection of which is only dependent on the ion irradiation parameters. Overall, nanoindentation crystal plasticity simulations based on the tensile tests are not common findings in the literature, especially for irradiated materials with complex microstructure and elevated temperatures.

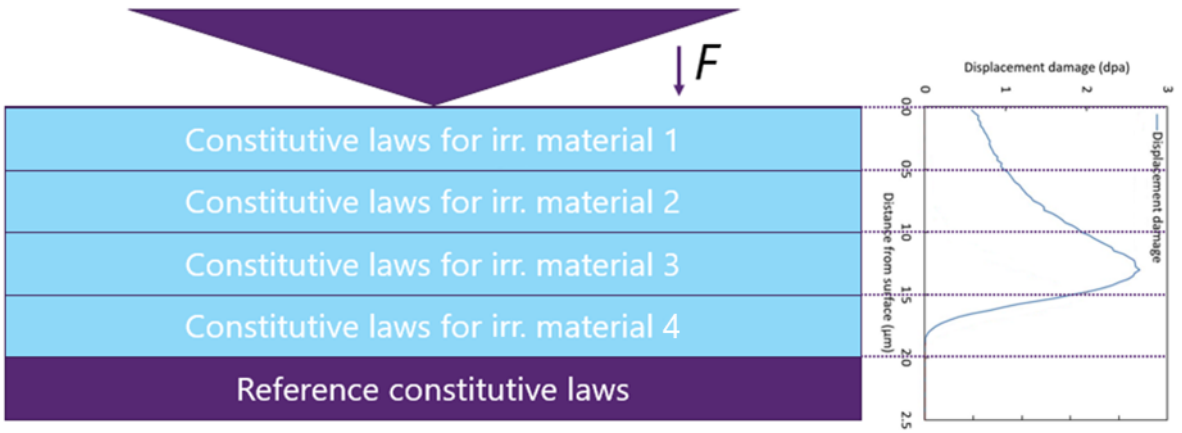

Figure 11. Schematic representation of the layered geometry.

Eventually, the development of a computational algorithm assigned for fitting the hardening-depth-dose complex function is proposed. It is based on the nanoindentation simulations in ion-irradiated material, which are crucial for the evaluation of the constitutive parameters responsible for the irradiation hardening. In this thesis, only results obtained by

manual fitting will be presented, although providing decent accuracy. The algorithm that combines all aspects of the proposed approach is illustrated in Figure 12.

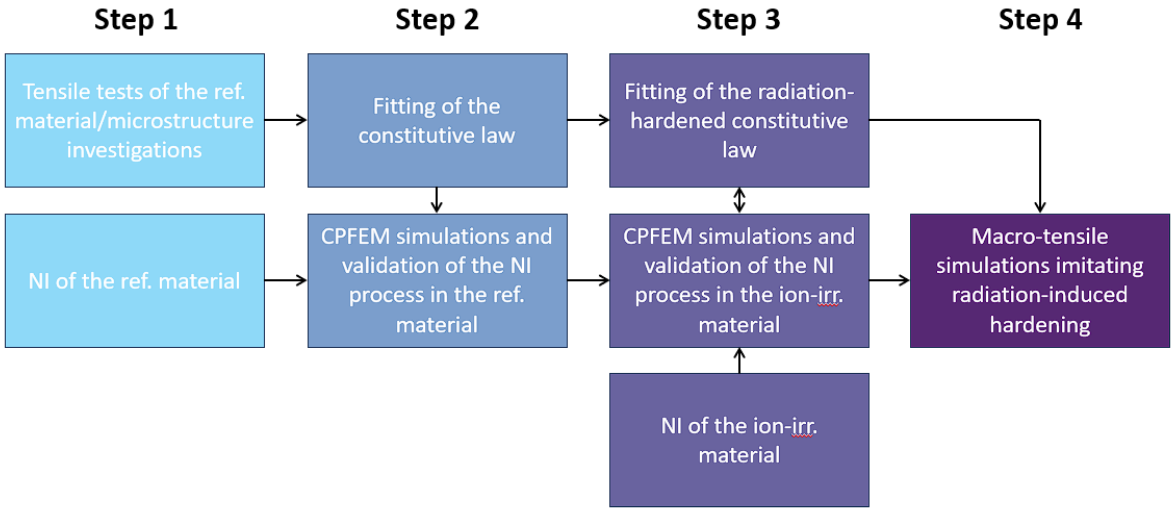

Figure 12. The algorithm to evaluate the neutron-induced irradiation hardening.

1.3 Scientific innovations

The presented approach extends the list of methods proposed in the past. While based on many common elements typical for computationally experimental analysis of the ion-irradiated materials built around nanoindentation, it has features that are not yet reported.

- Actually, the approach to simulate the material substrate in layers as a nanoindentation study is not completely novel. For example, in [58] the substrate is presented as a hemisphere divided into layers, where each layer is associated with a certain magnitude of irradiation hardening plus a contribution from the indentation size effect. This allows reproducing the experimental ion-irradiated hardness with good accuracy, where each hardness contribution is separated from each other. However, in the case of the presented study, layering is introduced as a geometrical feature within an FEM, which is more complex on one hand and more informative and representative on another, as it allows investigation of the integral response of the material.

- The simplicity and transferability of the constitutive model must be admitted. Further, it will be seen that the dislocation slip formulation used as the plasticity law is versatile enough to represent both the pure iron and Eurofer97 steel in reference and irradiated states, undergoing uniaxial tension or nanoindentation. This allows minimizing the set of theories and their parameters used to describe a material behavior as well as the complementary characterization techniques used for their determination. One can easily switch between materials or their conditions using the same model (by adapting the values of the constitutive parameters) and try simulating other types of non-fracturing loading modes (such as 3-point bending tests) to extend the predictivity of the approach beyond the tensile testing. Moreover, if a deeper study of physical phenomena is required, the set of tools is flexible enough without compromising its efficiency under the most basic usage.

- Additionally, the philosophy of this work is to establish a self-sufficient multidisciplinary characterization protocol, where all steps are performed under the control of a research team. It is typical for many studies found in literature to operate with only one side of the procedure, either performing experimental characterization of the irradiation hardening or making simulations based on the experimental data obtained elsewhere. Here, comprehensive access to the research data and its understanding is considered of high importance, thus reducing the possible issues outcoming from misinterpretations of other works. Therefore, the emerging method is eventually seen as a research tool to be applied, rather than a sole investigation.

Some technical novelties have taken place as well:

- An improbable performance of application of the 20 nm SiO_2 layer to protect iron samples from oxidation at high temperature testing has been shown (§3.2.2).

- A superimposing of the indented area extracted using FIB and inspected by SEM with its FEM analog to precisely study the degrees of deformation occurring under the indenter (§3.4.3, Figure 46).

1.4 The structure of the thesis

The thesis manuscript is structured as follows. The reader should have already been familiarized with the introduction Chapter 1, where the global context of the reasons driving this research has been presented. The second section of the introduction gives an overview of everything related to the presented research process, such as preset goals, used methodology, and the introduced novelty.

Chapter 2 provides more comprehensive information about the experimental and computational techniques used in this work. The following two chapters will familiarize the reader with the main research body, where the experimental characterization as well as computational work and microstructure investigations will be performed on two materials of the study: Chapter 3 will establish the procedure on the unirradiated pure iron material as a probatory process, whereas in Chapter 4 the knowledge obtained will be used to investigate a more complex Eurofer97 RAFM steel, introducing the irradiation effect. In Chapter 5 the main conclusions will be discussed first, then the outlook for future studies and the applicability of the presented method will be proposed. Chapter 5 will also cover the lessons learned during the investigation, which have not been included in the main part for different reasons.

1.5 List of publications

1.5.1 Topic-related publications

During the research, four topic-related publications have been published. Their metadata and an overview of each publication will be given.

1. **T. Khvan**, L. Noels, D. Terentyev, F. Dencker, D.D. Stauffer, U.D. Hangen, W. Van Renterghem, C. Cheng, A. Zinovev, “High temperature nanoindentation of iron: Experimental and computational study”, *Journal of Nuclear Materials* 567(11):153815, May 2022 [59] – is a paper published on the full basis of Chapter 3 of the presented manuscript, where the experimentally computational characterization is performed and the CPFEM nanoindentation model is developed for the pure iron product. The

publication also includes the microstructure investigations performed by means of SEM, EBSD, and TEM-FIB.

2. L. Malerba et al., **T. Khvan**, "Multiscale modelling for fusion and fission materials: The M4F project", *Nuclear Materials and Energy*, 29:101051, Aug 2021 [52] – gives a complete overview of the Multiscale Modeling for Fusion and Fission Materials (M4F) project, where the comprehensive experimental and multiscale computational characterization of materials aimed for application in both fusion and fission reactors has been performed within many research institutions across the EU. The main materials of this study represented the increasing microstructural complexity step by step from iron to Eurofer97 steel: pure α-iron (studied in this work), Fe9Cr, Fe9Cr-NiSiP, Eurofer97 (studied in this work) in as-received, deformed, ion and neutron-irradiated states. The experimental, microscopy, and computational works performed around the nanoindentation testing from the presented manuscript have been used as a part of the M4F project.

3. L. Veleva, P. Hähner, A. Dubinko, **T. Khvan**, D. Terentyev, A. Ruiz-Moreno, "Depth-Sensing Hardness Measurements to Probe Hardening Behaviour and Dynamic Strain Aging Effects of Iron during Tensile Pre-Deformation", *Nanomaterials* 11(1):71, Dec 2020 [45] – provides an experimental study of the pure iron product from Chapter 3 by means of tensile tests, nanoindentation and atomic force microscope. The indentation pile-ups heights and their contribution to the measurement error are evaluated and the elastic modulus correction is applied to the measured hardness and the Young's modulus quantities. The significant dynamic strain aging (DSA) influencing material behavior is observed for the first time. A collaborative study within the M4F project.

4. A. Ruiz-Moreno et al., **T. Khvan**, "Round Robin into Best Practices for the Determination of Indentation Size Effects", *Nanomaterials* 10(1):130, Jan 2020 [60] – is a round robin work between seven nanoindentation laboratories-members of the M4F project to evaluate the indentation size effects in Eurofer97 steel. Different parameters and loading modes were applied to obtain statistical data for hardness and Young's modulus of this material.

At the time of writing this manuscript, a publication based on the data provided in Chapter 4 is being prepared for submission.

1.5.2 Publications on other topics

1. D. Terentyev, A. Zinovev, **T. Khvan**, J.H. You, N. Van Steenberge, E.E. Zhurkin, "Irradiation embrittlement in pure chromium and chromium-tungsten alloy in a view of their potential application for fusion plasma facing components", *Journal of Nuclear Materials* 554(3):153086, May 2021.

2. G. Bonny, **T. Khvan**, A. Bakaeva, C. Yin, A. Dubinko, C. Cabet, M. Loyer-Prost, N. Castin, A. Bakaev, D. Terentyev, "Effect of statistically stored dislocations in tungsten on the irradiation induced nano-hardening analyzed by different methods", *Journal of Nuclear Materials* 543:152543, Jan 2021.

3. G. Bonny et al., **T. Khvan**, "Trends in vacancy distribution and hardness of high temperature neutron irradiated single crystal tungsten", *Acta Materialia* 198(1-3), July 2020.

4. D. Terentyev, **T. Khvan**, J.H. You, N. Van Steenberge, "Development of chromium and chromium-tungsten alloy for the plasma facing components: Application of vacuum arc melting techniques", *Journal of Nuclear Materials* 536(3):152204, May 2020.

Chapter 2. Overview of the research techniques and methods

In this chapter a brief description of the experimental, computational and microscopy techniques used in the methodology will be presented.

2.1 Nanoindentation

Nanoindentation is the instrumented hardness test, which means that a highly solid material (usually diamond) formed in a special shape is firstly immersed into the surface of a tested specimen on a nano/micrometer scale and then extracted, whereas the applied force and penetration are recorded by the experimental setup. The output of such a test is a curve in force-displacement ($N-m$) cords, which can be analyzed in order to obtain the mechanical properties of the material. Essential parameters, a force-displacement curve, and their interconnection with the indentation process are presented in Figure 13.

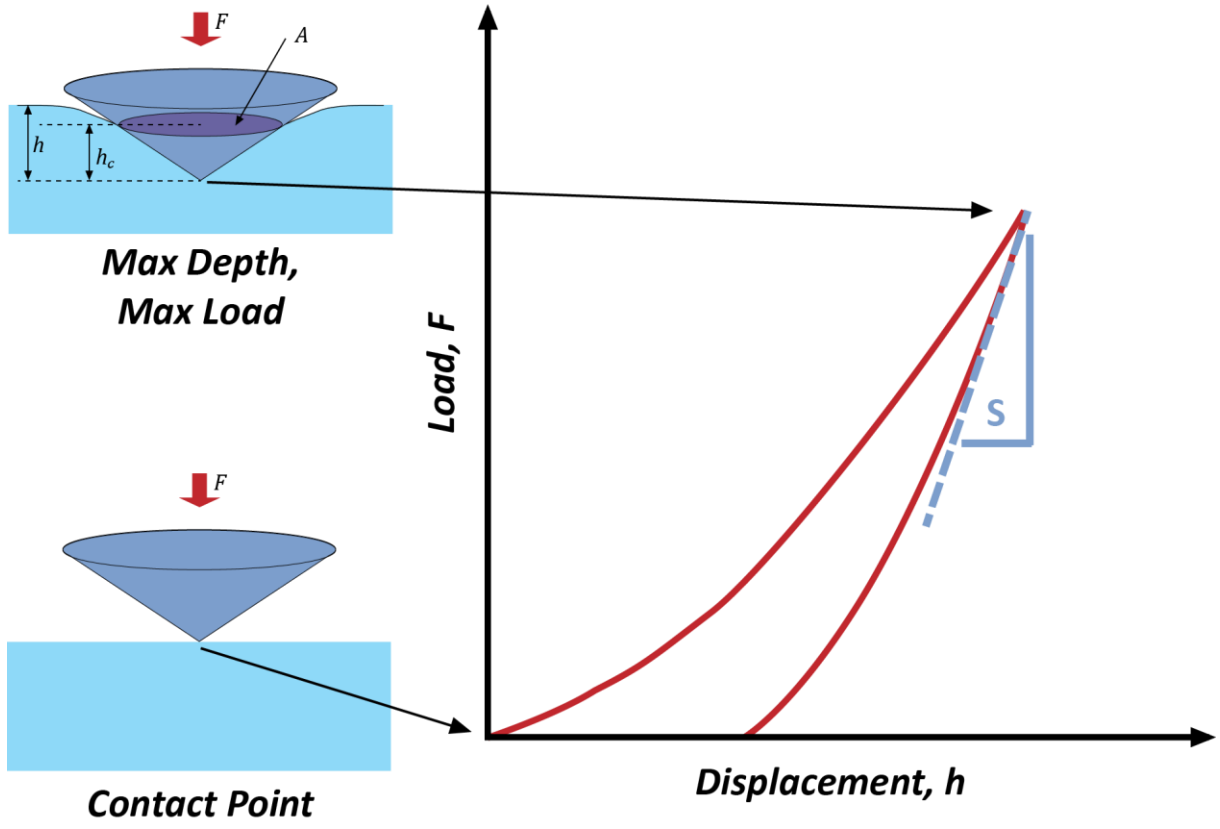

Figure 13. Schematic process of a nanoindentation test and a nanoindentation force-displacement curve.

Many different indenter tip shapes exist, which are applied depending on the required material response, i.e. characterization. The most widely used nanoindenter tips in metals testing are:

- Berkovich: three-sided geometrically self-similar pyramid with a total included angle of 142.3° and a half angle of 65.27°, measured from the axis to one of the pyramid flats.

- Spherical: a hemisphere. Being blunt, it does not penetrate the material surface immediately, making the elastoplastic transition visible for studying plastic properties of a material.

- Cube corner: three-sided pyramid with perpendicular faces. Generally used for fracturing nano-/micropillars created by focused ion milling for fracture toughness studies.

The presented work is based on modeling and testing with only a Berkovich indenter, shown in Figure 14. It is applied for determination of hardness and Young's modulus of a material, which possibly makes it the most widely used in nanoindentation testing.

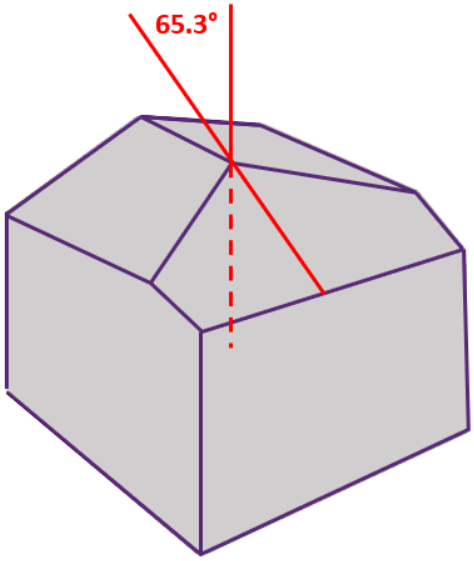

Figure 14. Berkovich indenter tip.

The Oliver-Pharr method [61] presented to the scientific community in the beginning of 1990s is a nanoindentation state of art, which established the process of the evaluation of these mechanical properties and brought nanoindentation testing to a new level. The application of the method is based on a power law fitting of the initial slope of the unloading part, thus obtaining an elastic property of a material called "unloading stiffness" S (see Figure 13).

$$F = B\left(h - h_f\right)^m \tag{2.1}$$

where B, h_f and m are arbitrary fitting parameters. The stiffness at the peak of the unloading curve represents the elastic response of the material at the initial point of unloading, which can be calculated from the derivative of Eq. (2.1).

$$S = \left(\frac{dF}{dh}\right)_{h=h_{max}} = mB(h_{max} - h_f)^{m-1} \tag{2.2}$$

The stiffness is then used to calculate the contact depth h_c and the contact area $A(h_c)$ as the function of the contact depth.

$$h_c = h_{max} - \epsilon \frac{F_{max}}{S} \quad (2.3)$$

$$A = 24.56 \cdot h_c^2 + \sum_{i=1}^{8} C_i h_c^{1/2^{i-1}} \quad (2.4)$$

where h_{max} is the maximal indentation depth, F_{max} is the maximal indentation force, and ϵ is the geometrical factor of the indenter, which is equal to 0.75 for Berkovich indenter. C_i are fitting constants.

The contact depth is the vertical distance along which the contact is made. It is not equal to the measured depth because some volume of a material may "sink" around the indented place. This sink phenomenon is called an "indentation sink-in", and the opposite occasion, when a material comes out of an indentation imprint is called an "indentation pile-up" (not to be confused with the dislocation pile-up). The contact area is the projected area of the area of contact. The term $24.56 \cdot h_c^2$ of the formulation (2.4) calculates the contact area of the perfectly sharp Berkovich indenter. As in reality the perfect sharpness is unachievable, the second polynomial term is used to fit the contact area to a value measured on a material with the known properties.

The unloading stiffness and the contact area are used to determine the reduced modulus E_r – Young's modulus of a material affected by the elasticity of an indenter. This impact can be subtracted to obtain a proper Young's modulus of a material:

$$E_r = \frac{\sqrt{\pi}}{2} \frac{S}{\sqrt{A}} \quad (2.5)$$

$$\frac{1}{E_r} = \frac{(1-\nu^2)}{E} + \frac{(1-\nu_i^2)}{E_i} \quad (2.6)$$

where ν – is Poisson's ratio of the inspected material, E – Young's modulus of the inspected material, ν_i – Poisson's ratio of an indenter, and E_i – is Young's modulus of an indenter (ν_i = 0.07 and E_i = 1140 GPa for diamond).

Another important property that can be obtained from the nanoindentation is hardness:

$$H = \frac{F}{A} \quad (2.7)$$

Hardness is the ability of a material to resist plastic deformation; therefore, it is tightly associated with elastoplastic transition (yield stress). The famous empirical Tabor's relationship [62] connects hardness and yield stress of a material such as:

$$H = \frac{C}{\sigma_y} \quad (2.8)$$

where C is Tabor parameter and σ_y is yield stress. C was calculated by Tabor to be in the range from 2.8 to 3.1 for structural metallic alloys. However, this is purely an empirical parameter which was originally introduced for spherical indentation. It strongly depends on the type of indentation testing, the shape of the indenter, the plastic properties of the material and other behavioral characteristics that may have an impact on the measurements, and does not necessarily lay within the range proposed by Tabor.

The formation of indentation pile-ups can result in an inadequate estimation of the contact area and a consequent wrong calculation of hardness and Young's modulus. To account for this, the elastic modulus correction (EMC) technique is applied. To perform the EMC, one needs to know the macroscopic elastic modulus of the tested material, which can be used to calculate the reference reduced modulus E_r^{ref} with Eq. (2.6). Then the squared ratio of the two moduli is used to calculate the new corrected hardness:

$$H_{corr} = \frac{H}{\left(\frac{E_r}{E_r^{ref}}\right)^2} \tag{2.9}$$

2.2 Tensile tests

Tensile testing is one of the most used conventional tests of materials, particularly metals. A tensile test is performed by applying uniaxial tension on a testing specimen with a special shape, which allows to effectively fix the specimen in clamps of a testing bench along two spatial directions and being freely deformed along the third one. In the case of testing metals, the most popular shapes of specimens are cylindrical and flat tensile, both can be seen in Figure 15(a). The latter is often called as "a dog-bone" (the shape reminds of a classical representation of a bone as a dog's treat):

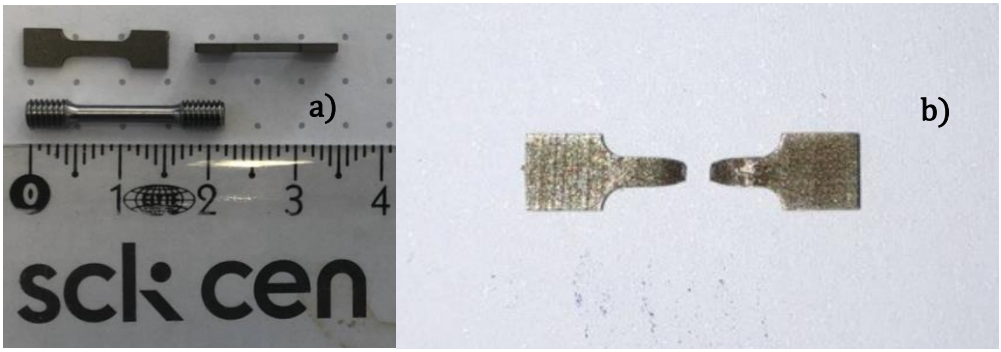

Figure 15. a) Flat tensile (upper) and cylindrical (lower) specimens; b) A fractured flat tensile specimen with the "neck".

The geometry of the specimen is designed in a way that concentrates most of the measured deformation in the thin middle part, which is called "a gauge", as the wide parts are used to clamp the specimen to a testing bench and are supposed to not be deformed. The gauge is deforming evenly (uniformly); however, after some amount of strain, the plastic deformation starts to localize somewhere on the gauge and form a "neck". The necking stage leads to a fracture and a specimen breaks apart. A metal sample passed through the necking stage and breaking is shown in Figure 15(b).

Tensile testing is a very informative technique, as it allows a lot of important mechanical properties of materials to be measured, and it can be applied with different loading types, magnitudes, and in a wide range of temperatures depending on the possibilities provided by a particular testing bench. For instance, a simple straining machine can easily afford a range of -196°C (liquid nitrogen as a coolant) up to 500-600°C, whereas the upper limit is only a matter of quality of a furnace and thermal insulation.

The list of mechanical properties can be obtained from a tensile test:

- Yield stress – a property which characterizes at what stress value the plastic deformation occurs.

- Ultimate tensile stress/uniform elongation – properties which characterize at what stress/strain values the plastic instability occurs (i.e. necking).

- Fracture stress/strain – properties which characterize what stress/elongation levels a material can sustain upon breaking apart.

- Reduction of area – plasticity property, which characterizes a level of cross-sectional thinning after a test.

During the test, the applied force is measured by a load cell, and the elongation is measured as a displacement of the machine pulling rod. The output is given in force-displacement (*N-m*) cords and can be recalculated in the stress and strain using the following formulas:

$$\sigma_{eng} = \frac{F}{A_0};\ \varepsilon_{eng} = \frac{L - L_0}{L_0} \tag{2.10}$$

where F – is the measured force, A_0 – is the initial cross-section of a specimen, L – is the measured displacement, and L_0 – is the initial length of the specimen. The calculated stress and strain are called "engineering" and provide the values with respect to the initial cross-section and length. However, this assumption is not completely true, as their dimensions change during the test. The stress and strain can be calculated with respect to these changes as:

$$\sigma_{true} = \sigma_{eng}(1 + \varepsilon_{eng});\ \varepsilon_{true} = ln(1 + \varepsilon_{eng}) \tag{2.11}$$

In this case, stress and strain will be called "true". The application of these formulations presumes several assumptions, such as 1) volume conservation of a sample during deformation; 2) the deformation is uniform. As the latter only occurs until the necking stage, the calculation of true stress after the ultimate tensile stress point (which is close to the onset of necking) is not straightforward. Therefore, it may require some advances in measurements of the actual specimen cross-section during the test or modeling of the neck formation/development process. However, in this work, these problems will not be addressed and investigations will be based on just the information obtainable with Eq. (2.11).

2.3 Electron microscopy techniques

2.3.1 Scanning electron microscopy

The scanning electron microscope is an advanced tool for observing surface phenomena of conductive materials with high magnification. The microscope can be used to analyze sample topography, morphology, composition, grain orientation, crystallographic information, etc. The principle in brief is based on an electron beam creating primary electrons that are aimed at a sample and interact with its surface. When the electrons are interacted, they provide energy to the atomic electrons of an inspected material, and they are released as secondary electrons (SE), so the image can be formed by collecting them from each point of the specimen. Actually, not only secondary electrons are released during interaction, but also X-rays and backscattered electrons (BSE). All of them are being collected by detectors and then analyzed to provide

imaging or other types of information. Within the presented work, SEM is used to investigate indentation pile-ups and features of the deformed material.

2.3.2 Electron backscatter diffraction

Electron backscatter diffraction is a technique and a type of supplementary detector for SEM, which provides this technique. It allows the crystallographic structure of a material to be obtained, including crystal orientations and phases. The working principle is the same as in SEM; however, a specimen is placed at a highly tilted angle (~70°) to the electron beam in this case, and the detector itself is somewhat perpendicular to the beam. Fundamentally, the secondary electrons which are induced by the primary ones diffract and form Kikuchi lines – characterizing diffraction patterns. The orientation of Kikuchi lines depends on the orientation of a crystal that creates diffracting electrons, so it gives insight into how the crystal is oriented with respect to the detector plane, as shown schematically in Figure 16.

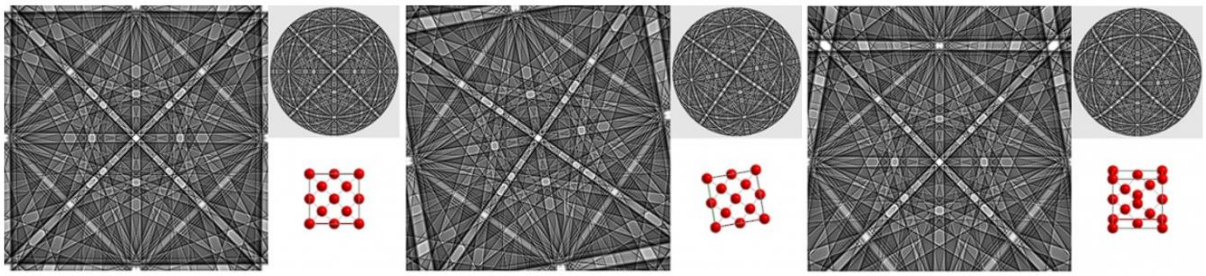

Figure 16. Spherical diffraction patterns (Kikuchi lines) generated by different orientations of the cubic structure. Generated using Bruker ESPRIT software [63].

At the end of EBSD scanning, an EBSD map is formed. It provides the morphology of the surface of a material, so the size and shapes of the grain/phase can be observed, and their orientations are associated with a color. A more detailed description of both SEM and EBSD can be found in [64].

2.3.3 Transmission electron microscopy

Transmission electron microscopy is an electron microscopy technique in which the electron beam is transmitted through a sample to create an image. To perform TEM, the studied section of a specimen must be ultrathin: around 100 nm thick. The principle is based on the scattering of electrons, depending upon the compositional density and crystal orientation of the observed area of the specimen. Scattered electrons disappear from the beam that comes to the detector, creating contrast in the final image. TEM is widely used in material sciences to study the inner microstructure, in particular, crystal defects. In this work TEM is applied to estimate the dislocation densities of the materials studied. To calculate this quantity, one draws a circle at random position of the TEM micrograph and counts the number of intersections between this circle and the dislocation lines. Then the equation is used:

$$\rho = \frac{2N}{Lt} \tag{2.12}$$

where ρ – is the dislocation density, N – the number of intersections, L – is the circle circumference, and t – is the total thickness of the specimen in the taken area of the image, which is determined from the electron diffraction pattern of the convergent beam, obtained

during microscopy. Usually, this calculation is performed several times in different locations, and the average value is then presented. Within the presented work, dislocation densities are corrected for extinction conditions, assuming that all line dislocations have Burger's vector $a/2\langle 111\rangle$ (a is the lattice parameter of BCC iron). A more detailed explanation about the technique is described in [65].

2.4 Crystal plasticity theory

The commonly applicable physical elastoplasticity models for FEA (such as von Mises (J_2) plasticity [66]) are isotropic, as they simplify and average the anisotropic microscale effects in crystals. This assumption justifies itself when the simulated deformations are on scales significantly higher than the expected anisotropy. Because the fine-structured many-grain cluster of a studied polycrystalline material neglects the anisotropy effects, the averaging is somewhat more representative in such cases. However, if the deformation scales are comparable to the size of a single crystal, the elastoplastic behavior may vary with respect to the direction of the applied force. In that case, one must account for the anisotropy effects and consider the crystallographic orientations as an additional parameter.

For this, crystal plasticity theory is developed. It is known that the main mechanism responsible for plastic deformation in metals is shear inside separate grains, whereas the main carriers of plasticity are dislocations gliding in slip systems. Considering the crystallographic orientations and anisotropy they create, the deformed grains can change in terms of their shape (deformation) and orientation (rotation). Crystal plasticity is a comprehensive theory of crystal deformations, which considers the anisotropic nature of the dislocation slip and takes into account the crystal orientations with respect to the external loadings or adjacent crystals [67]. It originates from the contribution of Taylor [47] and is based on the assumption that macroscopic plasticity is a superposition of slips in all activated slip systems. The activation of a slip system may occur if the resolved shear stress in it reaches a critical value. The main conceptual advantage of CP models is their ability to combine a variety of mechanical effects considering their dependence on the direction of the crystal orientation. Another advantage is the existence of dislocation density-based CP models (counter to the phenomenological CP models), which account for dislocation defects as the main carriers of plastic deformation. Obviously, computational implementation of the crystal plasticity approach is more demanding than that of the isotropic models.

If one is dealing with the deformation of a single crystal, then the above-described assumption is straightforward. However, once switching to a polycrystalline, additional assumptions must be made to include the interactions of neighboring grains. For many years, crystal plasticity models in polycrystals have been relying on simplified assumptions of Sachs or Taylor, correspondingly according to whom all grains undergo either the same stress, or the same strain as the whole macroscopic crystal. CP based on these assumptions is called "mean-field". These simplifications cannot simultaneously ensure the strain compatibility or the stress equilibrium at the grain boundaries, whereas in real polycrystals they are achieved by non-uniform stresses and strains.

The transition between the single crystal calculations to the polycrystals or between the microscale and the macroscale is called "homogenization". CPFEM allows one to create representative single and polycrystalline structures and apply to them complex boundary conditions. In the presented manuscript, both mean-field homogenization and computational (in terms of utilizing CPFEM) homogenization are applied. A model implementing crystal plasticity theory can be coupled with an FEM solver, thus giving the possibility to establish a geometrical representation of a studied problem on the macroscale but still be based on the microscale anisotropic features.

2.4.1 Crystal plasticity model and slip plasticity formulation

The computational analysis in the presented work has been done by coupling a user-defined material law (UMAT subroutine) that implements crystal plasticity theory with a FEM solver. The solver is combined with the open source three-dimensional finite element mesh generator with a built-in CAD engine: gmsh [68]. The CM3 libraries FEM solver [69] was developed in the Department of Aerospace and Mechanical Engineering of Liege University in Belgium, while the crystal plasticity routine was developed by Delannay et al. [70] [71]. In the covered research, two types of elements were used: tetrahedral elements for the nanoindentation simulations and hexahedral elements for the flat tensile simulations. The elements are 1st-order, where the volumetric deformation is averaged to avoid shear locking.

2.4.1.1 Modeling of plastic deformation

Plastic deformation in metals occurs by activation and glide of dislocations, as well as by grain boundary deformation at high temperature and/or high strains or by twinning at low temperature and fast deformation. In this research, plasticity is assumed to be caused only by the glide of dislocation, since this is the main mechanism relevant to structural materials. The strain rate is then controlled by the rate at which the dislocations are released from the pinning points, which is thermally activated and driven by the applied stress. Thermal activation and obstacles overcome by dislocations are predicted by an Arrhenius-type equation [72] [73], where the frequency of backward jumps at low stresses is controlled by the hyperbolic sine function [74]. The dislocation slip rate $\dot{\gamma}^{\alpha}$ in a slip system α may be expressed as a function of the shear stress τ_{α} in this slip system [75], however adapted to include the athermal stress characteristic of BCC metals at high temperatures [76]:

$$\dot{\gamma}^{\alpha} = \dot{\gamma}_0 \, exp\left(-\frac{G_0 \mu b^3}{k_b T}\right) 2 \, sinh\left[\frac{G_0 \mu b^3}{k_b T}\left(1 - \left(1 - \left(\frac{\tau_{\alpha} - \tau_c}{\hat{\tau}}\right)^{p}\right)^{q}\right)\right] \tag{2.13}$$

In this expression, $2H_k = G_0 \mu b^3$ represents the value of the kink-pair formation enthalpy for a screw dislocation, where $\mu = (C_{11} - C_{12} + 2C_{44})/4$ is the shear modulus, b is the magnitude of Burger's vector, and G_0 is a constant. $\dot{\gamma}_0$ is a reference slip rate, $k_b T$ is the product of Boltzmann constant and temperature, and p and q are constants describing the profile of Peierls potential barrier, being equal to 0.5 and 1.5 respectively [77]. Critical resolved shear stress (CRSS) is controlled by two terms: the athermal stress τ_c typical for BCC metals and thermal stress $\hat{\tau}$, which determines thermal sensitivity of the plastic flow.

Athermal stress can be expressed as a function of dislocation density according to the dispersed barrier hardening model [78]:

$$\tau_c = S_0 + h_{dis} \mu b \sqrt{\rho} \tag{2.14}$$

where h_{dis} is the dislocation strength coefficient and S_0 represents the contribution of lattice friction stress and the Hall-Petch effect [79]. Even though this is the athermal contribution to CRSS, it is known that h_{dis} in BCC metals may depend on temperature [80]. ρ is the dislocation density which evolves according to the modified law proposed by Kocks and Mecking [81], where k_2 is computed from the saturated dislocation density value ρ_{sat} and remains constant, and the temperature and strain rate effects are controlled by the term ξ [82]:

$$\dot{\rho} = \left(k_1 \sqrt{\rho} - k_2 \xi \rho\right) \dot{\Gamma} \tag{2.15}$$

$$\rho_{sat} = \left(\frac{k_1}{k_2}\right)^2 \tag{2.16}$$

$$\xi = \left\{1 - \left(\frac{k_b T}{G_0} ln \frac{\dot{\gamma}_0}{\dot{\Gamma}}\right)^{\frac{1}{q}}\right\}^{-\frac{1}{p}} \tag{2.17}$$

where $\dot{\Gamma}$ is the sum of slip rates in all slip systems:

$$\dot{\Gamma} \triangleq \sum_{\alpha} |\dot{\gamma}_\alpha| \tag{2.18}$$

2.4.1.2 Mathematical formulation of the crystal plasticity model

The derivation of the model equations was inspired by several works on crystal plasticity [48] [83] [84] [80]. Under finite strains, the mapping from the undeformed (reference) configuration of a continuum (infinite number of material points) **x** into the deformed (current) configuration **y** is described by the second-rank deformation gradient tensor **F**. As commonly assumed in crystal plasticity theories, the deformation gradient is multiplicatively decomposed in: $\mathbf{F} = \mathbf{R}^*\mathbf{F}^{\mathrm{el}}\mathbf{F}^{\mathrm{p}}$, where $\mathbf{R}^*$ is an orthogonal matrix representing the crystal lattice rotation, $\mathbf{F}^{\mathrm{el}} = \mathbf{I} + \boldsymbol{\varepsilon}^{\mathrm{el}}$ is the elastic strain, (which is infinitesimal in metals, $\|\boldsymbol{\varepsilon}^{\mathrm{el}}\| \ll 1$), and $\mathbf{F}^{\mathrm{p}}$ – is the deformation caused by the dislocation slip. A spatial gradient **L** which quantifies the relative velocity between two positions of the current configuration is called velocity gradient and given by:

$$\mathbf{L} = \nabla \mathbf{v} \tag{2.19}$$

where **v** is a nonzero velocity field that representes a time-dependent displacement $\mathbf{u} = \mathbf{y} - \mathbf{x}$ and given by the time derivative of the corresponding displacement field:

$$\mathbf{v} = \frac{d\mathbf{u}}{dt} = \dot{\mathbf{u}} = \dot{\mathbf{y}} \tag{2.20}$$

The relation of the velocity gradient and the deformation rate $\dot{\mathbf{F}}$ can be derived from the equivalence of the relative change in the velocity of two points separated by $d\mathbf{y}$ and the deformation rate of their relative position:

$$\mathbf{L}d\mathbf{y} = \frac{\partial \mathbf{v}}{\partial \mathbf{y}} d\mathbf{y} \equiv \frac{d}{dt} d\mathbf{y} = \frac{d}{dt} \mathbf{F} d\mathbf{x} = \dot{\mathbf{F}} d\mathbf{x} = \dot{\mathbf{F}}\mathbf{F}^{-1} d\mathbf{y} \tag{2.21}$$

then, comparing the left-hand and right-hand sides of Eq. (2.21) and accounting that $\|\boldsymbol{\varepsilon}^{\mathrm{el}}\| \ll 1$, the velocity gradient tensor **L** can be decomposed as:

$$\mathbf{L} = \dot{\mathbf{F}}\mathbf{F}^{-1} \cong \dot{\mathbf{R}}^*\mathbf{R}^{*\mathrm{T}} + \mathbf{R}^*(\dot{\tilde{\boldsymbol{\varepsilon}}}^{\mathrm{el}} + \dot{\mathbf{F}}^{\mathrm{p}}\mathbf{F}^{\mathrm{p}-1})\mathbf{R}^{*\mathrm{T}} = \mathbf{R}^*\left(\underbrace{\mathbf{R}^{*\mathrm{T}}\dot{\mathbf{R}}^*}_{\tilde{\boldsymbol{\Omega}}^*} + \dot{\tilde{\boldsymbol{\varepsilon}}}^{\mathrm{el}} + \underbrace{\dot{\mathbf{F}}^{\mathrm{p}}\mathbf{F}^{\mathrm{p}-1}}_{\mathbf{L}^{\mathrm{p}}}\right)\mathbf{R}^{*\mathrm{T}} \tag{2.22}$$

The tilde, which is adjoined on top of three second-order tensors, highlights the fact that they apply to the "unrotated configuration". In this configuration, the velocity gradient is additively decomposed into a skew-symmetric tensor $\dot{\widetilde{\mathbf{\Omega}}}^*$ called the lattice spin (i.e. rate of crystal rotation), $\dot{\widetilde{\boldsymbol{\varepsilon}}}^{\mathrm{el}}$ which is a symmetric elastic strain rate and $\mathbf{L}^{\mathrm{p}}$ which is a plastic velocity gradient. Moreover, they are the most conveniently expressed in a coordinate frame that rotates with the crystal frame. Therefore, they will be called "co-rotational" tensors.

The anisotropic elastic stiffness operator $\mathbf{C}$ then allows to compute the co-rotational Cauchy stress $\widetilde{\boldsymbol{\sigma}} = \mathbf{C}: \widetilde{\boldsymbol{\varepsilon}}^{\mathrm{el}}$. The plastic velocity gradient will be equal to:

$$\mathbf{L}^{\mathrm{p}} = \sum_{\alpha} (\mathbf{b}^{\alpha} \otimes \mathbf{n}^{\alpha}) \dot{\gamma}_{\alpha} = \sum_{\alpha} \mathbf{M}^{\alpha} \dot{\gamma}_{\alpha} = \sum_{\alpha} (\mathbf{M}^{\alpha}_{sym} + \mathbf{M}^{\alpha}_{skw}) \dot{\gamma}_{\alpha} \tag{2.23}$$

where $\mathbf{b}^{\alpha}$ and $\mathbf{n}^{\alpha}$ are unit vectors along the Burger's vector and normal to the α^{th} slip plane. The dislocation slip rate $\dot{\gamma}^{\alpha}$ in the slip system α is calculated by Eq. (2.13). $\mathbf{M}^{\alpha}$ is the Schmid tensor, dyadic product of two vectors, subdivided into a symmetric $\mathbf{M}^{\alpha}_{sym}$ and a skew-symmetric $\mathbf{M}^{\alpha}_{skw}$ part. The material response is calculated incrementally by time integration using a Newton-Raphson scheme [85] under an above-mentioned velocity gradient expressed as $\mathbf{L} = \mathbf{D} + \mathbf{W}$, where $\mathbf{D}$ and $\mathbf{W}$ are symmetric and skew-symmetric strain rate tensors respectively. The set of differential equations is built by separating symmetric and skew-symmetric tensors:

$$\begin{cases} \dot{\widetilde{\boldsymbol{\sigma}}} = \mathbf{C}: \left(\mathbf{R}^{*\mathrm{T}} \cdot \mathbf{D} \cdot \mathbf{R}^{*} - \sum_{\alpha} \mathbf{M}^{\alpha}_{sym} \dot{\gamma}_{\alpha} \right) \\ \dot{\widetilde{\mathbf{\Omega}}}^{*} = \mathbf{R}^{*\mathrm{T}} \cdot \mathbf{W} \cdot \mathbf{R}^{*} - \sum_{\alpha} \mathbf{M}^{\alpha}_{skw} \dot{\gamma}_{\alpha} \end{cases} \tag{2.24}$$

Time integration of the material law is implicit and solved incrementally. As the increments of dislocation slip $\Delta\gamma_{\alpha} = \dot{\gamma}_{\alpha} \Delta t$ depend on the stress, there remain 9 independent unknown variables in the set of non-linear equations: the six components of the co-rotational stress increment $\Delta\widetilde{\boldsymbol{\sigma}}$ and the three independent components of the skew-symmetric tensor $\Delta\widetilde{\mathbf{\Omega}}^{*} = \dot{\widetilde{\mathbf{\Omega}}}^{*} \Delta t$ representing the increment of lattice rotation:

$$\begin{cases} \Delta\widetilde{\boldsymbol{\sigma}} = \mathbf{C}: \left(\mathbf{D}|_{t+\Delta t} \Delta t - \sum_{\alpha} \mathbf{M}^{\alpha}_{sym} \Delta\gamma_{\alpha} \right) \\ \Delta\widetilde{\mathbf{\Omega}}^{*} = \mathbf{W}|_{t+\Delta t} \Delta t - \sum_{\alpha} \mathbf{M}^{\alpha}_{skw} \Delta\gamma_{\alpha} \end{cases} \tag{2.25}$$

The fully implicit time integration is simplified by accounting for the fact that each time increment involves a sufficiently small increment of lattice rotation [86] to ensure that:

$$\mathbf{D}|_{t+\Delta t} = \mathbf{R}^{*\mathrm{T}}\big|_{t+\Delta t} \cdot \mathbf{D} \cdot \mathbf{R}^{*}|_{t+\Delta t} \cong \underbrace{\mathbf{R}^{*\mathrm{T}}\big|_{t} \cdot \mathbf{D} \cdot \mathbf{R}^{*}|_{t}}_{=\mathbf{D}|_{t}} - \Delta\widetilde{\mathbf{\Omega}}^{*} \cdot \mathbf{D}|_{t} + \mathbf{D}|_{t} \cdot \Delta\widetilde{\mathbf{\Omega}}^{*} \tag{2.26}$$

The $\mathbf{W}|_{t+\Delta t}$ is computed in the same way, thus depending only on the lattice rotation at the beginning of the time step $\mathbf{R}^{*\mathrm{T}}\big|_{t}$ and on the increment of rotation $\Delta\widetilde{\mathbf{\Omega}}^{*}$ which is determined in the Newton-Raphson solution.

2.4.1.3 Standalone mode Taylor-type modeling

The CP model can be used either standalone or coupled with a finite element solver (CPFEM mode). In the standalone mode, the model equations are applied to a theoretical (virtual) polycrystal with one material point, in which every grain undergoes the same strain as the polycrystal as a whole (Taylor mean-field crystal plasticity model [47]). The grains of this virtual polycrystal cannot be defined in terms of their geometrical shape and size, and their arrangement cannot be prescribed. Thus, the effect of these factors on the mechanical response is not taken into account. However, a specific crystallographic texture may be assigned to the polycrystal. Even though the iso-strain assumption makes the approach less realistic than CPFEM, the standalone calculations rely on the same mathematical modeling of dislocation slip and allow us to capture the main macroscopic trends.

2.4.2 Strain gradient crystal plasticity models

Strain gradient crystal plasticity is a highly effective approach once it is used for nanoindentation FEM simulations. However, for several reasons, it is not applied in the presented research. Herewith, the presence of this chapter is driven by the ubiquitous mentioning of this method throughout the text.

The reason for the importance of the strain gradient theory in nanoindentation simulations is the indentation size effect, commonly present in each nanoindentation test. During the ISE, the measured hardness value is significantly increased on shallow depths, gradually lowering its contribution with further depth evolution. One can see the indentation size effect on hardness-depth profile presented in Figure 17.

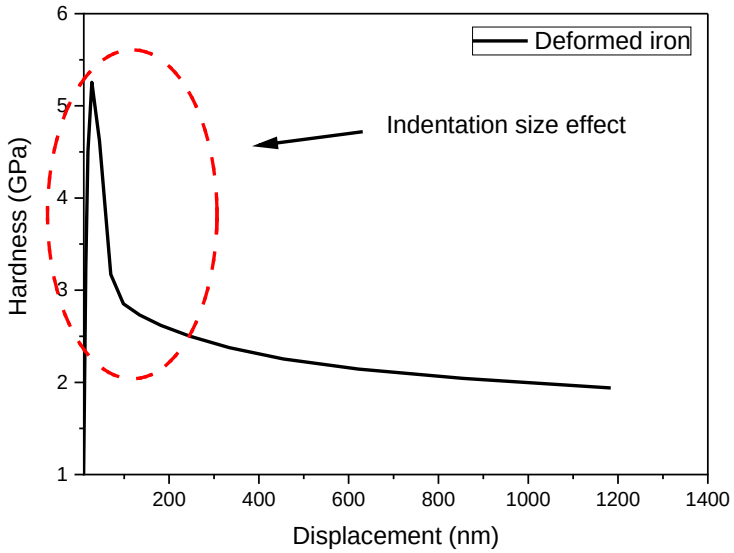

Figure 17. Hardness-depth profile of a deformed pure iron product.

Physically the indentation size effect is associated with the geometrically necessary dislocations (GNDs), in addition to the naturally present statistically stored dislocations (SSDs). GNDs appear to accommodate plastic bending in crystals, where the deformation levels are low enough to be ensured by the SSDs. The bending curvature in a body creates tensile strain in the upper part and compression strain in the lower part, thus providing its shape incompatibility or a strain gradient. The nanoindentation process at the very beginning of the test represents such a bending, as the indenter tip is “bending” the surface of a crystal. Therefore, GNDs are created,

strongly contributing to hardness. When the depth is increasing, more and more SSDs control the plastic flow and the indentation size effect fades. Moreover, on the grain interfaces in polycrystallines, the GNDs play the role of intermediate plasticity carriers. Thus, they ensure the structural integrity of the deforming bicrystal units and produce increments of dislocation densities, which lead to hardening predicted by the Hall-Petch effect.

Fundamentally, the strain gradient crystal plasticity models are similar between each other, as they presume an introduction of terms responsible for the GNDs contributions and length scale factors controlling their presence. A good example of the implementation of the strain gradient model into the crystal plasticity framework for simulations of the nanoindentation process in ion-irradiated materials is provided by X. Xiao in [40]. A brief overview is provided. τ_c from the equation (2.14) can be extended by introducing a hardening term responsible for the GNDs. Therefore, the equation can be rewritten as follows:

$$\tau_c = S_0 + \sqrt{\left(h_{dis}^{SSD}\mu b\sqrt{\rho_{SSD}}\right)^2 + \left(h_{dis}^{GND}\mu b\sqrt{\rho_{GND}}\right)^2} \tag{2.27}$$

where h_{dis}^{SSD} is the dislocation strength coefficient for the SSDs, ρ_{SSD} is the SSDs density (controlled by the Kocks-Mecking model in Eq. (2.15)), h_{dis}^{GND} is the dislocation strength coefficient for the GNDs and ρ_{GND} is the GNDs density. The latter is determined by the plastic strain gradient, i.e.

$$\rho_{GND} = \left|\mathbf{n}^{\alpha} \times \sum_{\beta} \mathbf{b}^{\alpha} \cdot \mathbf{b}^{\beta} \nabla\gamma^{\beta} \times \mathbf{n}^{\beta}\right| \tag{2.28}$$

where $\nabla\gamma^{\beta}$ denotes the gradient of the dislocation slip strain γ on the β-th slip system. Eq. (2.28) shows that the density of GNDs is mainly controlled by the strain gradient in the localized region.

As for the macroscale axial loading modes the plastic deformation tends to be homogeneous, the contribution from GNDs will not appear. On the other hand, nanoindentation, which creates non-uniformly localized stress fields close to the indenter tip and, therefore, generates GNDs with the consequent hardening behavior observed on the force-displacement and hardness-depth plots.

As has been said, this implementation is assumed and based on the development proposed and used by X. Xiao et al. Strain gradient theory is not used in the presented work and described to the reader because of often mentioning throughout the text.

Chapter 3. Development & experimental validation of the CPFEM model for the nanoindentation process in pure α-iron

The outcome results of this chapter have been published in Journal of Nuclear Materials in June 2022, and can be found in Ref. [59]. The data have been obtained in collaboration with other research groups; the contribution of everyone is highly acknowledged by the author: Prof. Ludovic Noels – guidance in the computational part, methodology; Dr. Dmitry Terentyev – guidance in the experimental part, methodology, conceptualization; Dr. Ude D. Hangen – nanoindentation experiments, methodology; Dr. Douglas D. Stauffer - methodology; Folke Dencker – nanoindentation experiments; Dr. Wouter Van Renterghem – FIB/TEM investigations; Dr. Andrii Dubinko – TEM investigations; Chih-Cheng Chang – tensile testing; Dr. Aleksandr Zinovev – guidance in the computational part; Prof. Laurent Delannay – guidance in the computational part. The author himself participated in the methodology, conceptualization, computational analysis, tensile testing, specimen preparation and SEM/EBSD investigations.

According to the methodology presented in §1.2.2, the establishment of the CPFEM temperature-dependent model calibrated with tensile tests data and its validation with nanoindentation tests for unirradiated α-iron consists of the following steps:

1. **Experimental characterization**: To describe the material law and get an idea of the mechanical performance of the material, a set of experiments must be performed. In our case we apply tensile tests data and nanoindentation in a range of temperatures for the reference and ion-irradiated materials.

2. **Microstructure characterization**: Microstructural properties play an important role in the model constitution, as well as in understanding of the computational results.

3. **Selection of the constitutive parameters**: coming from three sources: experimental, literature and fitting, the constitutive parameters are found for reproduction of the experimental tensile stress-strain curves.

4. **Simulations of the nanoindentation process**: FEM geometry and boundary conditions setup for the nanoindentation process is developed, then the established constitutive parameters (i.e. material law) are transferred into it. The output is compared with the experimental data.

5. **Post-processing**: analysis of the FEM maps, output curves, geometrical features, etc.

Once all of the steps mentioned above are performed successfully, we will obtain an experimentally validated, dislocation density-based material law, which provides the interconnection between macro-tensile and micro-/nano-compressive deformation through the CPFEM simulations of the nanoindentation process. This law can be transferred to other simulations of the conventional or non-standard tests, and upon validation, provide a certain level of computational reproducibility. This reproduction comes with an extended analysis of the studied deformation process (nanoindentation in our case) provided by the FEM maps of various quantities, access to additional boundary conditions or testing parameters, related geometrical features, and many more.

Unirradiated pure α-iron is used as a probe material to investigate the efficiency of the developed method. Upon confirmation of its applicability, the methodology can be extended by the introduction of complicated microstructure features typical for RAFM steels, as well as the effect of irradiation. This approach is discussed in §1.2.2.

3.1 Material production and chemical composition

The technically pure iron was produced by OCAS (Gent, Belgium) by additive melting using an induction furnace with vacuum chamber. A piece of the produced material was introduced into a preheated furnace at 1200°C for 1 h and then hot rolled without interruption. The final stage was air cooling to room temperature. The approximate eventual dimensions of the sheet were 10 × 250 × 600 mm^3.

To determine the chemical composition, two types of spectroscopies were used: spark source optical emission spectroscopy to quantify all elements except Ni, Si, and Al, and inductively coupled plasma optical emission spectroscopy to estimate Ni, Si, and Al concentrations. The nominal chemical composition is presented in Table 2 [45].

Cr	**Ni**	**P**	**Al**	**Si**	**V**	**W**	**Cu**
0.002	0.007	0.003	0.023	0.001	< 0.0109	< 0.0099	< 0.0091
Mo	**Co**	**C**	**Nb**	**Ti**	**As**	**Sn**	
< 0.0082	< 0.0080	< 0.0067	< 0.0036	< 0.0020	< 0.0012	< 0.0010	

Table 2. Chemical composition of Fe in wt. %.

It is important to note, that due to the presence of C impurities at a concentration of 313 ppm (0.0067 wt.%), the material exhibits a significant dynamic strain aging effect [87]. This phenomenon affects the material response at some elevated temperatures, which lay in the range of interest; therefore, the usage of the data from tests done at those conditions was avoided. More detailed explanation will be provided in §3.2.1 and §3.2.2.1.

3.2 Experimental results

3.2.1 Tensile testing

The iron sheet described in §3.1 was used to cut miniaturized flat tensile specimens with dimensions of 1.5 × 4.2 × 16 mm^3 (5.2 mm gauge length) to perform uniaxial tensile deformation. Mechanical straining was done using an Instron electromechanical universal test machine equipped with a heating chamber and calibrated according to Belgian accreditation rules (BELAC). The elongation of the sample was measured by pulling rod displacement and force with a load cell with 50 kN maximum capacity. The cross-head displacement rate was 0.02 mm/min in order to establish the strain rate of $6.6 \cdot 10^{-5}$ s^{-1} to coincide with the previously performed tests of the studied material on larger samples [45]. The obtained curves in force-displacement cords were recalculated into engineering stress-strain by using the formulations (2.10).

Due to the presence of C impurities in a concentration of 313 ppm (0.0067 wt.%), the material exhibits a significant dynamic strain aging effect in the temperature range of 100 – 300°C. The influence of the dynamic strain aging effect on the flow stress during uniaxial

tension can be observed in Figure 18, where the engineering stress-strain curves are presented in the full temperature range.

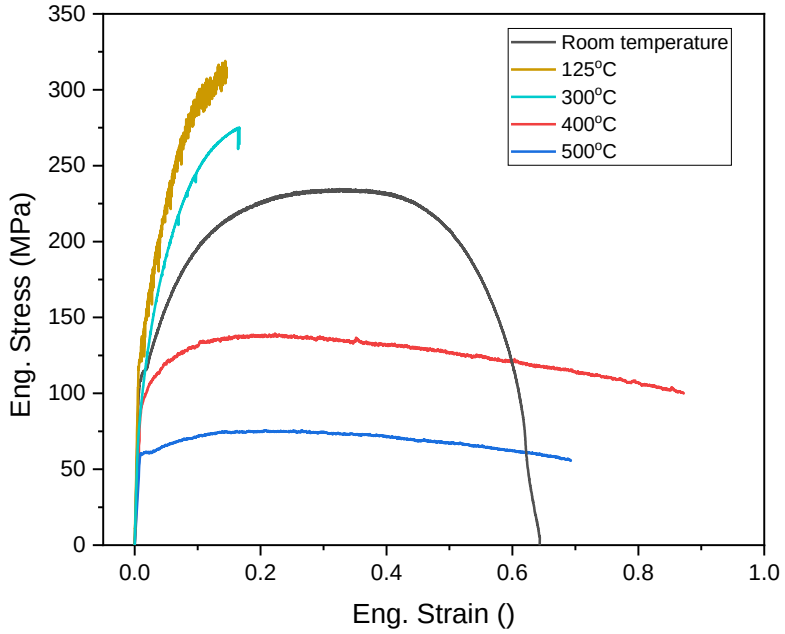

Figure 18. Engineering stress-strain curves of iron in a range of temperatures.

It can be seen in Figure 18 how yield stresses and hardening rates are strongly affected by the presence of carbon impurities during tests at 125°C and 300°C, and how the classical thermally activated yielding renews as the temperature increases. However, yield stress at 400°C still remains closer to the room temperature value, rather than 500°C, which means that dislocations are still weakly bonded by carbon impurities. Plastic deformation at 125°C also exhibits serrated yielding, which is also known as the Portevin-Le Chatelier effect [88].

Development of the nanoindentation model for the material where it has such a different from typical plastic behavior was out of the scope of this study, especially, since Eurofer97 as the main material for the model application does not exhibit this effect. However, it might still be possible within the modeling tools used. Therefore, the stress-strain curves obtained at 125°C and 300°C were avoided, and only room temperature, 400°C and 500°C were used for the validation of the FEM model input.

The presented in Figure 18 engineering stress-strain curves were corrected and processed in order to obtain the true stress-strain for further adoption of the model input. The machine compliance was removed by correction of the elastic part to the known value of Young's modulus of iron of 210 GPa. The following formulation was used:

$$\varepsilon_{eng_{corr}} = \varepsilon_{eng} + \sigma_{eng}\left(\frac{1}{E} - \frac{1}{E_{exp}}\right) \tag{3.1}$$

where E = 210 GPa and E_{exp} is the Young's modulus calculated from the tensile tests (approx. 23 GPa). Young's modulus was assumed to be constant for all temperatures. Further, the true stress-strain recalculations were applied to the corrected engineering curves. The obtained true stress-strain curves cut until UTS are shown in Figure 19.

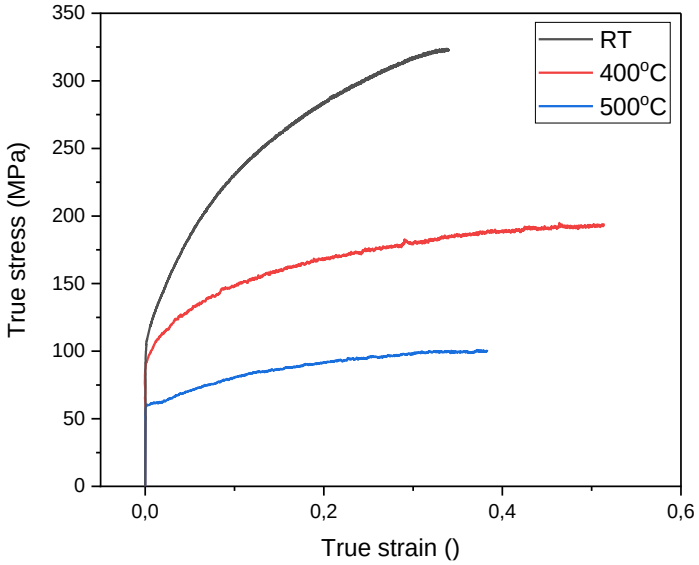

Figure 19. True stress-strain curves of iron with the applied corrections.

3.2.2 Nanoindentation

The iron specimens for the nanoindentation experiments were cut with dimensions of 10 × 10 × 1 mm^3. Prior to the tests, they had undergone one-sided mechanical grinding and polishing, using grinding papers. The surface preparation process was finalized using an active oxide polishing suspension "OP-U". The process is summarized in Table 3.

	Method	**Parameters**
Step 1	Mechanical grinding	1200 grit grinding paper
Step 2	Mechanical grinding	2000 grit grinding paper
Step 3	Mechanical grinding	4000 grit grinding paper
Step 4	Mechanical polishing	3 µm diamond suspension
Step 5	Mechanical polishing	1 µm diamond suspension
Step 6	OP-U	30 min

Table 3. Surface preparation process of iron samples.

The nanoindentation experiments from this chapter were performed using a high temperature nano-mechanical testing system from Bruker, the HYSITRON TI980 equipped with an xSOL 800 heating stage. The high temperature NI was carried out under a gas atmosphere (N_2 95at%; H_2 5at%) using a diamond indenter tip mounted by high temperature ceramic glue on a glass shank with low thermal expansion and low thermal conductivity. The xSOL stage allows for tight temperature control of both the specimen and indenter tip in a small microenvironment, the 3D drawing of the stage is given in Figure 20.

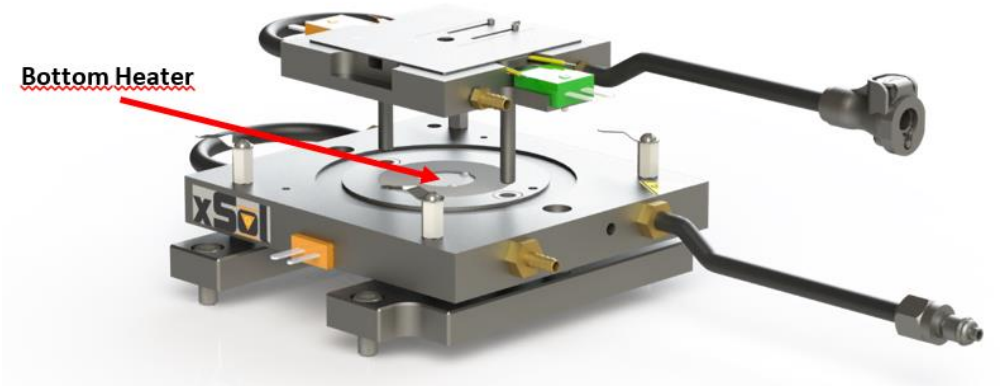

Figure 20. The schematic 3D drawing of the xSOL heating stage. The sample is placed on the bottom heater.

The specimen and indenter tip were located inside the xSOL heating stage, which establishes a uniform temperature zone, heated by two ceramic heaters (below and above the microenvironment). The heaters are embedded in thermally isolating ceramic foam and encapsulated by a water-cooled copper block and a copper cover that isolates the heated zone and helps to maintain the test temperature of the instrument. A gasket seals the microenvironment in the xSOL stage. The gas environment in the xSOL stage was controlled by a constant inflow of gas that exits the stage through the hole in the top cover, which enables optical observation of the sample with the light microscope and thereby also provides an access for the indenter tip. In the present study, Fourmier gas (N_2 95at%; H_2 5at%) was chosen to protect the diamond tip and to reduce the oxidation of the iron sample. However, to fully prevent oxidation at the highest temperatures of 400-500°C, a 20 nm SiO_2 layer was applied to the surface of the sample. The proof of the protection of the indentation area from oxidation is provided in Figure 21 as a comparison of the surfaces of two iron specimens with and without the application of the SiO_2 layer after the test at 500°C, made with an optical microscope. It clearly shows how the surface of the iron specimen is oxidized without the application of the SiO_2 layer and is protected in the other case.

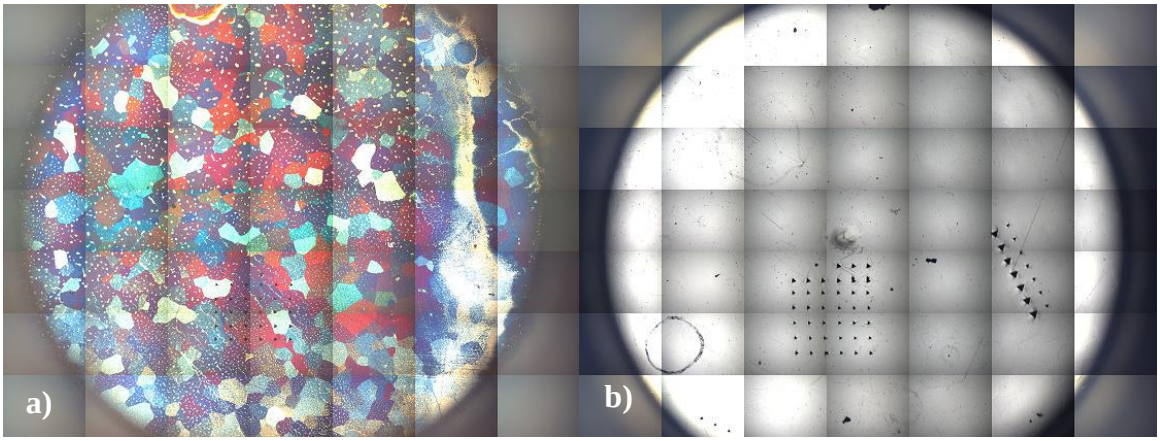

Figure 21. Iron surfaces tested at 500°C: a) without, b) with the protective SiO_2 layer.

The sample mounting does not involve any embedding or gluing and was realized by mechanical clamping. After the temperature equilibration was performed, a set of single cycle NI was carried out in the force control mode up to 250 mN of maximum load, F_{max}. Six to nine

standard measurements were performed for each condition using loading and unloading times of 5 s, applying a dwell time of 2 s, and spacing between indents of 50 µm. The test temperature has an absolute error of about 1 K, determined by the typical accuracy of the thermocouples, while the relative error on the temperature is as good as 0.01 K. Thermal drift is a time-dependent error in displacement that qualifies the holding stability of the indenter tip on the material surface due to the thermal expansions. Given that passive indenter heating was applied here, the thermal drift may increase during penetration of the indenter (cold finger effect) due to the heat evacuation via the indenter rod. The compensation for such temperature drift was realized by heating the indenter tip by the flowing gas. Both the sample and the tip were located in a small chamber heated from the top and the bottom. The tip was heated by the gas inside the chamber and the radiation from the heaters around the chamber. Moreover, the tip was mounted on a thermally isolated shank. The sample and the tip were therefore at nearly the same temperature. Thermal drift was measured for each single indentation and the average values are presented in Table 4 (negative and positive signs determine the direction of the indenter shift).

Temperature, °C	Thermal drift, nm/s
100	0.68 ± 0.78
200	-0.18 ± 0.28
300	-0.34 ± 0.45
400	-0.07 ± 0.1
500	-0.27 ± 0.17

Table 4. Thermal drift measured during nanoindentation testing of pure iron at high temperatures.

Additionally, the high loading rates used in this experimental run minimize the effect of thermal drifting, as the loading time is too low to accumulate significant parasitic displacement, whereas the high indentation depths reduce their impact in relation.

Indentation hardness values have been determined using the classic Oliver & Pharr method [61] and fitting a power law (Eq. (2.1)(2.2)) to the first segment of the unloading curve (from 95% to 20%). The tip area function and the frame compliance were calibrated on fused quartz as described by the ISO 14577 standard procedure [89].

3.2.2.1 Nanoindentation results

The force-displacement nanoindentation curves were obtained in the range of temperatures from room temperature to 500°C. Averaged curves are presented in Figure 22. Since at least six tests were done for each temperature in the force-controlled mode, the summarized result has a scatter by the displacement axis (due to a different material resistance depending on a grain orientation), the curves were averaged, where the deviation is shown by the *x* error bar. As expected, the increase of temperature suppresses the resistance of the material to plastic deformation, so the same 250 mN force immerses the indenter up to ~3 µm at room temperature, and up to ~4 µm at 500°C. One can also note that the hold at the maximum force shows an increase in the displacement with increase of temperature, which is the expected behavior due to the high temperature creep relaxation. This fact seems to affect nanoindentation pile-up behavior, so the overall pile-up height decreases with the temperature, which will be analyzed in detail in §3.3.2. Moreover, as it happens under tensile deformation, due to the carbon impurities still slightly impeding the dislocation movement at 400°C, the corresponding force-

displacement curve appears closer to that of the room temperature, rather than to that of 500°C. This phenomenon, as the well as measured force-displacement curves, can be observed in Figure 22.

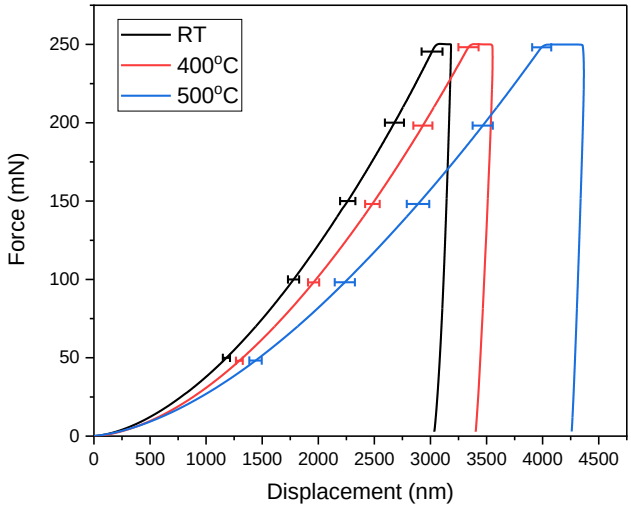

Figure 22. Averaged force-displacement curves for pure iron.

As discussed earlier, the presence of carbon in the material affects its plastic properties, creating dynamic strain aging effect. This is observed not only in the tensile stress-strain curves, but also in the nanoindentation force-displacement curves, which are presented in Figure 23.

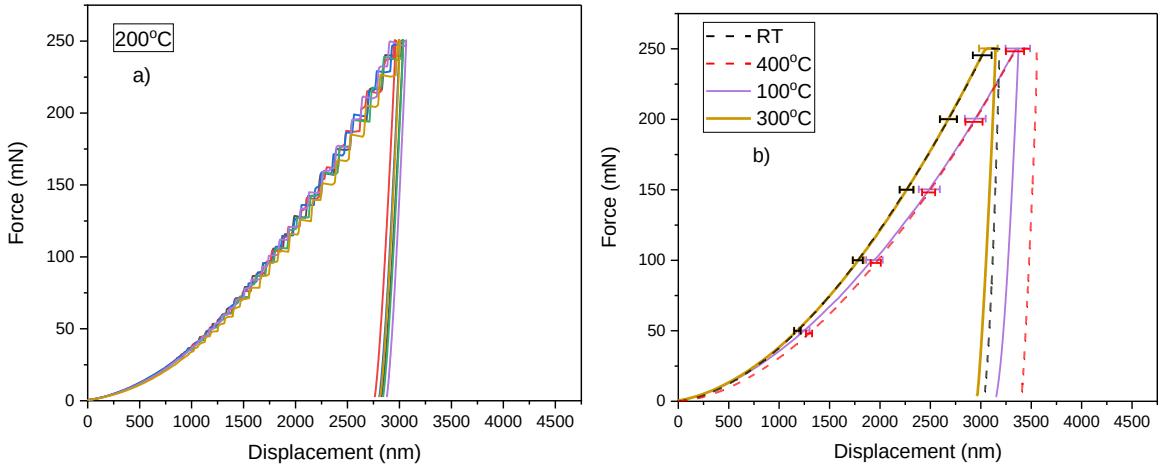

Figure 23. Force-displacement curves for pure iron affected by dynamic strain aging effect tested at: a) 200°C, b) 100°C and 300°C compared to room temperature and 400°C.

An interesting effect of the staircase loading can be seen in Figure 23(a). Such drops of force during the loading stage are associated with the previously discussed serrated yielding, which the material exhibits as well during uniaxial tension. In the case of 100°C and 300°C tests such a phenomenon was not found, however: a) the material resistance to the indenter immersion at 300°C is stronger than expected, so the force-displacement curve precisely matches the room temperature one instead of becoming softer; b) As the 400°C force-displacement curve is still slightly affected by the carbon impurities, it matches the one performed at 100°C.

It also seems that carbon suspends creep relaxation, as the shift in displacement during dwelling time is lower at these temperatures. To reflect the creep behavior, the creep rate (in nm/s) versus temperature plot is provided in Figure 24.

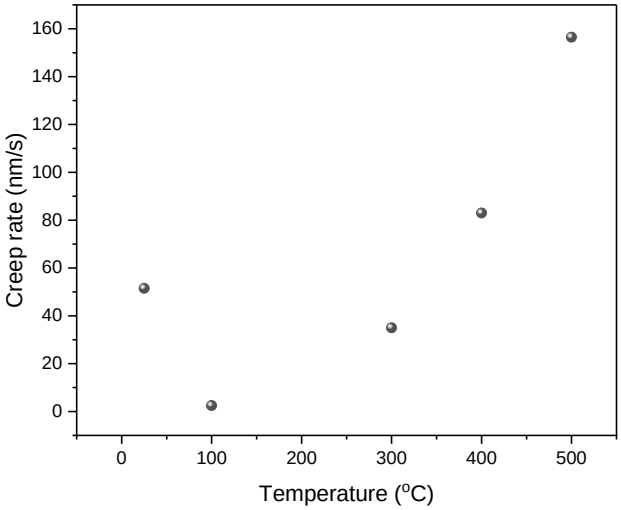

Figure 24. Creep rate versus temperature for pure iron.

Hardness and Young's modulus of iron versus temperature obtained by means of nanoindentation (Eq. (2.6) and (2.7)) are presented in Figure 25.

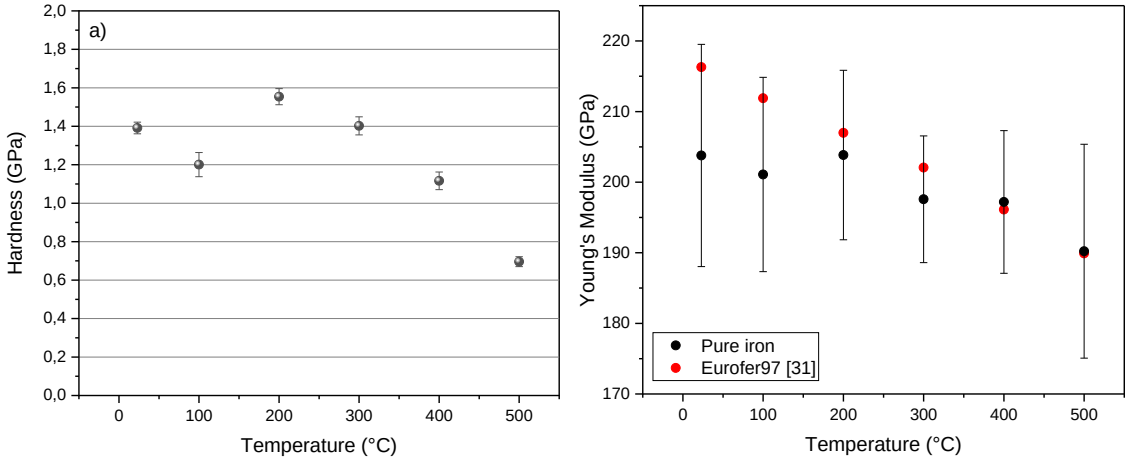

Figure 25. a) Hardness of iron versus test temperature; b) Young's modulus of iron (black) from the experiments compared to Eurofer97 [31] (red) measured by the E111-04 ASTM standard [90].

The influence of dynamic strain aging is very well seen in both Figure 24 and Figure 25(a). The former shows that the creep rate suspends at temperatures most favorable for dynamic strain aging to appear. The latter is the opposite, as hardness is significantly affected by the DSA in the approximate range from 200°C to 400°C. The normal temperature-dependent hardness trend is recovered at room temperature, 100°C and 500°C almost linearly reducing from ~1.4 GPa to ~0.7 GPa. On the other hand, the DSA-affected values reach almost 1.6 GPa at 200°C, ~1.4 GPa at 300°C and ~1.1 GPa at 400°C, which is not expected if the carbon content is lower. Nevertheless, the obtained Young's modulus values presented in Figure 25(b) and

compared to the ones of Eurofer97 obtained using the E111-04 ASTM standard are well matched and follow the expected trend of decreasing as temperature grows, although Eurofer97 is stiffer at lower temperatures. This behavior might be expected due to the characteristic microstructural features present in steel and alloying with 9% Cr and other minor elements.

The general conclusion about the plastic behavior of iron can be the following: strongly distorted properties such as hardness (nanoindentation), yield stress and hardening rate (tensile tests) in the temperature range of 100-300°C make the establishment of the constitutive laws for this material meaningless (but probably still possible). Moreover, as was said, the application of iron for nanoindentation CPFEM simulations in our case has appeared rather probationary than objective, and the main material of interest Eurofer97 does not exhibit any complexities in its thermally activated plastic behavior at the given temperatures. Nevertheless, the range of temperatures used for the experiments on iron has been wide enough to obtain both nanoindentation force-displacement and tensile stress-strain associated curves with the minimal or absent effect of dynamic strain aging, what makes them applicable for the CPFEM model validation.

3.3 Microstructure investigations

In order to correctly treat the CPFEM input and develop a proper model geometry, the morphology and microstructure of materials must be investigated. Scanning electron microscopy with electron backscatter diffraction module, and transmission electron microscopy were applied to analyze the grain size, grain orientations with respect to placed indentations, nanoindentation pile-ups scales, and dislocation densities in different locations and material states. As will be shown further, this information will be used either in the stage of model development or in validation.

3.3.1 Electron backscattered diffraction

EBSD was performed to draw conclusions regarding the grain size of the material. Additionally, one can see how the indents were placed with respect to different grain orientations. The iron inverse pole figure orientation map (IPFZ) calculated in the indented area using ATEX software [91] is presented in Figure 26.

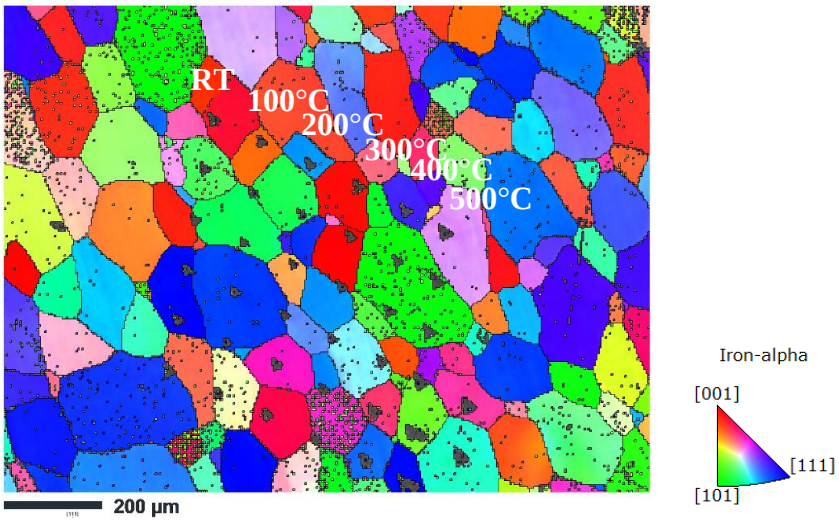

Figure 26. IPFZ EBSD map of iron in the indented area with the color legend.

The grain size of the material was determined as 113.41 μm.

The black triangles in the picture are nanoindentation imprints done in the range of temperatures. Each vertical row of six indents represents one temperature, so it goes from left to right as: room temperature, 100°C, 200°C, 300°C, 400°C and 500°C. 500°C tests were performed more than six times as something went wrong with the procedure and extra imprints were required. The observed morphology of iron is simple, since it consists of large and almost equiaxial grains.

3.3.2 Scanning electron microscopy on nanoindents

As the grain orientation map with respect to the placed indents has been obtained for iron, it is meaningful to observe the eventual shape of the indents depending on temperature and crystal orientations. Each indent is obtained with 250 mN force and reaches the maximum depth of around 3-4 μm, according to Figure 22. Images taken by using SEM are provided in Figure 27, Figure 28 and Figure 29.

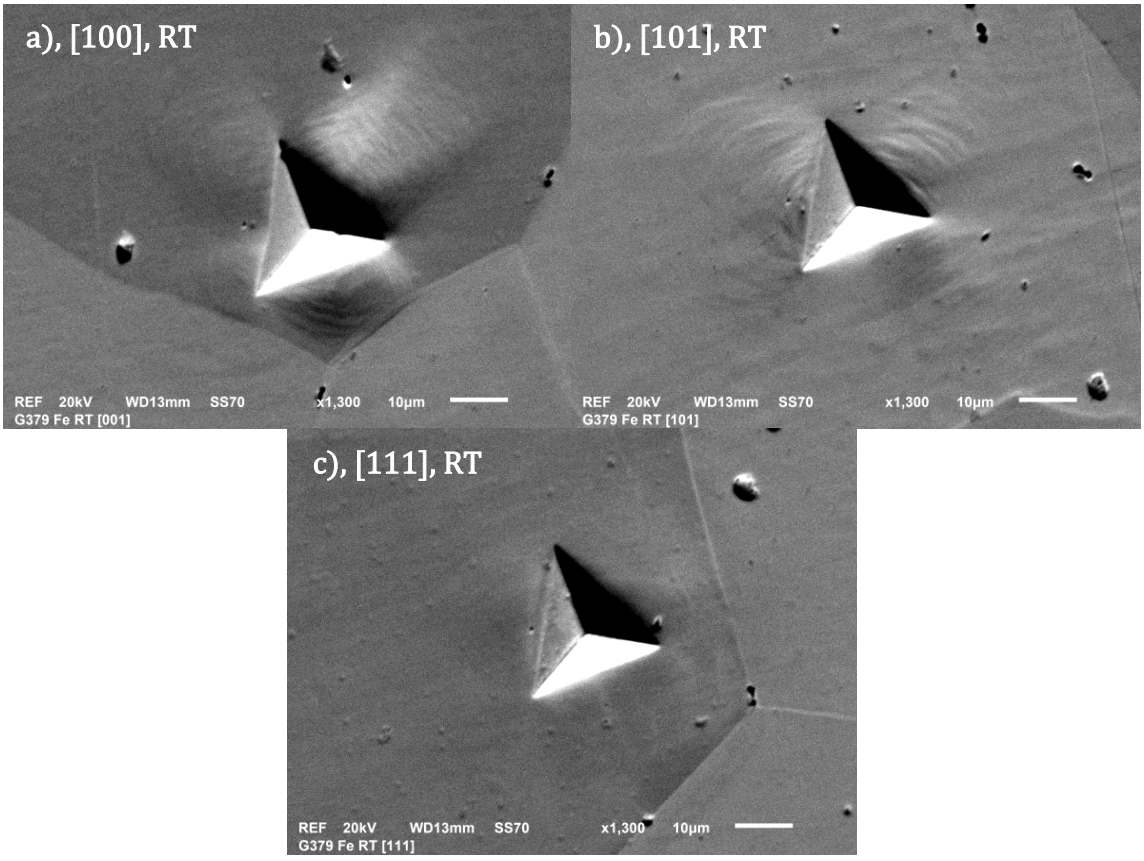

Figure 27. The shapes of nanoindents done on iron at room temperature into different surface orientations: a) [100], b) [101], c) [111].

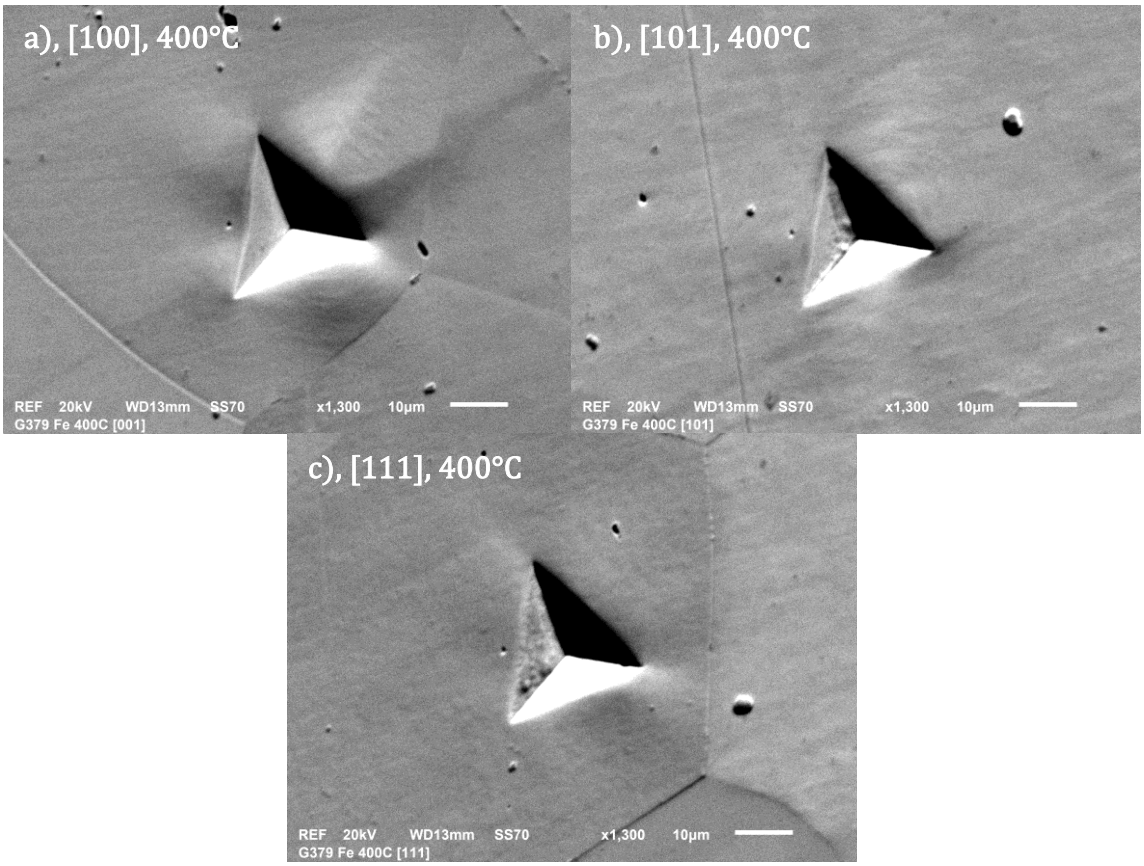

Figure 28. The shapes of nanoindents done on iron at 400°C into different surface orientations: a) [100], b) [101], c) [111].

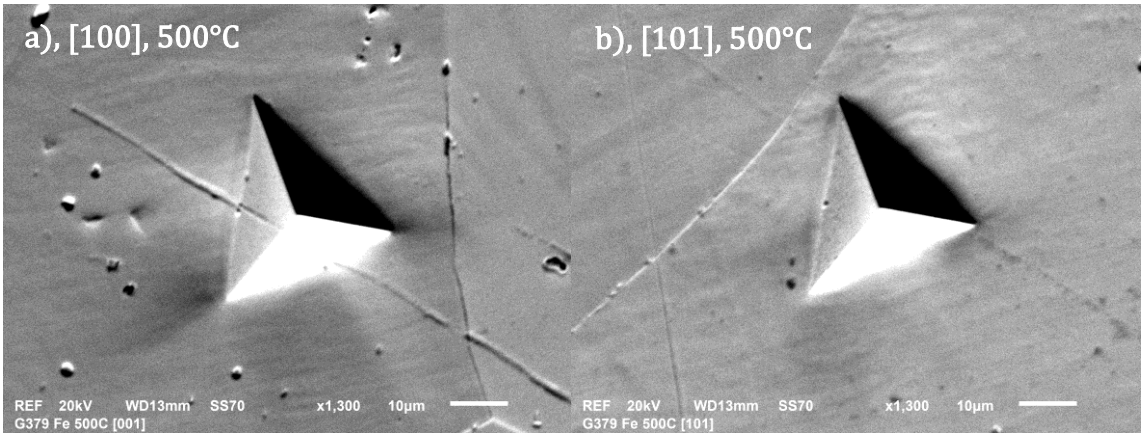

Figure 29. The shapes of nanoindents on iron done on iron at 500°C into different surface orientations: a) [100], b) [101].

It is impossible to estimate the exact height of the pile-ups using SEM, however, some features can still be observed. For all of the temperatures, the shapes of the pile-ups are different once placed on different orientations of the grains, as the active slip systems are also rotated with respect to the indentation direction. Also, the indents placed on [100] seem to be larger than others. The indent eventual shape and volume must also depend on the in-plane orientation of the crystal; however, no obvious proofs for this were found after examination of all of the

indents. Pile-up formation tends to decrease with increasing temperature, which is explained by the high temperature creep relaxation, discussed in detail in §3.2.2.1.

3.3.3 Transmission electron microscopy and scanning electron microscopy of the indented subsurface area

Another microstructure investigation of iron has been performed in combination with a focused ion milling technique. During focused ion milling, a focused ion beam is used to burn-out or deposit the material in a desired region, thus allowing to create nano-/microscale specimens with various complex shapes. Examples of such shapes are presented in Figure 30.

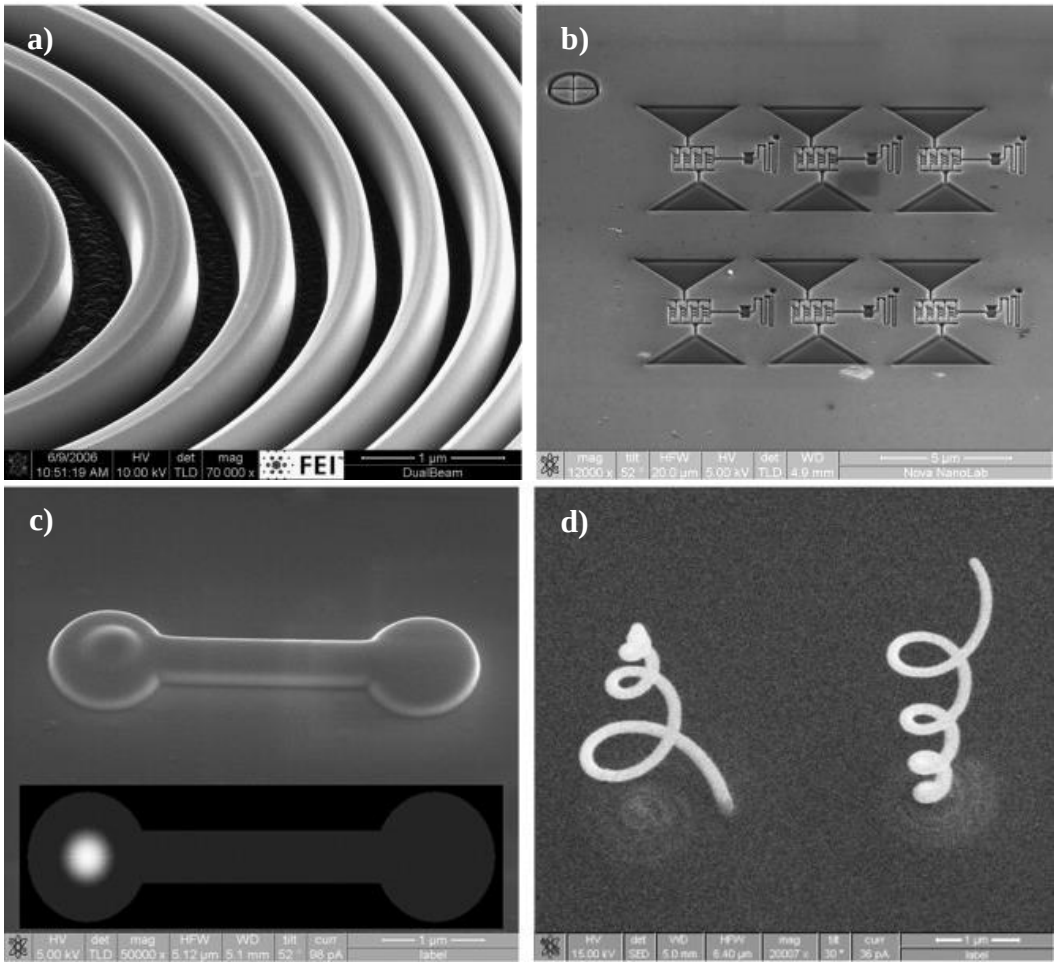

Figure 30. Structures formed by using a focused ion beam: a, b) focused ion milling; c, d) focused ion deposition; Reprinted from Micro and Nano Technologies, Wilhelmi O., Reyntjens S., Van Leer B., Anzalone P.A., Giannuzzi L.A., Handbook of Silicon Based MEMS Materials and Technologies: Chapter Twenty – Focused Ion and Electron Beam Techniques, 323-325, Copyright (2010), with permission from Elsevier [92].

Within this work, a ThermoFisher Scios FIB/SEM instrument was applied to carry out the visual inspection of the area taken from underneath the nanoindent. The microstructural investigation presented further was applied to 1.5 µm deep nanoindentations performed at room temperature. The preparatory steps are shown in Figure 31. First, an indent is selected and the area of interest is covered with a Pt layer to protect it from ions. It is placed over the deepest

place of the indent, so the analyzed area is located near the indenter tip, where the most significant damage is expected. Then, the lamella of approx. 10 × 10 × 0.2 μm^3 dimensions is cut free, lifted out of the sample, and attached to the TEM grid. Finally, the lamella is thinned, until its thickness is reduced to less than 200 nm.

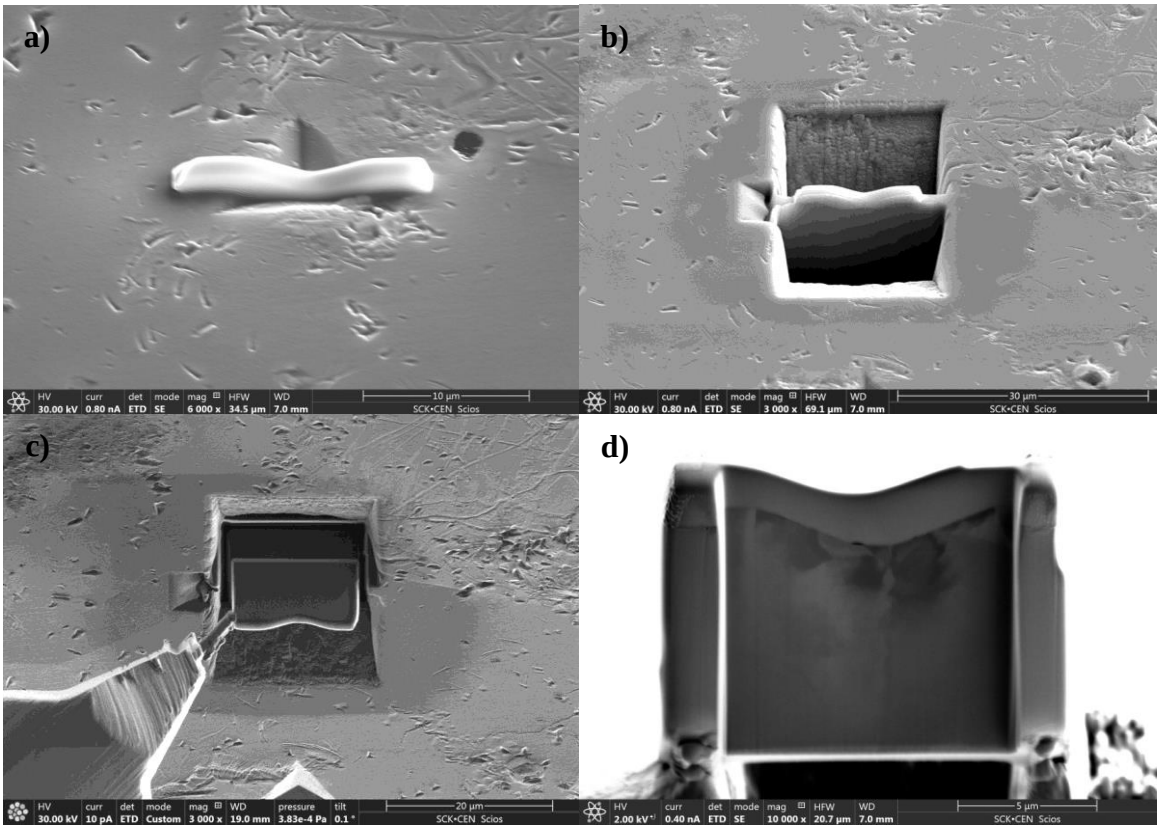

Figure 31. SEM images showing the different steps in the preparation of the lamella: a) deposition of the Pt layer, b) rough cut out, c) lift-out of the lamella, d) the lamella attached on the TEM grid.

The extracted lamella has been studied by means of SEM using backscattered electrons and secondary electrons modes, and then it has been inspected by TEM.

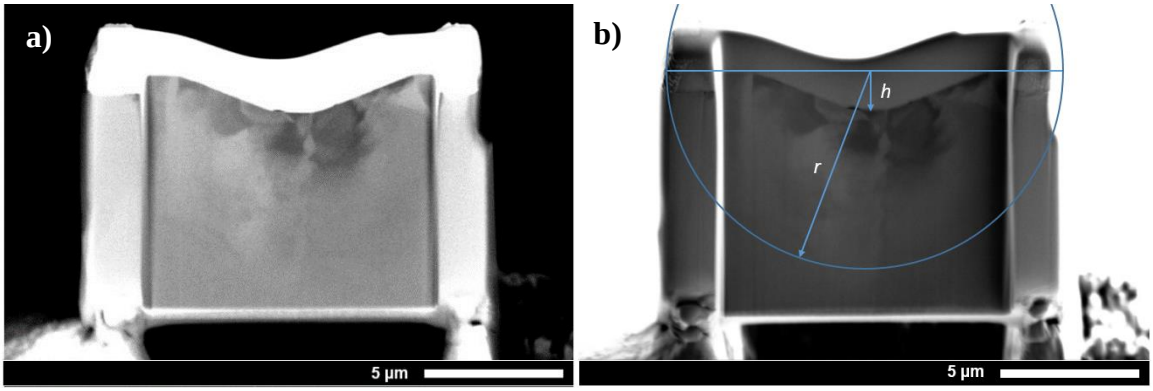

Figure 32. The lamella inspected with SEM taken from below the indent: a) BSE mode, b) SE mode with roughly estimated plastic zone radius.

The plastic deformation induced by the indentation process can be seen in Figure 32 thanks to the contrast in the BSE and SE images, while the indentation depth is well resolved due to the surface contour under the platinum layer. By rough estimation of the plastic zone hemisphere (see Figure 32(b)) the ratio of the indentation depth h = 1.5 µm to the plastic zone radius $r \approx 8$ µm is calculated as 5.3, which is in expected range of 5-10 for metals.

The second step was the characterization of the lamella by TEM. The main objective was to characterize the pattern of the dislocation density and to make an estimation of the variation of the dislocation density as a function of distance from the indent tip. The initial microstructure of the material (i.e. before indentation) was previously studied in [45] and will be further described in §3.3.4. Figure 33 and Figure 34 show the dislocation structure underneath the indent.

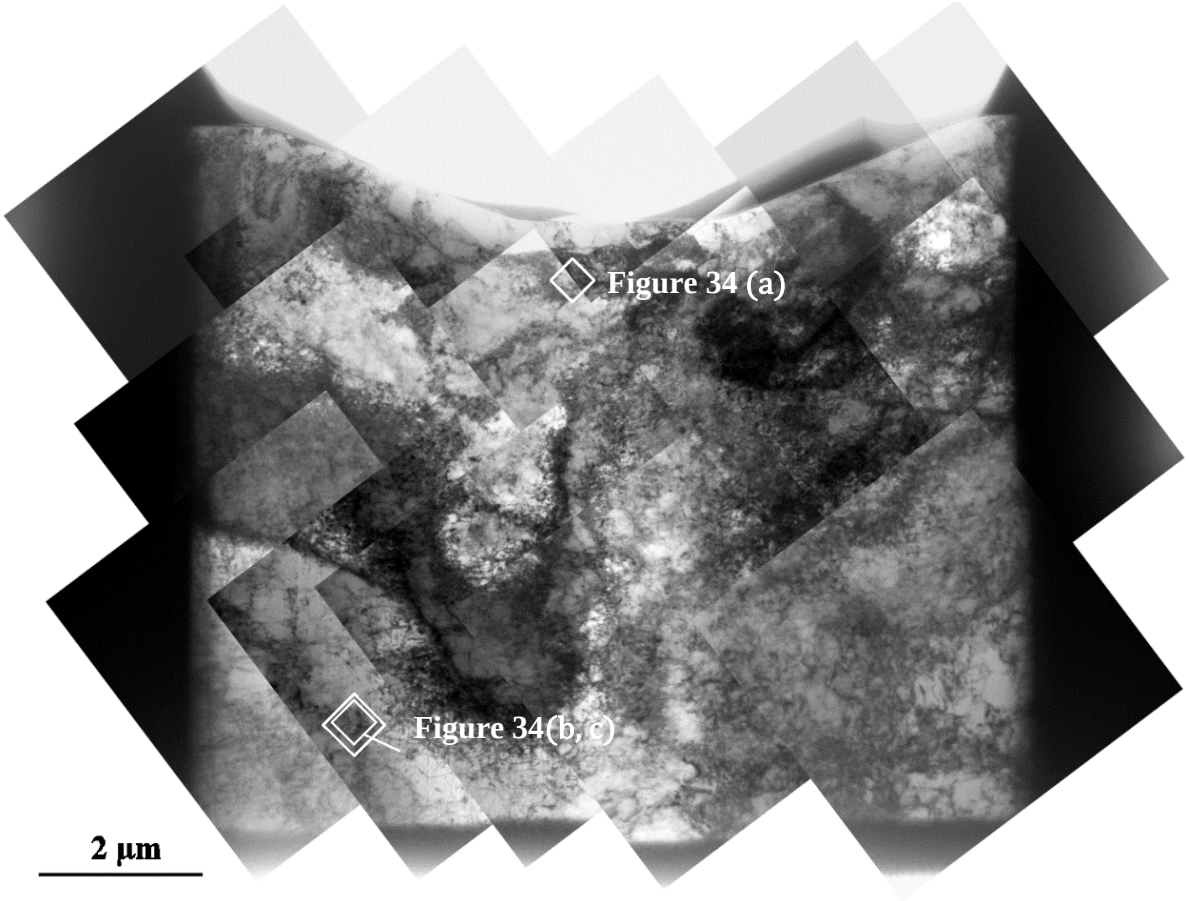

Figure 33. Composite picture of the dislocation structure in the lamella, extracted from the region underneath the indent, inspected by TEM.

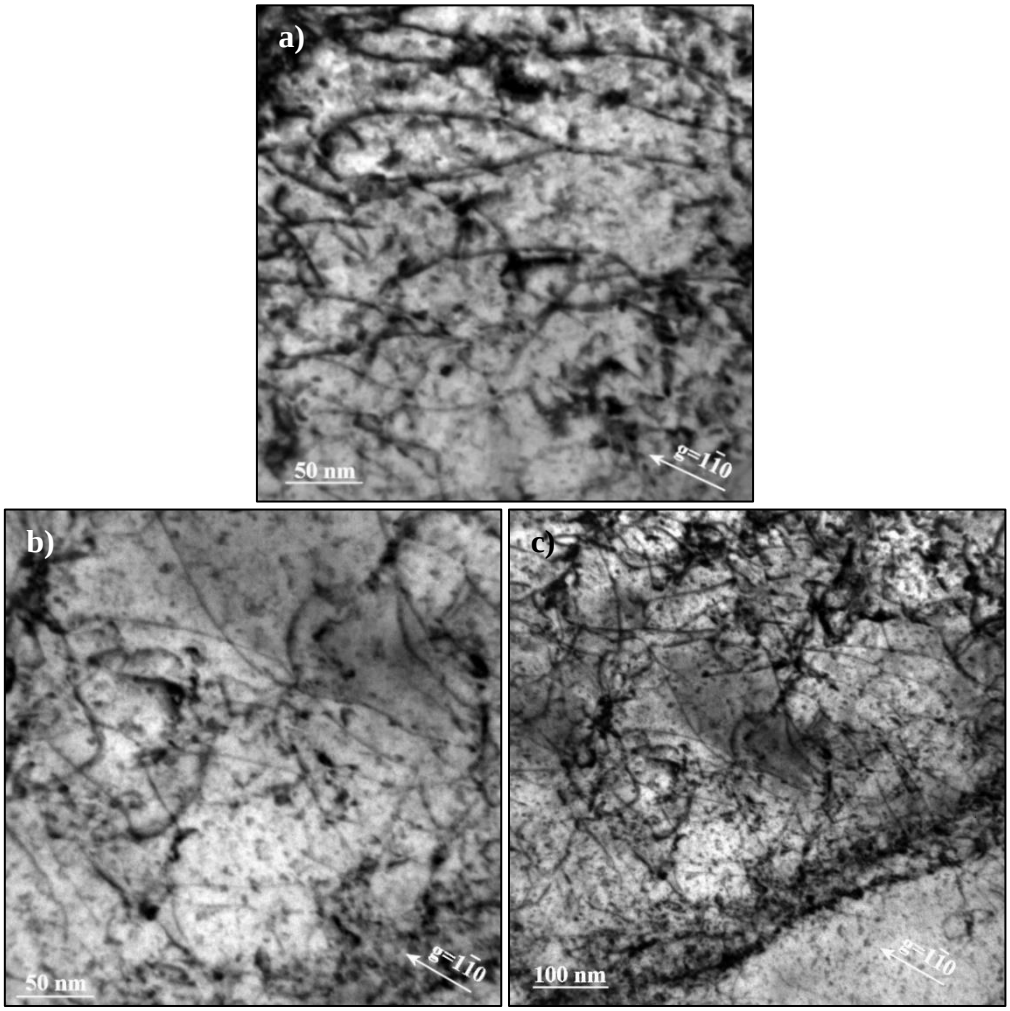

Figure 34. Dislocation structure in the specific places of the lamella inspected by TEM: a) dislocation structure near the tip, b) dislocation structure in the bottom of the lamella, c) dislocation slip band in the bottom area of the lamella.

TEM images presented in Figure 33 and Figure 34 were used to determine the dislocation density at three different locations on the lamella. Thus, the density of $1.37 \cdot 10^{15}$ m^{-2} (Figure 34(a)) near the tip of the indent, $0.91 \cdot 10^{15}$ m^{-2} (no microimage provided) in the middle of the lamella, and $0.85 \cdot 10^{15}$ m^{-2} (Figure 34 (b)) at the bottom of the lamella have been calculated. It should be noted that the precision of the individual measurements is very low, and even though the value suggests a higher density near the tip of the indent, the difference may not be statistically significant. The average dislocation density below the indent was calculated as $(1.0 \pm 0.2) \cdot 10^{15}$ m^{-2}.

In general, the dislocations are tangled and homogeneously distributed; however, there are some locations, for example, in the bottom part of Figure 34(c), where the dislocations are starting to form dislocation bands. The observed defect structure suggests that the stress induced by the indentation creates a high amount of dislocations, which move away from the indentation. The only obstacles for the dislocation glide are dislocations initially present in the non-deformed bulk material and dislocations created by the indentation (no grain boundaries were found within the lamella). This results in a high density of tangled dislocations. When the movement of the dislocations is blocked, dislocation bands can be formed which are oriented perpendicular to the movement of the dislocations. In this sample, several of such bands were

observed to be oriented roughly parallel to the sample surface. It agrees with the common understanding that the plastic deformation zone is created at and moves away from the indent. The observed dislocation bands propagate deeper into the material than it can be observed from the lamella, so the depth of the plastic deformation area is somewhat more than the size of the lamella and, therefore, larger than was assumed just by using SEM contrast fields.

3.3.4 Transmission electron microscopy in bulk

Transmission electron microscopy has been used to analyze the dislocation density of materials in different states and locations of the tensile test specimens. The presented TEM investigations have been performed using either JEOL 2010 operating at 200 kV or JEOL 3010 operating at 300 kV. The dislocation density is a key parameter which plays an important role in the establishment of a material law. It is fundamentally related to the plastic properties of crystals; therefore, the determination of this quantity and its evolution is necessary for the correct description of the response of the material to mechanical straining.

In the case of iron, TEM has been used to determine the dislocation densities in the as-received material state and after 15% straining of the tensile specimens. The reported average values were 10^{12} m^{-2} for the initial dislocation density and $2 \cdot 10^{14}$ m^{-2} after pre-straining at room temperature, so the evolution of the quantity with respect to uniaxial stress has been obtained. These investigations have been carried out for another work dedicated to nanoindentation of the same pure iron product and analysis of the consequent microstructural features, which can be found in [45]. TEM micrographs taken from [45] and unpublished data are shown in Figure 35.

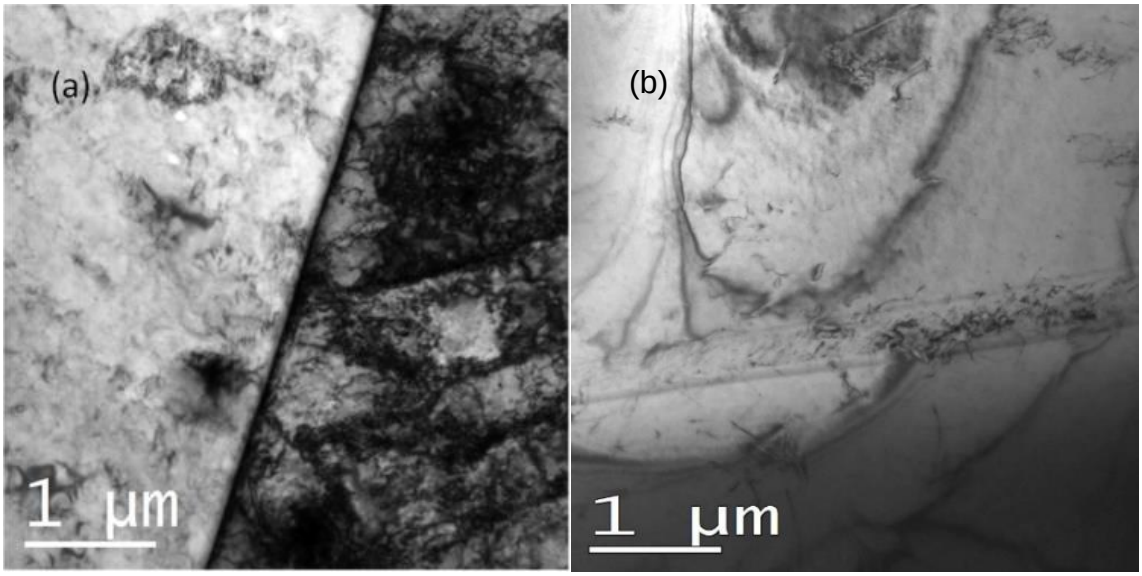

Figure 35. TEM images of the iron microstructure: a) pre-strained to 15% [45], b) as received.

The dark areas seen in Figure 35 represent locations where dislocation densities are high. The line crossing Figure 35(a) is a grain boundary, so one can see how the magnitude of dislocation density differs from one grain to another. This can happen due to one of the two reasons or concurrently both: the plastic strain can localize depending on the grain orientation with respect to the straining direction, or the primary electrons penetrating ability changes significantly with another grain orientation, thus creating the contrast.

3.4 CPFEM analysis of pure α-iron

3.4.1 Establishment of the material law using uniaxial tensile tests

To describe the elastoplastic behavior of the material, a set of parameters responsible for the formation of dislocation slip described in the paragraph §2.4.1.1 had to be determined. The following information needed to be compiled. The number of slip systems used was 24, the elastic constants C_{11}, C_{12}, and C_{44} were taken from [93] (assumed to be constant for all of the studied temperatures), Burgers vector was taken for the $\frac{a}{2}\langle 111\rangle$ dislocation (so the magnitude of the Burgers vector is $\sqrt{3}\frac{a}{2}$), where a is α-Fe lattice parameter of 2.856 Å [94] (assumed to be constant for all of the studied temperatures), initial and saturated dislocation densities were taken from the TEM measurements presented in §3.3.4, and the kink pair formation enthalpy was determined in Ref. [95]. However, the value used in the model was modified to correctly reflect the presence of carbon impurities, which are expected to interact with the kinks, effectively increasing the apparent activation energy (atomistic simulations describing such an interaction can be found here [96]). Other parameters had to be fitted in order to correctly reproduce the true stress-strain ($\sigma - \varepsilon$) curve shown in Figure 19.

Looking ahead, the set of the parameters had to be correctly transferred as an input for nanoindentation simulations, taking into account the difference in the Hall-Petch contributions. Given that the average grain size is 100 µm, even the deepest indent (4 µm depth) at 500°C having the maximum possible plastic zone radius of ~40 µm is not large enough for the dislocation movement to be effectively "blocked" by a grain boundary, while the dislocation-grain boundary interaction readily happens in the uniaxial tension of a polycrystalline sample. Therefore, the Hall-Petch stress contribution was neglected in the simulation of the nanoindentation, by reducing S_0 by 4 MPa with respect to the value calibrated from the tensile test. This was found to provide a better agreement with experimental data (compared to the case of inclusion of the Hall-Petch contribution).

The summary of the parameters applied in the set of constitutive equations is provided in Table 5.

Parameter	Value	Source
Elastic coefficient, C_{11}	230 [GPa]	Literature [93]
Elastic coefficient, C_{12}	135 [GPa]	Literature [93]
Elastic coefficient, C_{44}	117 [GPa]	Literature [93]
Burger's vector, b	0.2482 [nm]	Literature [94]
Reference slip rate, $\dot{\gamma}_0$	10^3 [s^{-1}]	Fitted
Lattice friction + Hall-Petch stress, S_0	21-13 (17-9) [MPa]	Fitted
Initial dislocation density, ρ_0	10^{12} [m^{-2}]	Measured
Kink pair formation enthalpy, $2H_k$	2.365 [eV]	Literature [95]/Artificially increased [96]
Dislocations interaction strength, h_{dis}	0.21 – 0.07	Fitted
Saturated dislocation density, ρ_{sat}	$1.3\cdot10^{15}$ [m^{-2}]	Measured
Kocks-Mecking parameter, k_1	$1.3\cdot10^{8}$ [m^{-1}]	Fitted
Thermal stress, $\hat{\tau}$	47.0 [MPa]	Fitted

Table 5. The list of constitutive parameters used to simulate the material law of pure iron.

Some parameters, such as S_0 and h_{dis} required their adjustment with respect to the features of simulated tests and/or temperature. Their dependences are provided in Figure 36.

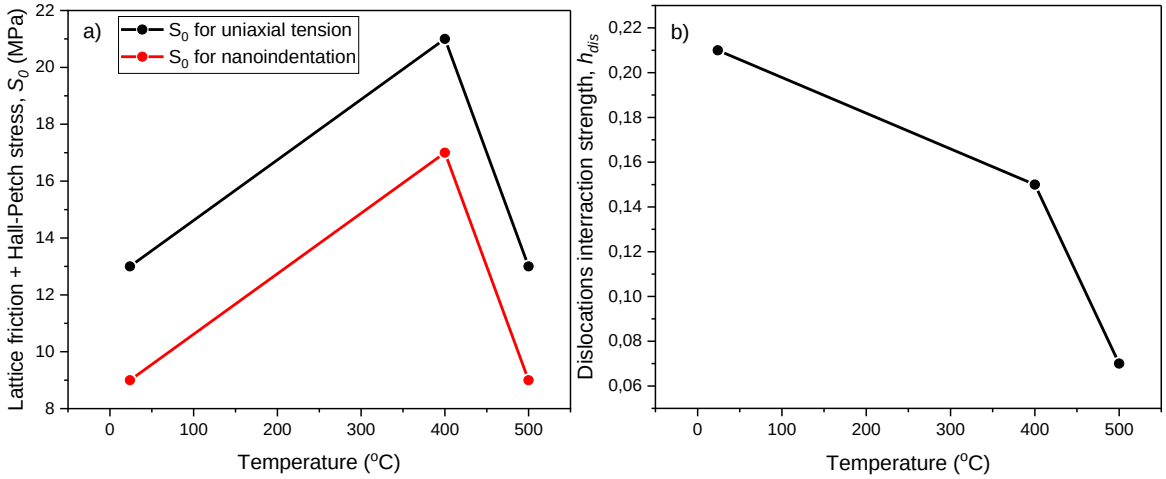

Figure 36. a) Lattice friction + Hall-Petch stress S_0 and b) dislocation-dislocation interaction strength h_{dis} versus temperature.

As already mentioned, the carbon interstitials seem to still contribute to the stress needed to start the dislocation movement at 400°C, so this fact was taken into account by increasing the S_0 value from 13 to 21 MPa (Figure 36(a)) for this temperature to simulate the uniaxial tension, and from 9 to 17 MPa (subtracting 4 MPa of the Hall-Petch effect) for the nanoindentation simulation, while the room temperature and 500°C values are equal to each other. It must be added that within the used crystal plasticity framework the S_0 remains constant (apart from its modification at 400°C to account for the carbon presence), despite the known inverse dependence of the friction stress/Hall-Petch effect of temperature. This is because the thermal stress $\hat{\tau}$ value from the formulation (2.13) is responsible for the thermal effects in the applied model. However, the dislocation-dislocation interaction coefficient requires additional variation with temperature to adequately capture the hardening rates. Thus, it decreases with temperature (see Figure 36(b)), which is the expected trend for BCC metals [80].

The constitutive parameters presented in Table 5 are correspondingly used to perform the uniaxial tension simulations in the standalone mode (one material point) applied to a polycrystalline sample consisting of 1000 grains until 15% of true strain (known dislocation density value). The computational cell is stretched in the direction *x* at a given temperature and strain rate and is free to deform along the directions *y* and *z*. The $(\sigma - \varepsilon)$ curves obtained from those simulations carried at RT, 400°C and 500°C are presented in Figure 37(a). To demonstrate the quality of the obtained match, the ratio of the simulated curve to the experimental one was expressed in percent and plotted versus true strain starting from ε_{true} = 0.2% in Figure 37(b). As can be seen, the maximum difference between the pair of experimental and simulated curves at room temperature remains within 2%, reaches 5% for 400°C, and does not exceed 7% at 500°C. Yield stress values agree with experimental data within 2% of divergence.

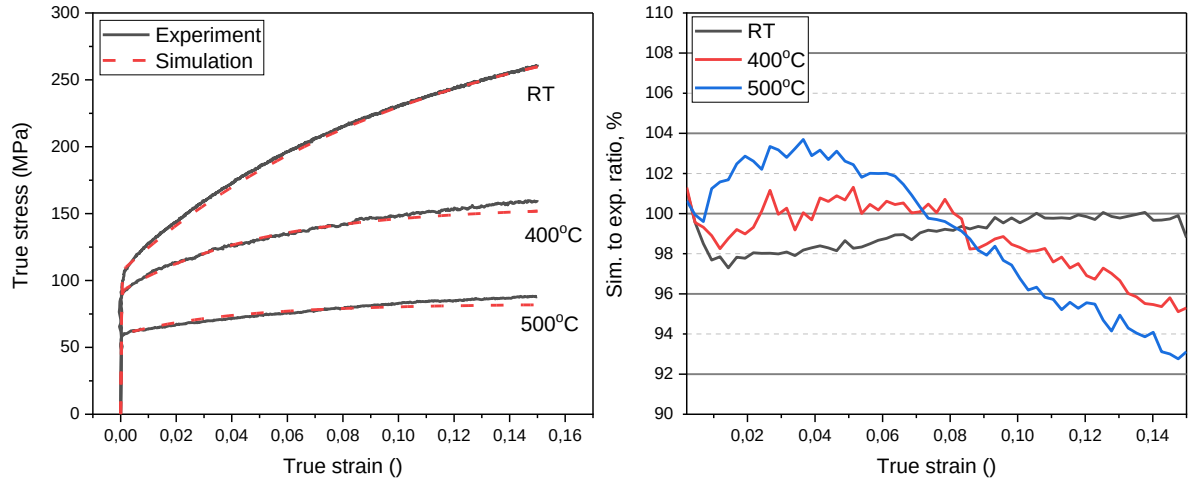

Figure 37. a) Simulated (dashed red) and experimental (solid black) true stress-strain curves of iron in comparison, b) simulation to experimental σ-ε curves ratios in percent.

As the CPFEM simulations were performed, the dislocation density as a function of the strain attained was reported; see Figure 38. As one can see, the development of the dislocation density is found to be in good agreement with the TEM measurements made at the elongation corresponding to 15% of strain at room temperature ($2 \cdot 10^{14}$ m^{-2}) presented in §3.3.4.

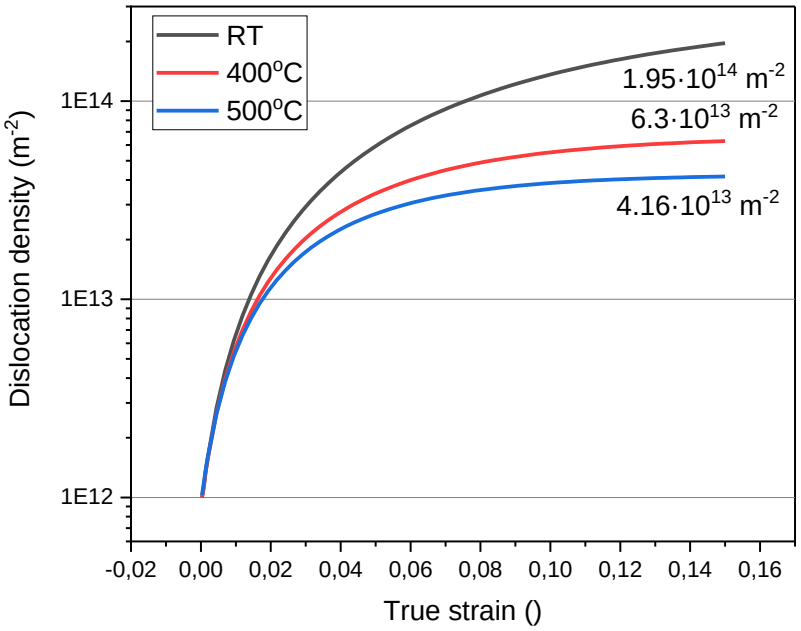

Figure 38. Dislocation density (log scale) versus true strain for the three temperatures. The numerical values presented in the graph correspond to the dislocation densities at 15% of the true strain.

To conclude, the presented reproducibility of the experimental results using the standalone crystal plasticity approach approves its applicability on this scale and in this deformation mode. Therefore, the transfer of the obtained constitutive parameters into the CPFEM nanoindentation setup is meaningful and will be performed as the next step.

3.4.2 Nanoindentation simulations

3.4.2.1 FEM setup

The FEM setup used for the simulations of the nanoindentation process is presented in Figure 39. It is a 100 × 100 × 50 μm^3 single crystal specimen box (the adequacy of considering a single crystal instead of a texture is discussed and evidenced in Appendix 1). The bottom plane of the box was constrained by the *x*, *y*, and *z* axes, and the side planes were constrained only along their normal axis to avoid an expansion of the box if dimensions are too small for a particular indentation depth. The Berkovich indenter is perfect, rigid, frictionless, has a 12.95° attack angle, and its displacement is controlled according to the experimentally obtained maximum depth.

The mesh was refined next to the tip with the smallest characteristic length of the element of 0.125 μm. Overall it had 7725 nodes and 36682 tetrahedral 1st-order elements in which locking is avoided by averaging volumetric deformation. The established FEM model is provided in Figure 39. Single crystal orientations were established for immersion of the indenter successively in the [100], [101] and [111] directions as the three ultimate cases of surface orientations. However, as will be shown further, the outgoing CPFEM nanoindentation force-displacement curves slightly change depending on the crystal orientation (~3.5% as the most), so such a choice of directions is a tool to study the corresponding stress-strain fields created by the indenter tip.

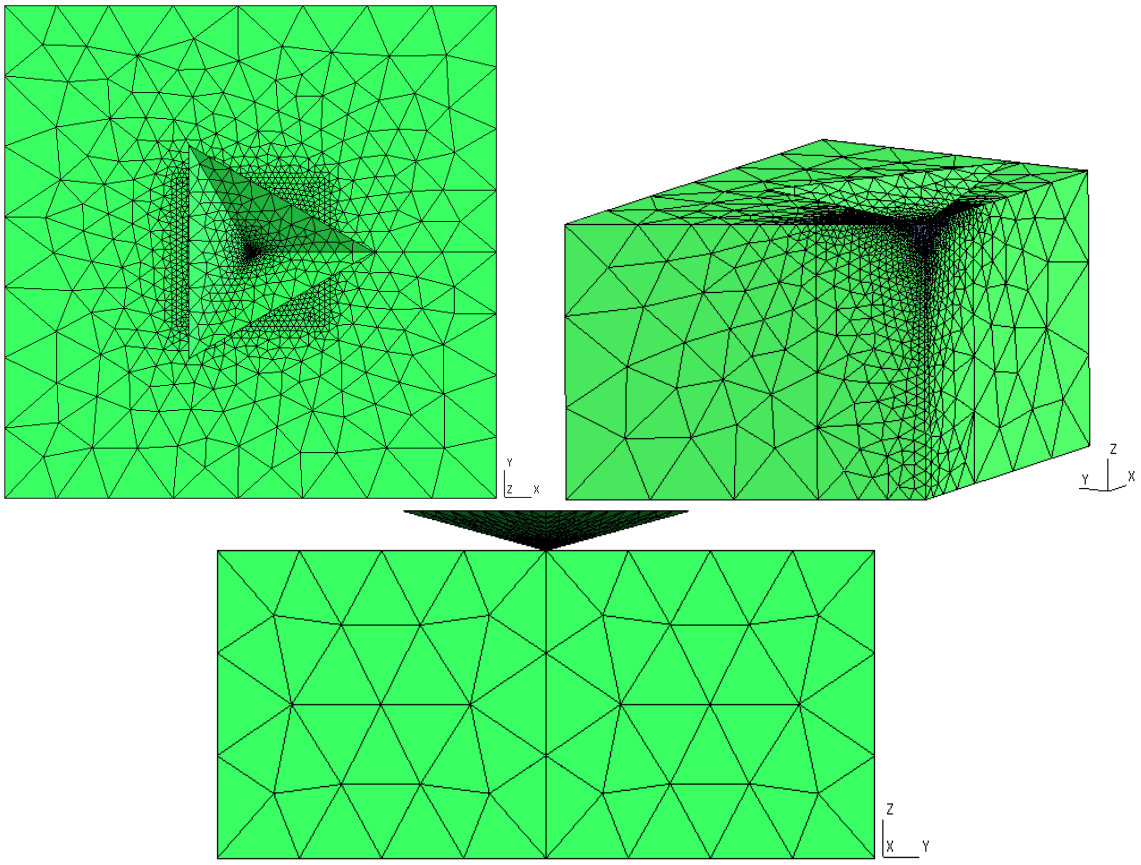

Figure 39. FEM setup used for the simulations of the nanoindentation process in pure iron.

Mesh sensitivity analysis was performed to ensure the absence of its effect on the mechanical response. The assumed characteristic length of the element below the indenter tip was divided by a factor of two for two times, and the simulation was recalculated with each mesh. Then, these three outputs were compared and presented in the plot in Figure 40.

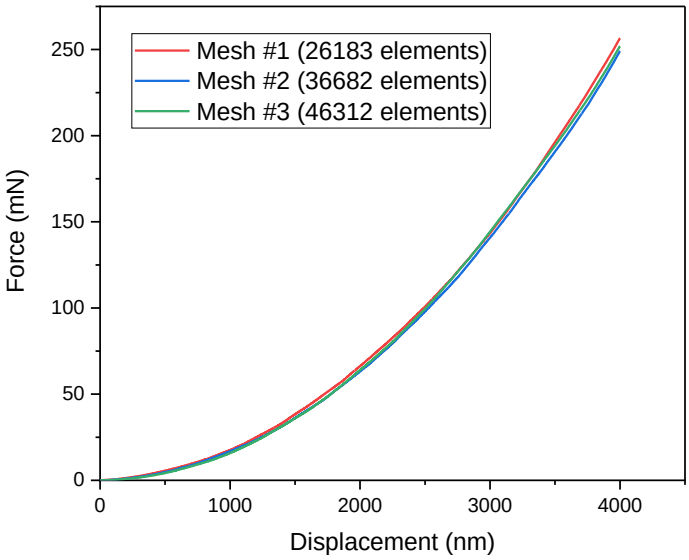

Figure 40. Mesh convergence analysis of the nanoindentation FEM setup.

As can be seen in Figure 40, the mesh dependence of the model is almost negligible for every size of the mesh. The difference between the outputs obtained from Mesh #1 and Mesh #2 at full depth is approx. 3%, and between Mesh #2 and Mesh #3 is 1%, so to obtain a balance between the accuracy and calculation time, Mesh #2 was used in the presented work.

The reason for using the perfect frictionless indenter has been driven by the simplicity of the model. Studies show a negligible difference from the introduction of the friction coefficient when modeling the Berkovich indenter [97] [98]. However, the issue with the indenter tip sharpness is trickier, as a less sharp indenter requires more force to penetrate the material, and thus the measured hardness is higher. This was demonstrated in Refs. [98] [99] on silica and on shallow depths. According to the studies provided, the difference in the output force between a sharp tip (0 nm radius) and a blunt tip (200 nm radius) can reach up to ~30-40% at depths lower than 200 nm. The tip radii used in this work are lower than that, nevertheless, the difference might still be significant. However, the effect of tip roundness fades as the penetration depth increases. In Ref. [100] authors demonstrate on MgO that the effect of tip radius is especially big between 50 and 133 nm and strives to unsignificant values afterward.

In addition, the computational setup applied in the presented work was not robust enough to converge the simulations of the unloading part of the nanoindentation curve. Eventually, the unloading was not simulated in a meaningful manner, therefore, this part is not presented throughout the whole manuscript for the simulated curves. As it is an important section for the Oliver-Pharr analysis to account for the tip imperfections and derive the contact area function, the method must be reconsidered in order to establish a hardness formulation for the simulations case. It will be based on several simplifications:

1. The use of a perfect indenter allows one to simplify the contact area equation (2.4) to just one term: $A = 24.56 \cdot h_c^2$ (as the fitting of the area function to the roundness of the tip is no longer needed).

2. The experimental data show that the difference between the contact and maximum depths is usually low in the case of iron or steel (1-5%). Therefore, the substitution of the contact depth h_c with the maximum depth h_{max} in the equation (2.4) for these materials is a justified assumption.

Eventually, these simplifications allow one to introduce a simplified hardness formula to be used in the simulations:

$$H = \frac{F}{24.56 \cdot h_{max}^2} \tag{3.2}$$

where F is the force obtained from the force-displacement curve.

This simplified hardness, compared to the experimental Oliver-Pharr hardness from the Eq. (2.7), can be underestimated on up to 10% due to the quadratic form of the depth value.

Ideally, FEM simulations of the nanoindentation process should include the roundness of the indenter; however, the presented research features the absence of the unloading part, avoided complication of the geometrical setup, and reduced computational time, while dealing with penetration depths higher than 500 nm. All these facts bring a justification for the utilization of the perfect indenter.

3.4.2.2 Simulations

Applying the described in §3.4.2.1 FEM setup and the constitutive law from §3.4.1, the nanoindentation tests were simulated at RT, 400°C, and 500°C. The resulting force-displacement curves were obtained with respect to the three crystal orientations and then averaged to provide a comparison with the experimental ones, as presented in Figure 41. Figure 41(d) contains the separated force-displacement curves for each of the three orientations. It is clearly seen that in the case of immersion of the indenter in the [100] direction, the material shows a slightly lower resistance to deformation (~3.5% difference between [100] and [111] at RT).

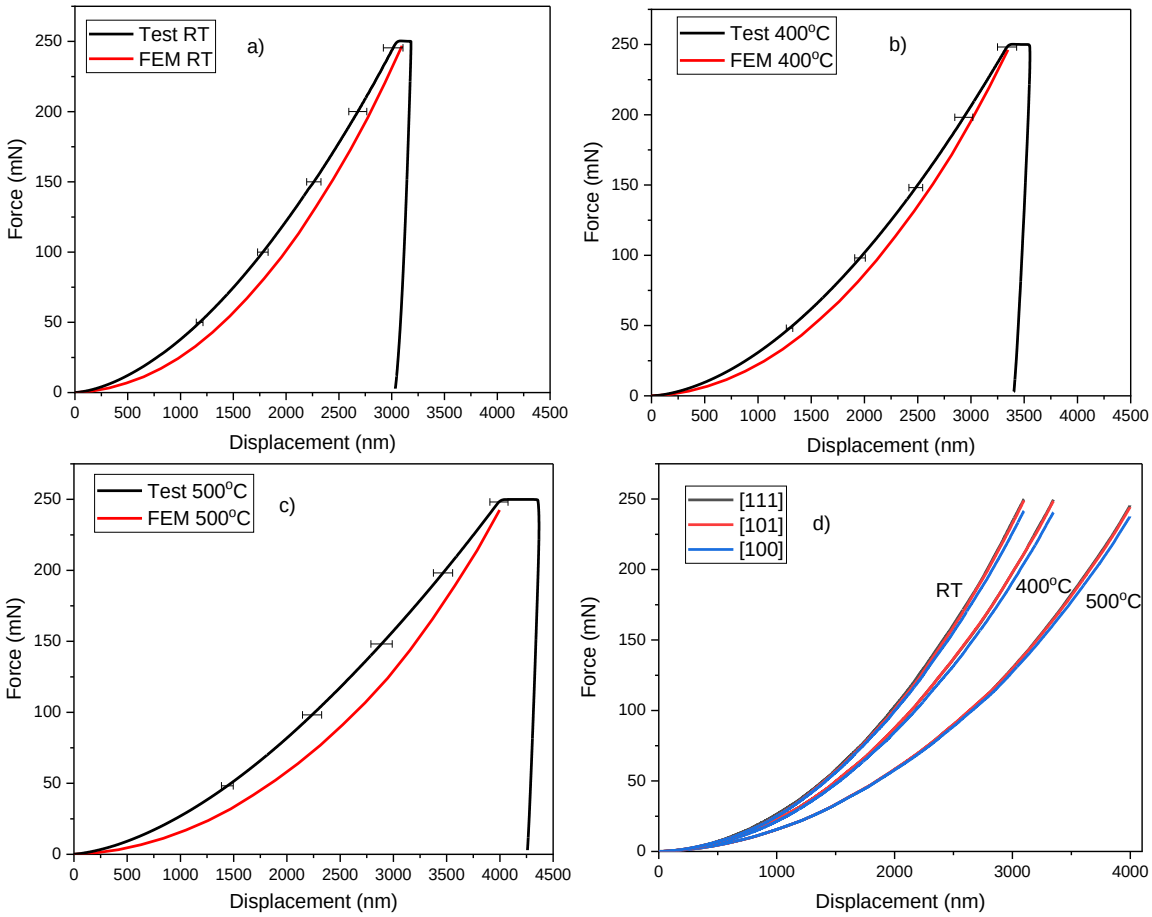

Figure 41. Averaged nanoindentation force-displacement curves obtained from experiment (black) and FEA (red) in comparison: a) at room temperature, b) 400°C, c) 500°C; d) Single curves by grain orientation.

Figure 41(a, b, c) shows that the output force at h_{max} match well with the experimental data; however, the CPFEM curves are strongly underestimating the experimental ones on the shallow depths (up to 60% difference at 250-500 nm) which might consequently affect the further force evolution. To improve this, the strain gradient theory must be implemented into the CPFEM setup, which, however, implies a cumbersome and dedicated implementation and computational effort.

Moreover, as has been said, the perfect indenter may bring some underestimation of the force output on the lower depths. Other reasons for the observed difference between the curves can come from the experimental artifacts, such as limited surface roughness, machine compliances, thermal drifts, uncertainties on the low depths, etc.

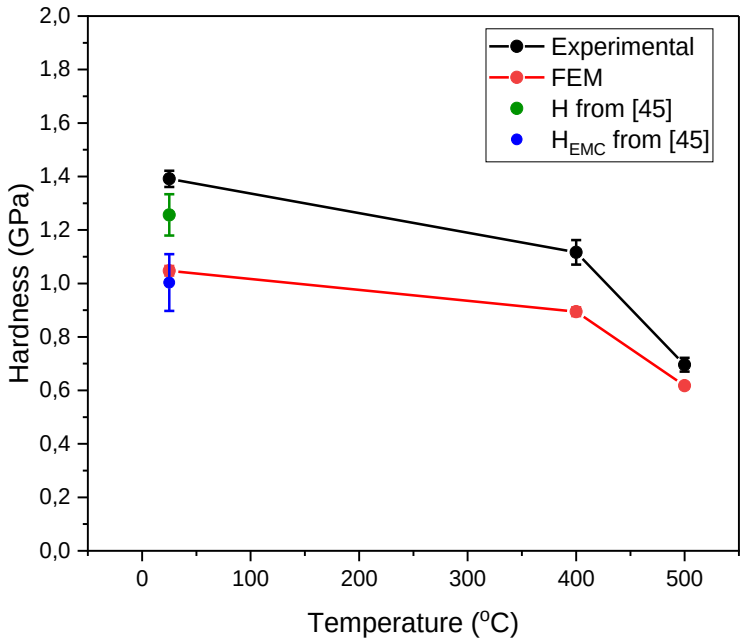

Figure 42. Hardness values calculated from experiment (black), FEM (red) and taken from [45] (blue, green) in comparison.

Given the simulated load-displacement curves, the hardness has been calculated using FEM data and compared to the experimentally measured values; see Figure 42. It can be seen that the hardness values from FEM coincide well with the hardness values of the same material taken from [45] where the elastic modulus correction procedure was applied (Eq. (2.9)). This is a good sign, as both the FEM hardness values (calculated with (3.2)) and EMC processed do not account for the distortions from the indentation pile-ups. As is known, they can affect hardness calculations and are significantly large in this material (see Figure 27). In support of this statement, one can see how the difference between CPFEM and experimental hardness values decreases with temperature, and, as we know, the pile-up volume decreases as well. The difference between the values of both investigations must also come from the high difference in indentation strain rates: 3.33 mN/s (green dot) and 50 mN/s (black dot). Unfortunately, Ref. [45] provides only data at room temperature.

Eventually, one can see that the general trend for the hardness predicted by the simulations is correctly reproduced, but the absolute value is underestimated by the CPFEM. This underestimation may be explained at least partially by the need to apply the EMC procedure to the experimental data.

3.4.3 Analysis of the FEM maps

The extension of the plastic deformation zone was also inspected by outputting the 2D profiles of the dislocation density underneath the indenter tip, in a similar way as it was experimentally studied by FIB-TEM. These profiles are presented in Figure 43. Here and in the following FEM pictures the *x*, *y* and *z* axes correspond to the illustration in Figure 39.

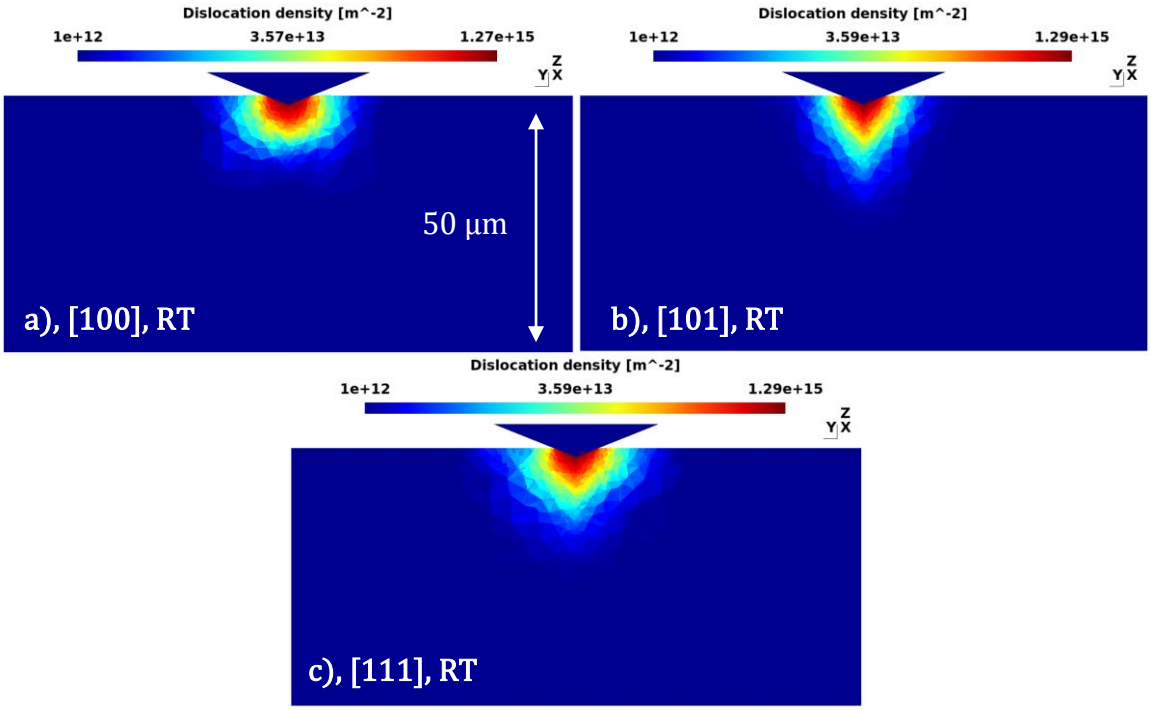

Figure 43. Dislocation density (log scale) at h = 1.5 µm and room temperature from FEA: a) [100] surface orientation, b) [101], c) [111].

No significant change in the dislocation density evolution pattern related to test temperature was found, so only the results obtained at room temperature are shown. However, the patterns in Figure 43 are considerably dependent on the crystal orientation of the indented surface and the perspective view. Thereby, the dislocation density pattern evenly surrounds the indenter tip in a hemisphere-shaped form in the case of the [100] surface orientation, as in Figure 43(a), while in the case of the [101] orientation, the plastic deformation extends into the bulk of the material, as in Figure 43(b). If the crystal surface orientation is [111], the dislocation density pattern appears to be a combination of the two other cases, experiencing the spherical distribution as in [100], but still having a noticeable "peak" along the indentation direction, as shown in Figure 43(c).

By picking the absolute values of the dislocation density, it is observed that the density increase predicted by the CPFEM simulations agrees well with the lamella TEM measurements presented in §3.3.3 (reaching ~$1 \cdot 10^{15}$ m^{-2} in the TEM observation and to ~$1.3 \cdot 10^{15}$ m^{-2} in CPFEM). Of course, the maximum dislocation density value is one of the constitutive parameters, which gives us control on the dislocation density behavior, but the fact that it actually reaches this value and that it was obtained from the fitting to uniaxial tension tests points to a good interconnection between the crystal plasticity model and the real material behavior under both compressive and tensile deformations.

In Figure 44 the maximum shear stress profiles are provided. The maximum shear stress is calculated as the half-difference between the maximum and minimum principal stresses σ_1 and σ_3 obtained from the Cauchy stress tensor $\boldsymbol{\sigma}$.

$$\tau_{max} = \frac{1}{2}(\sigma_1 - \sigma_3) \tag{3.3}$$

Just as for the dislocation density patterns, the shear stress distribution profile does not change with the test temperature, but the overall stress level decreases from the highest value of 424 MPa at room temperature down to 158 MPa at 500°C, what can be seen in Figure 44(c, d, e). However, the direction of the stress distribution changes with the orientation of the crystal as shown in Figure 44(a, b, c). Figure 44(a) shows that, in the case of orientation [101], the stress propagates along the *z* axis, as it occurs with the evolution of the dislocation density, while its highest values accumulate below the indenter. If indentation is performed in the [100] orientation, as in Figure 44(c), stress behavior becomes the opposite: the highest and lowest stress concentrations are "mirrored" with respect to the [101] orientation. This happens because [101] is achieved by rotating the crystal lattice in the [100] position by 45°, so the active slip systems also co-rotate. The [111] orientation leads to an asymmetric stress pattern if viewed from the same angle as shown in Figure 44(b). Stress propagates inside the bulk, which is expected behavior due to the fact that the indenter is being immersed along the [111] slip direction in BCC metals. The symmetry of the stress distribution indeed could be obtained by different in-plane surface orientation relative to the indenter; however, performing such a dedicated configuration was not in the scope of our work, which primary focuses on the treatment of the experimental data, where the orientation of grains to indented axis is usually random.

It is important to emphasize that in the case of the [100] surface orientation, the highest stress is not concentrated right below the indenter tip, as in the case of the other two directions. In addition, overall it has lower values, as can be seen by the comparison of the color maps in Figure 44(a, b, c). This must be also related to the fact that the force-displacement curve for [100] surface orientation is always lower than the others, which can be seen in Figure 41(d).

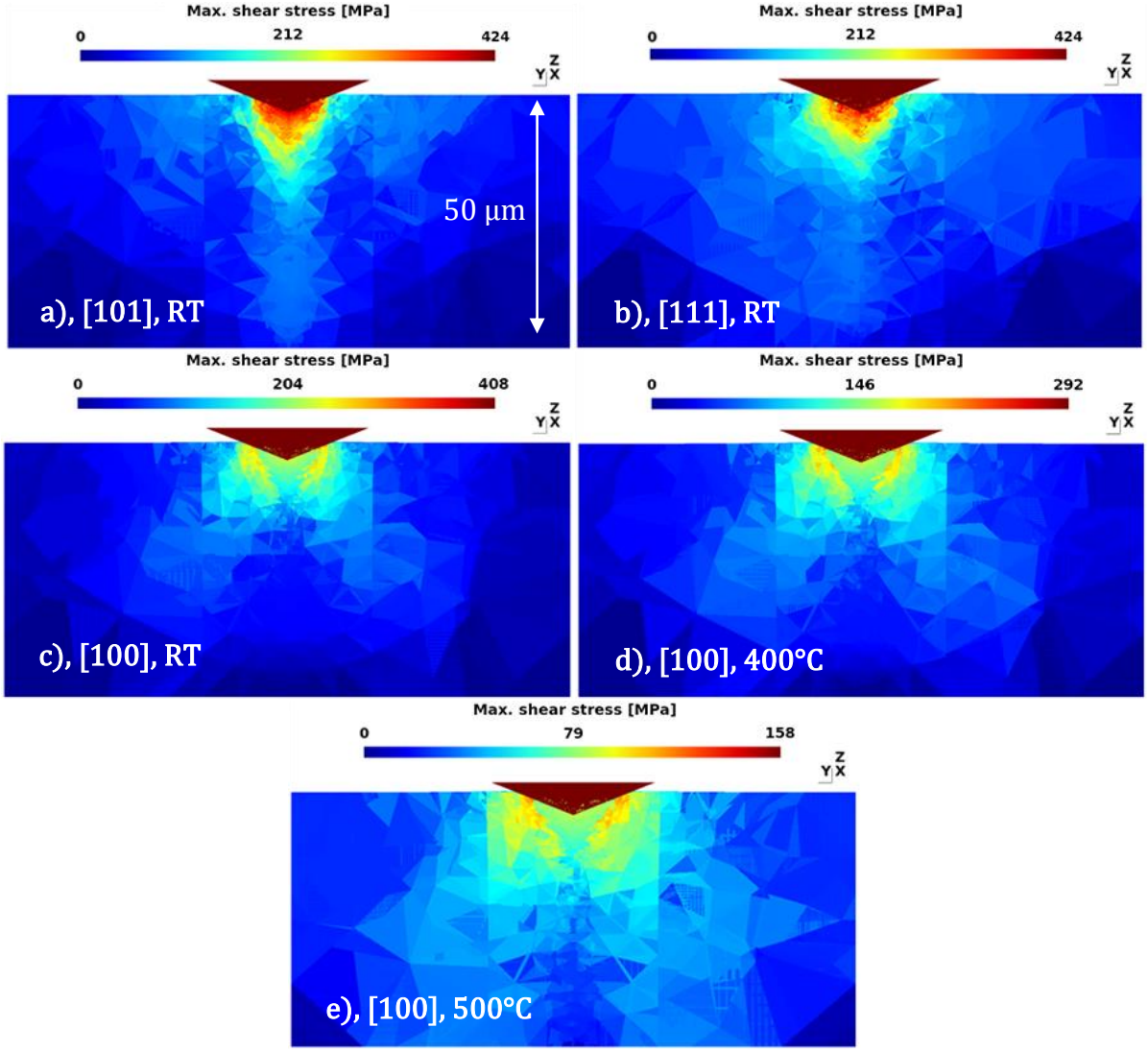

Figure 44. Maximum shear stress at h_{max} for different surface orientations from FEA: a-c) room temperature; d) 400°C; e) 500°C.

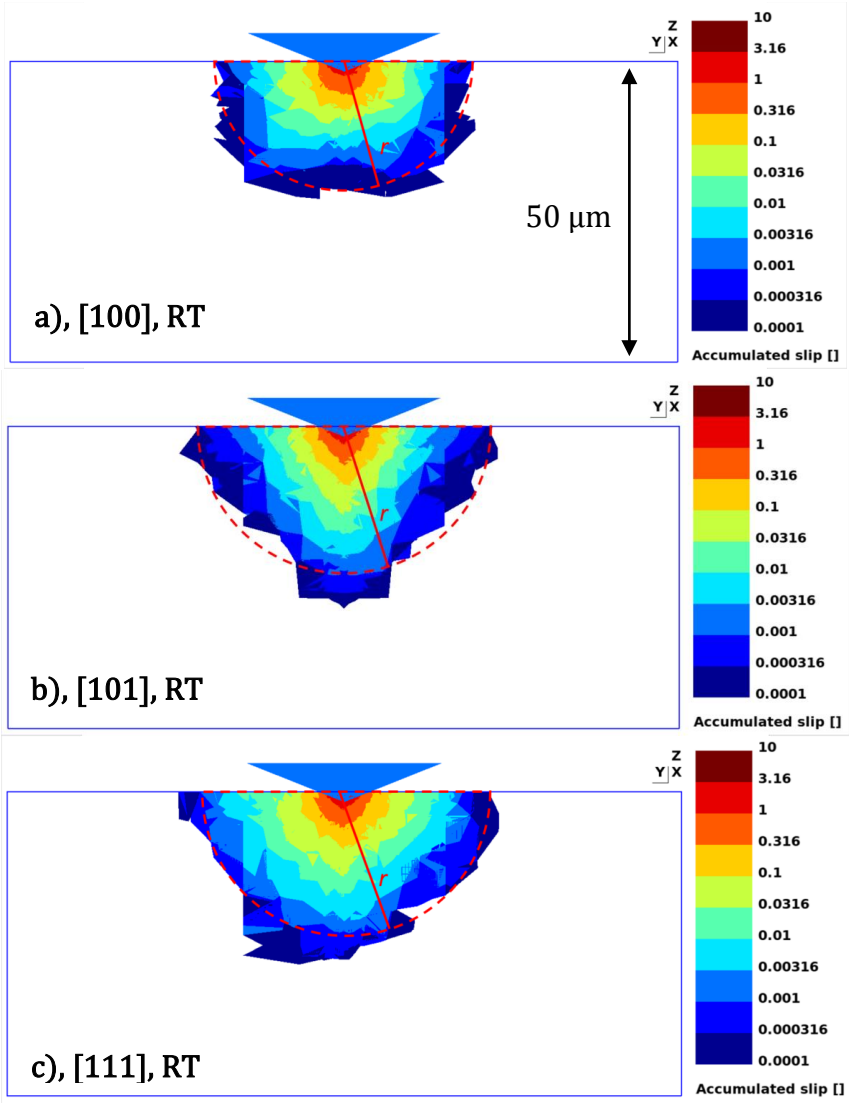

Figure 45. Accumulated slip (log scale) at h = 1.5 µm and room temperature from FEA: a) [100] surface orientation b) [101], c) [111].

Another common practice to explore the range of the plastic zone extension is to output the quantities responsible for the plastic deformation. In our case, it is the accumulated slip distribution. In Figure 45 the elements which undergo at least 0.01% deformation as accumulated slip are presented (lower values do not further extend the plastic zone further) are presented, which gives us an idea of the plastic deformation region. The radii of the obtained hemispheres with respect to the orientations were measured and their ratios to the penetration depth of h = 1.5 µm were calculated and averaged as 13.82 ± 0.8. The radii of the hemispheres with respect to temperature were also measured; however, no significant differences were found in this case and the factor divergence for the [100] orientation was calculated as 2.5%. These facts allow us to conclude that the penetration depth to the plastic zone radius is constant for the studied material in this temperature range and depends only on the crystal orientation.

Previously, SEM and TEM inspection of the lamella obtained with FIB have been discussed, where the ratio of h/r (see Figure 32(b))) was found to be ~5, and the formation of the dislocation bands indicated that this value must be higher. However, the deformation was estimated by analyzing the contrast fields obtained from different electron reactions and the

particular dislocation behavior. In the case of modeling, it is possible to distinguish the elements experienced plastic deformation; therefore, more accurately estimate the plastic zone as well as accumulated slip gradients associated with the changes of the contrast otherwise seen by the SEM tool. To demonstrate this approach, the TEM micrograph and the FEM accumulated slip color map are superimposed as shown in Figure 46.

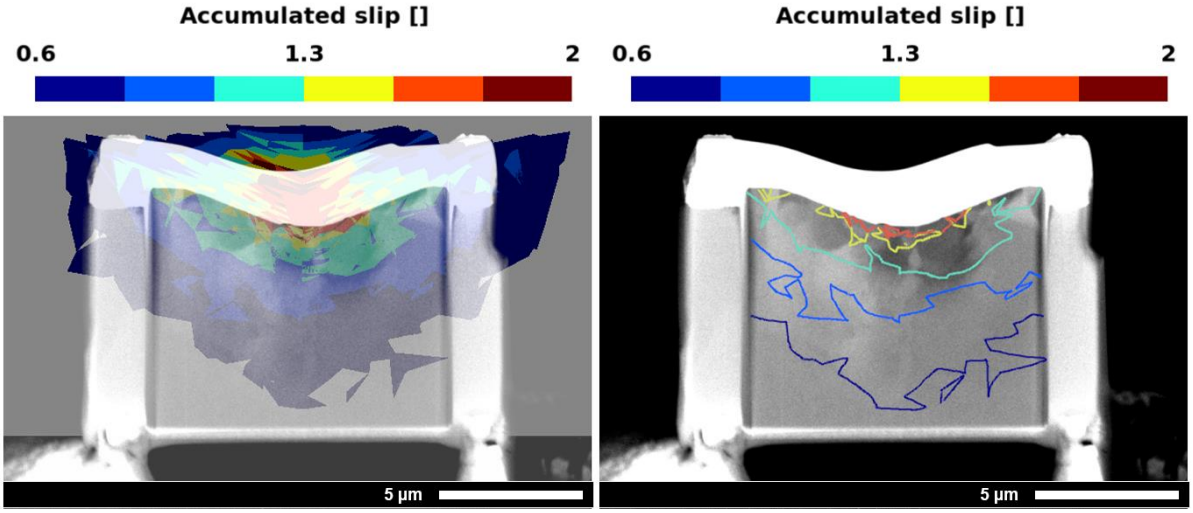

Figure 46. Plastic zones from FEA at RT and TEM compared by overlapping.

The legend in Figure 46 is adjusted in a way that matches the degree of deformation occurred in the area of the lamella. One can see that the deformation values of 60% and higher precisely represent the contour of the SEM dark-light contrast in the lamella. The area of the lamella where the contrast is slightly inhomogeneous is reflected by the iso-lines corresponding to 0.6 and 0.83 of deformation. Zones that experienced deeper deformation stay within 0.83 and 1.06, and the most dark gray areas are at least 1.06 deformation, with some particularly high deformed zones right next to the indenter tip of 1.3 and higher deformation values. Such an approach provides a good understanding of the degree of plastic deformation that occurred in each zone.

The next step is to compare and discuss the formation of the indentation pile-ups as observed experimentally and in CPFEM. When the orientations of the indented grains were analyzed using EBSD maps, it was possible to retrieve the Euler angles and use them to similarly orient the crystal in CPFEM simulation. Figure 47(b, d, f) contains the following information: a picture of the lattice orientation obtained with the prescribed Euler angles (top left), the top view of the final nanoindentation imprint (top right) and the 3D picture of the imprint with the colormap (bottom). The transparent plane on the lattice orientation picture corresponds to the surface planes where indents were placed. Figure 47(a, c, e) shows the real indents taken by SEM.

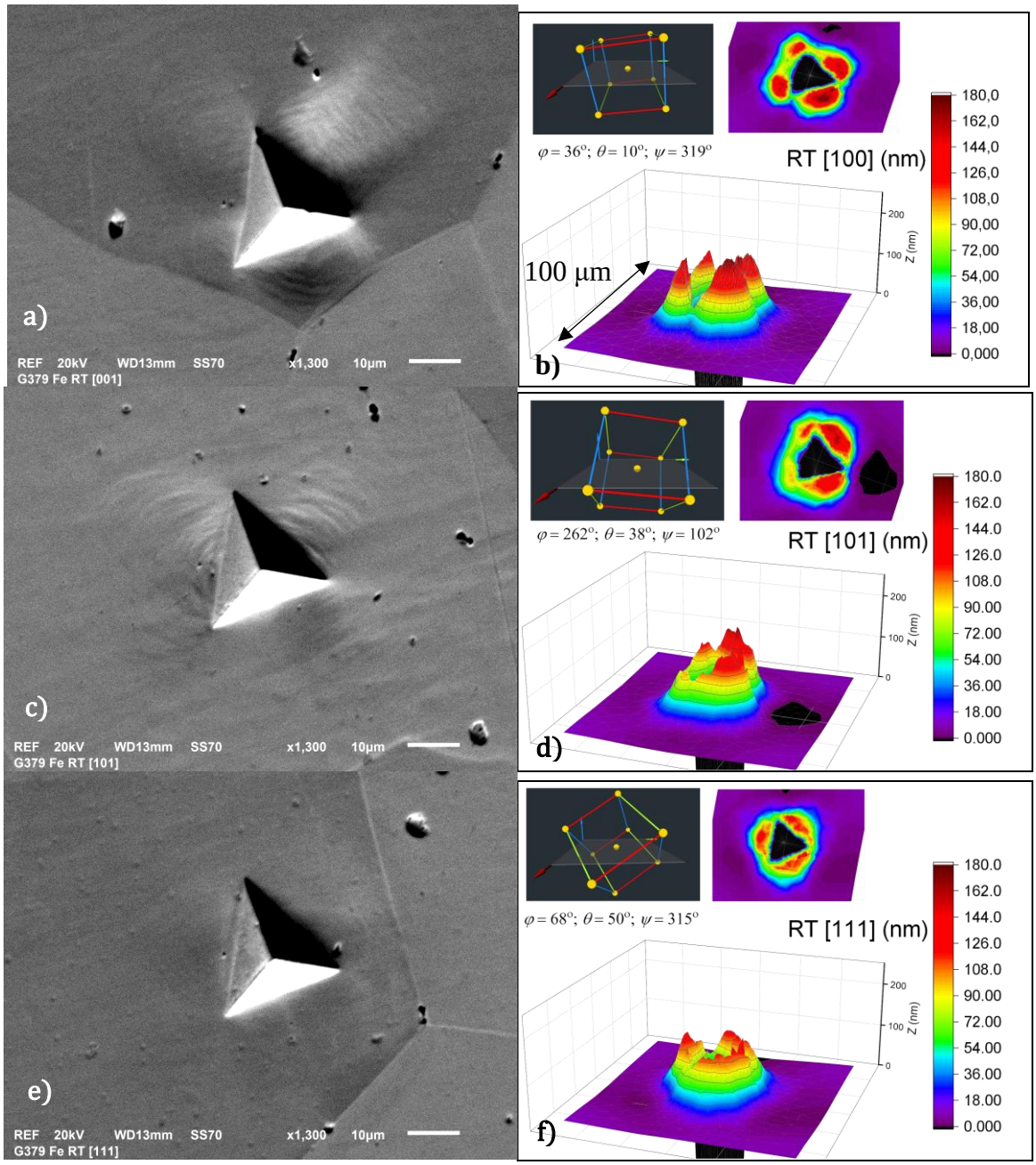

Figure 47. The final imprint and indentation pile-ups shapes taken from SEM and FEM.

It can be seen that the indents placed on the [100] and [101] surface orientations have two pile-ups, each created by one of the two sides of the Berkovich indenter and two adjacent ones, both created by another side. In the case of the CPFEM simulation, it seems that both indents have properly caught the pile-up behavior, but in the case of [101], it is a topic of discussion if the relative height of each pile-up was correctly reproduced. The pile-ups in [111] surface orientation are hard to distinguish, but CPFEM seems to correctly reproduce this: the overall pile-ups height is noticeably lower than in the other cases and very similar to each other.

Apparently, SEM is not a proper tool to precisely analyze the indentation pile-ups shape and size, instead, the atomic force microscope should be used. However, the CPFEM model definitely overestimates the eventual pile-up height due to the lack of strain gradient model and tip roundness. Therefore, their shapes and relative heights are compared and analyzed, without

making judgements about the absolute ones. For these purposes, SEM appears to be a sufficient tool.

3.5 Summary & conclusions

In this section, summarized and generalized conclusions from the presented chapter are given. Findings are separated into two categories corresponding to physical and technical/methodological conclusions. The former represents the outcomes related to understanding the nature of the physical processes and systems considered. The latter is related to the knowledge obtained with regard to the methodological aspects, which will be helpful in further improvements or application of the described approach in future works. Conclusions 1, 4, 5, 6, 9 from §3.5.1 and §3.5.2 are related to the nanoindentation tests used to validate the model. Conclusions 2, 3, 4, 5, 7, 8, 9 are about the CPFEM model of the nanoindentation process. Conclusions 1, 2 cover the findings related to the tensile tests used for model calibration.

3.5.1 Physical conclusions

1. The α-iron product used in this study exhibits a dynamic strain aging effect in the intermediate temperature range of interest (100°C – 300°C). This effect is observed in both types of deformations studied, tensile and nanoindentation. In the case of tensile deformation, the stress-strain curves show an increase in yield stress and hardening rate, sometimes serrated yielding. In the case of nanoindentation at these temperatures, one can observe an increase of the hardness values, suppression of creep rate, and staircase loading. To the best of our knowledge, this is the first time that nanoidentification could catch the dynamic strain aging in iron. The appearance of the dynamic strain aging makes the adoption of the material law at these temperatures meaningless (within the scope of this study), however still possible. Nevertheless, the temperature range studied reaches 500°C, where the classical dislocation-mediated thermally controlled plastic behavior returns, thus making this material appropriate for computational study.

2. Based on literature information, experimental tensile tests measurements, and fitting, the constitutive parameters obtained are in good correlation with the underlying physical processes and observations. The dislocation-dislocation interaction factor is the only parameter that changes with temperature (besides the artificial increase of S_0 parameter responsible for a set of hardening mechanisms at 400°C to account for the remaining contribution of the carbon interstitials to flow stress), and this behavior is in agreement with the literature. The activation energy must also be increased to account for the dislocation-carbon interactions as well, which is physically justified, since carbon is known to exhibit an attractive interaction with dislocations in bcc Fe.

3. Based on the analysis and best fit of the model to the experimental data, it is concluded that the contribution to the plastic flow yield coming from grain boundaries is very small (compared to lattice friction and dislocation forest). To account for the negligible impact of the Hall-Petch effect in the case of nanoindentation simulations, S_0 value responsible for a set of hardening mechanisms including Hall-Petch must be lowered by 4 MPa.

4. Correct computational reproduction of the nanoindentation experimental behavior provides an extended analysis of the complementary features, such as stress, dislocation density, and deformation distributions with respect to the crystallographic orientations. Thus, it was found that the magnitudes of the dislocation density reached under the indenter tip correlate well with the measurements performed with TEM in the same region; shear stress levels, associated with the accumulation of plastic slip, are decreasing from the highest value of ~424 MPa at room temperature to ~158 MPa at 500°C, which is consistent with the fact that elevated temperature assists stress dissipation by plastic deformation; Extensions of the plastic zone (defined as > 0.01% of slip deformation) are higher than the values predicted by literature (~13.8 versus 5-10), however the latter are usually calculated using isotropic models or contact mechanics, and cannot account for crystallographic dislocation slip.

5. The presented approach to superimpose the deformed subsurface inspected using SEM on FIB-made samples with the elements which have undergone a certain level of deformation has demonstrated its visibility and good correspondence between experiment and model prediction. The area of the lamella where the contrast is slightly inhomogeneous is reflected by the iso-lines corresponding to 0.6 and 0.83 of strain deformation. Zones that experienced deeper deformation stay within 0.83 and 1.06, and the most dark gray areas have at least 1.06 of deformation, with some particularly high deformed zones right next to the indenter tip of 1.3 and higher deformation values. Such an approach provides a good understanding of the degree of localized plastic deformation that occurred in various zones around the indenter tip.

3.5.2 Technical/Methodological conclusions

6. The application of a 20 nm SiO_2 protection layer on Fe has shown an improbable performance in high temperature nanoindentation tests. To the best of our knowledge, this is the first time that such a method was applied for the high temperature nanoindentation of highly oxidizing metals.

7. The frictionless, perfect indenter used in this study does not fully reflect the reality of the nanoindentation process; however, the performance of such an indenter is not strongly affecting the measurement of hardness, especially at high depths. Moreover, the simplicity provided by using the rigid indenter can justify the observed and expected distortions.

8. The nanoindentation force-displacement curves derived using FEM are in good agreement with the experimental ones. The force response is underestimated at depths lower than 500 nm due to the absence of strain gradient plasticity in the applied model and/or due to indenter roundness; however, the deviation reduces at larger depths. The FEM hardness values (calculated using the simplified way) correlate well with the experimental ones, which have undergone elastic modulus correction and, therefore, the removal of inaccuracies coming from indentation pile-ups. Furthermore, dislocation density maps and final imprint shapes also match well with the observations done experimentally. All these findings confirm the reasonable performance of the applied approach. The former definitely may serve

as an established basis for further improvement, such as the complex microstructure of the F/M steel and the introduction of the irradiated effect.

9. The CPFEM nanoindentation simulations have shown good predictability of the behavior of nanoindentation pile-ups shapes. SEM observations of the indentation imprint shapes have shown the reduction of the pile-ups volume with temperature, which is explained by thermally activated creep relaxation.

Chapter 4. Development & experimental validation of the CPFEM model for the nanoindentation process in reference and irradiated Eurofer97

In this chapter, the computational and experimental methodology developed in Chapter 3 will be extended to account for irradiation and will be applied to the reference and ion-irradiated Eurofer97 steel. The establishment of the model in the case of reference material will consist of the previously described steps; however, some novelty in simulation of the irradiation effect will be introduced. As has been said, in this work the approach of predicting the effect of neutron damage on macroscale material behavior using nanoindentation tests on ion-irradiated samples will be established in the opposite direction.

In the case of this research, the "layering" of the subsurface will be performed (see Figure 11). Then the features of the constitutive relation of the model will be used to empirically reproduce the mechanical properties of Eurofer97 steel after neutron irradiation. The modified material laws obtained will be transferred to simulations of the nanoindentation process in ion-irradiated material. Eventually, the association of two important physical phenomena will be evaluated: neutron and ion damage effects, as well as nano-compressive and macro-tensile deformations.

The data have been obtained in collaboration with other research groups; the contribution of everyone is highly acknowledged by the author: Prof. Ludovic Noels – guidance in the computational part, methodology; Dr. Dmitry Terentyev – guidance in the experimental part, methodology, conceptualization; Dr. Frank Bergner – ion irradiation; Dr. Enrico Corniani – nanoindentation experiments; Dr. Peter Hähner – guidance in the experimental part; Chih-Cheng Chang – tensile testing; The author himself participated in the methodology, conceptualization, computational analysis, nanoindentation experiments, and SEM/EBSD investigations. Special thanks to the Joint Research Centre in Petten, The Netherlands, for the concept of Open Access programs, giving an opportunity to young researchers to perform their investigations using high-end equipment and collaborate with experts of a particular field.

4.1 Material production and chemical composition

Eurofer97 was produced at Böhler Edelstahl in Kapfenberg, Austria, using the standard industrial procedure consisting of hot rolling and subsequent heat treatments: austenitization at 980°C for 30 min, air cooling and tempering at 760°C for 90 min. The chemical composition of the final product complies with the requirements provided in Table 1 [101] and can be verified with Table 6. The microstructure of the material is tempered martensite with carbide inclusions [102], and the basic properties can be found in [103].

C	Si	P	S	Ni	Cr	Mo	V
0.09	0.019	0.002	0.003	0.01	8.6	0.002	0.2
Ta	**W**	**Ti**	**Cu**	**Nb**	**Al**	**B**	**Co**
0.12	1	0.001	0.005	0.001	0.0001	0.0009	0.03

Table 6. Chemical composition of Eurofer97 in wt. %.

4.2 Experimental results

4.2.1 Ion irradiation

Ion irradiation of the nanoindentation specimen was performed at the Helmholtz-Zentrum Dresden-Rossendorf (HZDR) institute located in Dresden, Germany. The irradiation campaign has been carried out as part of the M4F project [52].

Prior to irradiation, a 10 × 10 × 1 mm^3 Eurofer97 specimen had been cut. Then, one-sided grinding and mechanical polishing was used up to an active oxide polishing suspension "OP-S" according to Table 7.

	Method	Parameters
Step 1	Mechanical grinding	500 grit grinding paper
Step 2	Mechanical grinding	1000 grit grinding paper
Step 3	Mechanical grinding	2000 grit grinding paper
Step 4	Mechanical polishing	3 µm diamond suspension
Step 5	Mechanical polishing	1 µm diamond suspension
Step 6	OP-S	2 h

Table 7. Surface preparation method of Eurofer97 samples.

Eventually, an electrolytic polishing was applied at room temperature using 10% oxalic acid and 5V voltage.

For the irradiation process, Fe^{2+} ions of 5 MeV energy produced by a 3MV Tandetron accelerator were used. The ambient temperature was 300°C. The total fluence was $2.4 \cdot 10^{15}$ ions/cm^2. Calculations using the binary collision code SRIM [22] were performed to calculate the depth profiles of the displacement damage and the injected interstitial atoms.

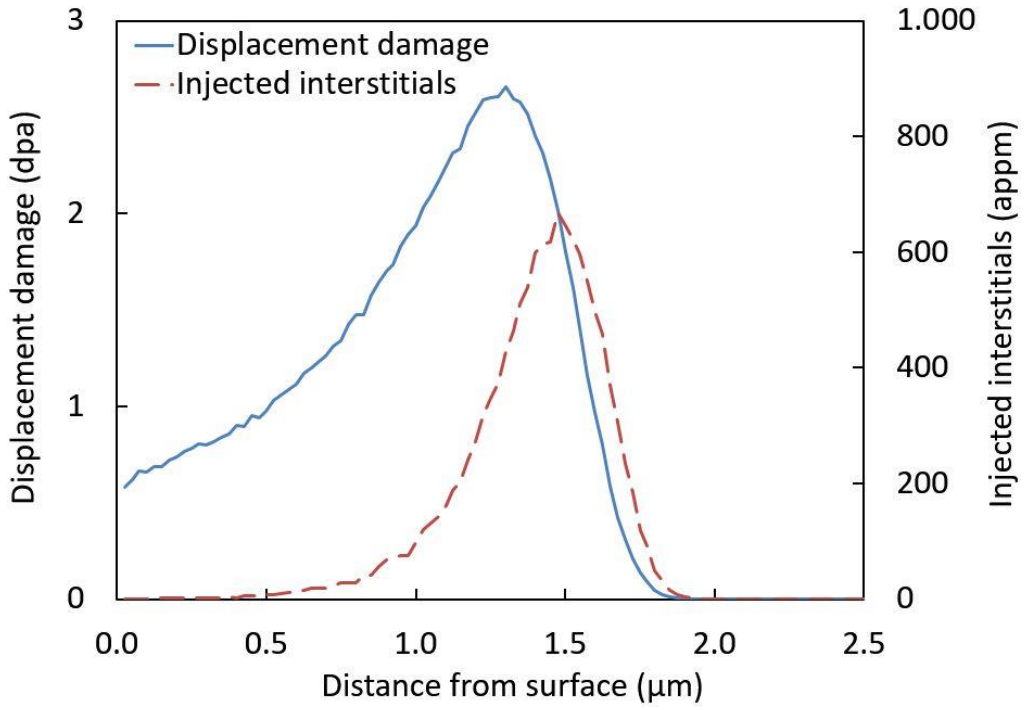

Figure 48. Damage-depth profile for the irradiated Eurofer97 specimen.

The damage-depth profile presented in Figure 48 shows an exponential increase in displacement damage from ~0.5 dpa on the surface, to the Bragg peak of around 2.6 dpa at ~1.25 µm. Then a steep reduction to the total absence of damage at ~1.8 µm takes place.

4.2.2 Tensile testing

Unlike iron specimens, it was not necessary to fabricate new specimens for Eurofer97, as the material database provided by SCK-CEN was large enough to find the required experimental data. Tensile tests were carried out on a miniaturized flat (dogbone) tensile sample with 5.2 mm gauge length and 1 mm × 1.6 mm cross-sectional area using an INSTRON model 1362 coupled with a 100 kN load cell. The tests were carried out at room temperature and 300°C with a crosshead speed of 0.087 mm/min (2.78 x 10^{-4} s^{-1} strain rate) and the tensile properties were generated according to ASTM E8/E8M [104] standard for the material studied. After the Young's modulus correction procedure (3.1) and application of the formulations (2.10), (2.11) the engineering and true stress-strain curves presented in Figure 49 were obtained. A classical thermoactivated behavior can be seen, where yield stress, hardening rate, and uniform elongation are reducing with respect to temperature.

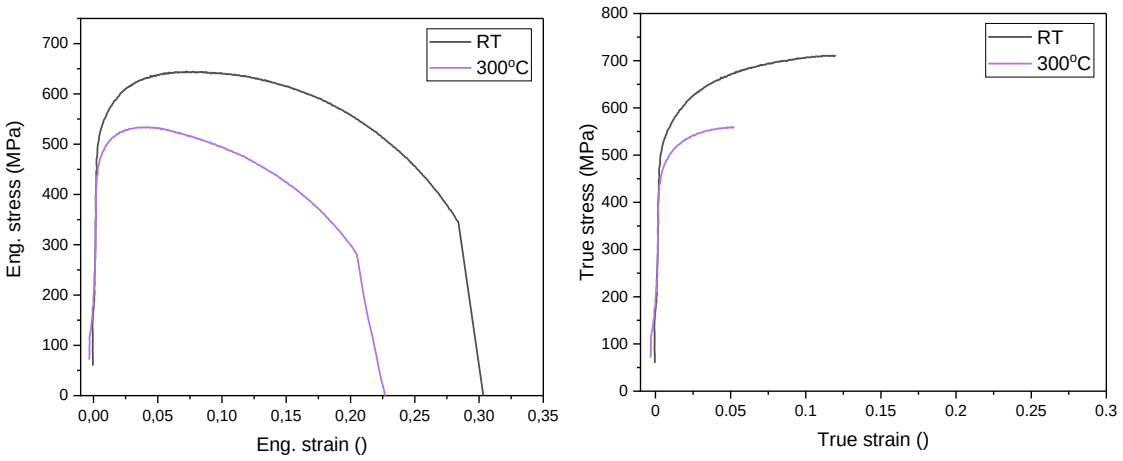

Figure 49. Engineering and true stress-strain curves of Eurofer97 at two different temperatures.

Neutron-irradiated tensile tests data are available in the literature [105]. No stress-strain curves are provided in the publication, but the yield stress dependence on the damage dose and test temperature is sufficient for the methodology used. It is important to use the data obtained at the same irradiation temperature as the ion irradiation assumed for the comparison, which is 300°C in the case of this work and [105]. The yield stress values are presented in Figure 50.

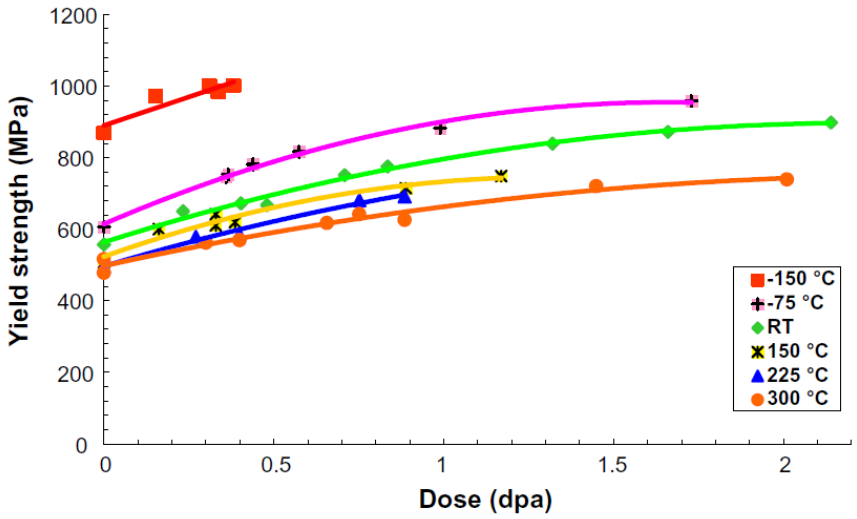

Figure 50. Yield stress values of Eurofer97 measured from tensile tests as a function of dose; Reprinted from Journal of Nuclear Materials, Volumes 329-333, Part B, Lucon E., Chaouadi R., Decréton M., Mechanical properties of the European reference RAFM steel (EUROFER97) before and after irradiation at 300°C, 1078-1082, Copyright (2004), with permission from Elsevier [106].

4.2.3 Nanoindentation

Nanoindentation experiments from this subsection have been carried out in collaboration with the Micro-Characterization Laboratory of the European Commission Joint Research Center located in Petten, The Netherlands, within the Open Access program.

The test bench used in the experimental campaign was the Anton Paar UNHT^3 Ultra nanoindentation tester. This nanoindenter provides high temperature testing up to 800°C in a high vacuum of 10^{-4} Pa to avoid sample oxidation. The testing module consists of the indenter tip, the reference ball located at a 9.3 mm distance from the indenter tip, and a ceramic heating stage with the sample holder where the specimen is located. The heating and temperature control are performed by using lightbulbs and thermocouples, an individual pair for each part, so three in total. Temperature stabilization on the sample is achieved by the reference ball placed on the surface during the indentation process to establish the minimal temperature difference between the thermocouples by automatic power control on the lightbulbs. The indentation positions and the surface of the sample can be observed with an optical microscope located next to the testing head in the vacuum chamber, and the movement of the heating stage with the specimen is done by a motorized table. The specimen is fixed by using only mechanical clamping. The pictures of the test bench are provided in Figure 51.

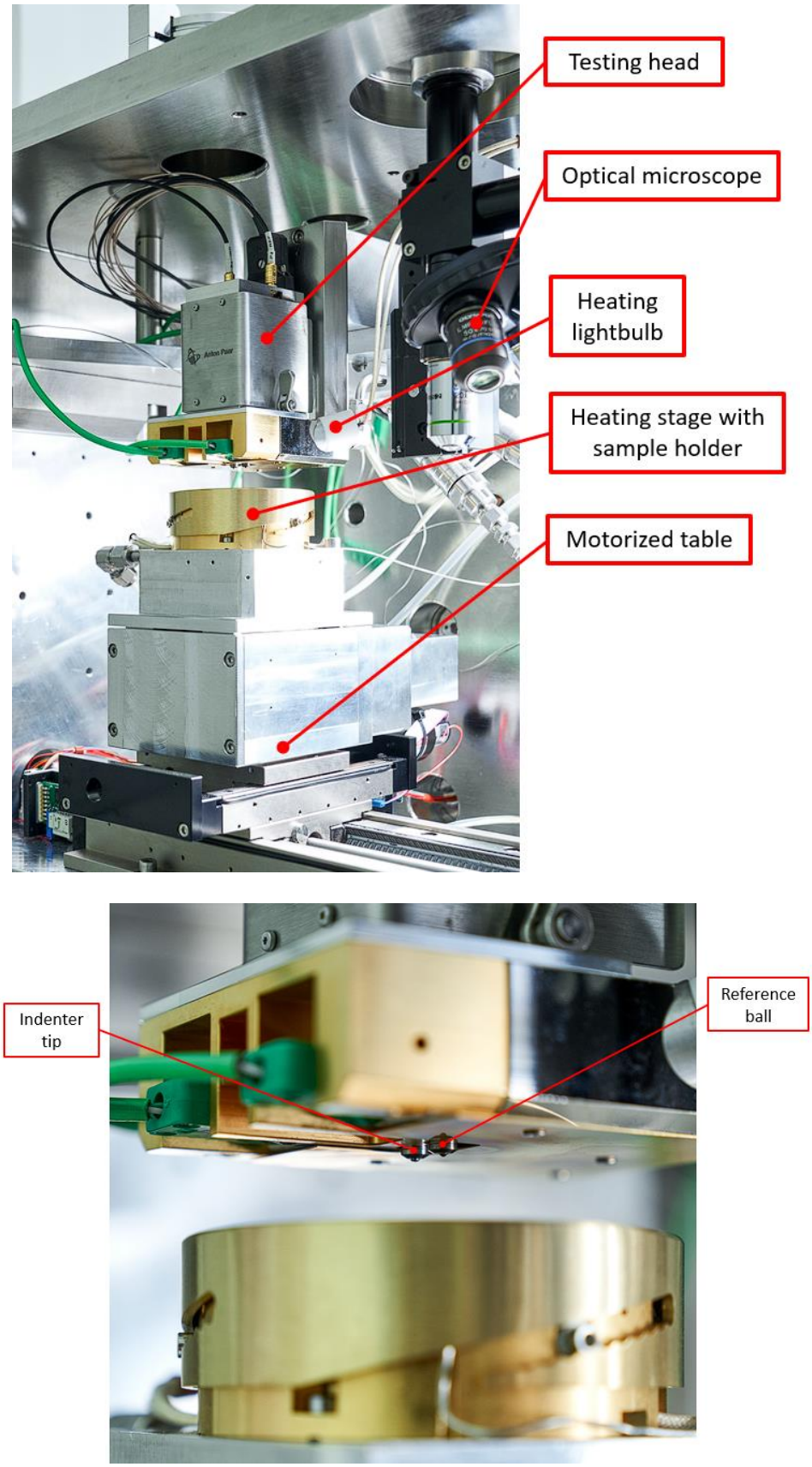

Figure 51. Anton Paar UNHT^3 main components inside a vacuum chamber. Copyright European Commission 2021.

High temperature nanoindentation using Berkovich tip has been performed on two different specimens: Eurofer97 in reference and irradiated state, each of them at room temperature, 300°C and 500°C. To analyze the hardness-depth profiles, which are important in the case of non-uniform ion damage distribution and, therefore, different material properties with respect to indentation depth, the tests were done at two different depths reached with 20 and 100 mN forces. The hardness and Young's modulus values were calculated using the Oliver-Pharr method [61] (Eq. (2.7)(2.6)).

The testing parameters used during the experimental campaign are collected in Table 8.

Single cycle	
Loading type	Linear loading/Force controlled
Max. load	20/100 mN
Loading/unloading time	30 s
Dwelling time	30 s
Acquisition rate	10 Hz

High temperature tests specifications	
Max. temperature drift	0.1 °C/min
Max. depth drift	10 nm/min

Table 8. Testing parameters used for high temperature nanoindentation.

One may note the same loading/unloading time for both maximum loads. The adjustment of the loading/unloading time to establish a similar indentation strain rate for the indentation cycles was mistakenly skipped, which will give a slight mismatch of hardness.

4.2.3.1 Nanoindentation results

The force-displacement curves obtained at different temperatures are provided in Figure 52, Figure 53, and Figure 54.

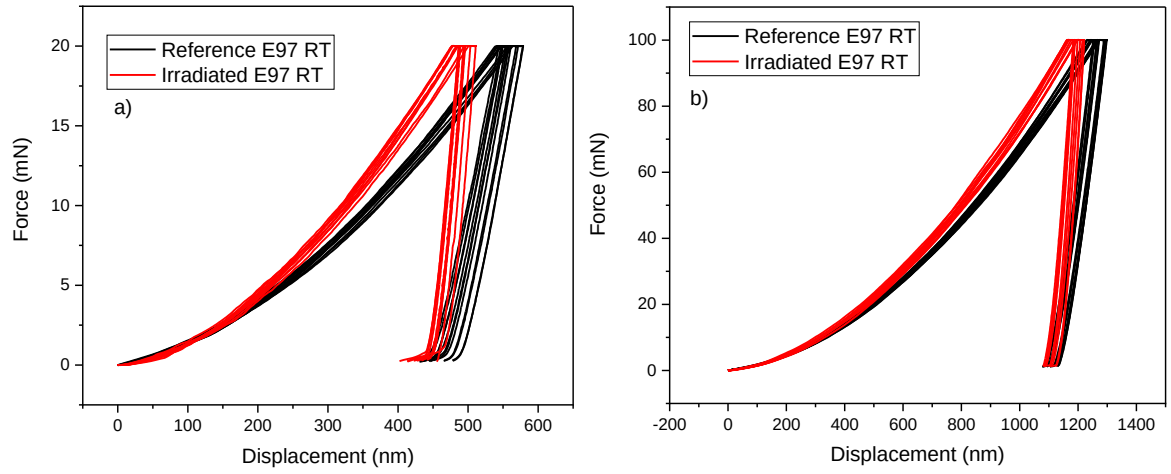

Figure 52. Force-displacement curves for reference (black) and irradiated (red) Eurofer97 tested at room temperature with: a) 20 mN, b) 100 mN force.

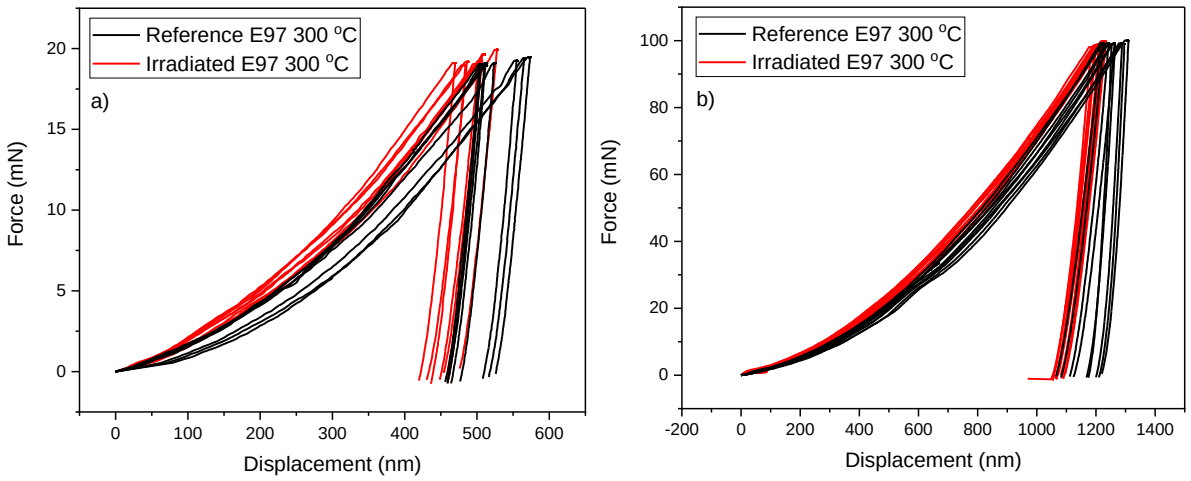

Figure 53. Force-displacement curves for reference (black) and irradiated (red) Eurofer97 tested at 300°C with: a) 20 mN, b) 100 mN force.

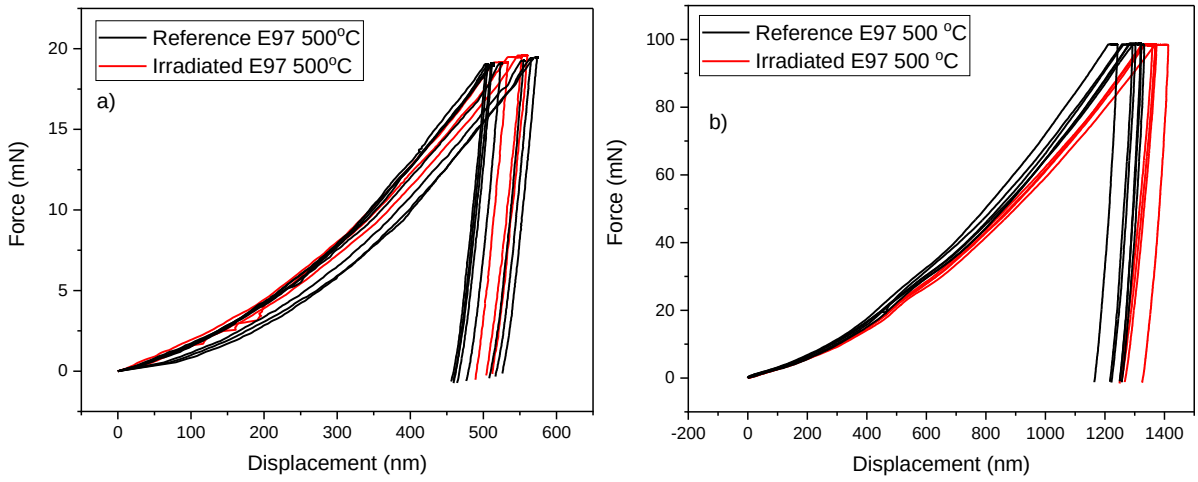

Figure 54. Force-displacement curves for reference (black) and irradiated (red) Eurofer97 tested at 500°C with: a) 20 mN, b) 100 mN force.

Several features can be observed. In Figure 52 one can see that the indenter with a force of 20 mN reaches ~450 nm of maximum depth in the ion-irradiated material and ~550 nm in the reference one; 100 mN gives the penetration until ~1200 nm for the irradiated material and ~1250 nm for the reference. This is expected because the unirradiated material is softer. The curves are very self-similar, which points to a successful experimental run. However, the unloading slopes differ in both states of the material, which consequently affects the hardness and Young's modulus calculations. This fact will be demonstrated, discussed, and accounted further in the text. The 300°C curves in Figure 53 reach around 500 and 530 nm with 20 mN in the irradiated and reference material respectively, and roughly 1200 and 1250 nm with 100 mN force. Additionally, their self-similarity is lower (especially the 20 mN ones) compared to the curves obtained at room temperature. This may be due to the presence of experimental artifacts or microstructural changes associated with elevated temperature. Eventually, the 500°C curves shown in Figure 54(a) reach the same depth of ~500 nm with a force of 20 mN. This points to thermal annealing of the irradiation damage, as the testing temperature in this case is higher than the irradiation temperature. The 100 mN curves in 54(b) even show the opposite behavior:

the tests carried out on the reference material reach lower depths (~1270 nm) than on the irradiated one (~1350 nm). Again, it must be an alignment of the microstructural states because of damage recovery.

Hardness and Young's modulus are calculated and presented in Figure 55.

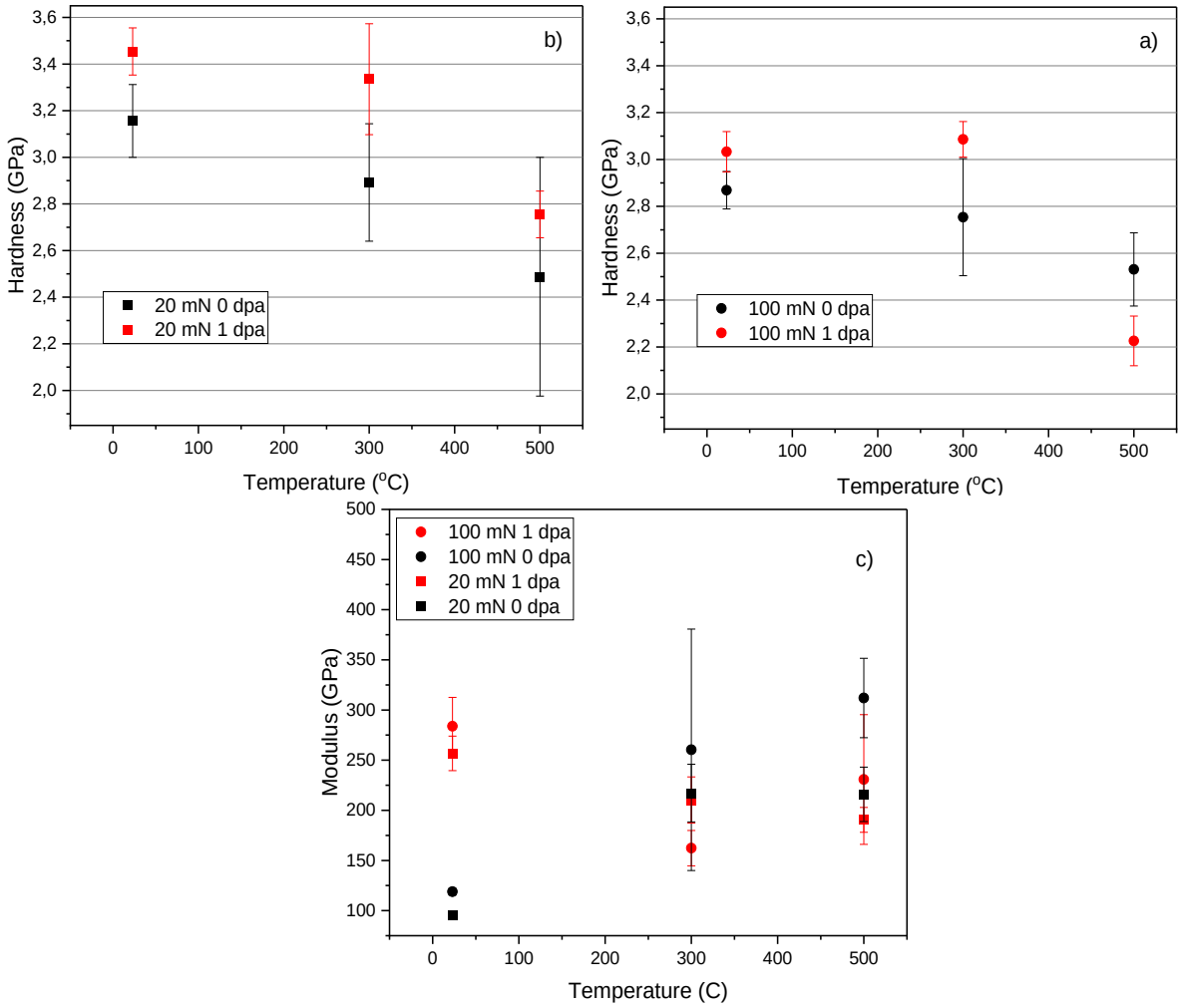

Figure 55. Hardness versus temperature from a) 20 mN and b) 100 mN force curves; c) Young's modulus versus temperature for both loads.

Figure 55(c) shows that the elastic modulus of the material does not agree well with the commonly established value (~210 GPa) measured by other methods. The measured unloading stiffness S is most likely affected by indentation pile-ups formation, which is a well-known problem [45]. As the testing temperature increases, the measured values tend to approach the expected value of Young's modulus. This is another confirmation, as the formation of indentation pile-ups is known and found to decrease with ambient temperature. As can be seen from the formulations (2.3), (2.4) and (2.7), a measured stiffness also affects hardness calculations. Since hardness is the most important quantity for this work, as the aim is to correctly analyze the impact of the irradiation effect on it, a stiffness correction procedure was applied, similar to the EMC procedure. It was possible because the value of the elastic modulus of the material is known, and it does not change or changes very slightly with irradiation. To apply the stiffness correction, the stiffness value S is manually adjusted to obtain the known value of Young's modulus E in formulations (2.5) and (2.6), thus correcting the contact depth

h_c and contact area A values (2.3), (2.4). Eventually, the corrected contact area is used to determine a new corrected hardness by using (2.7). After applying this EMC-like procedure, the new corrected values of hardness versus temperature were obtained and presented in Figure 56.

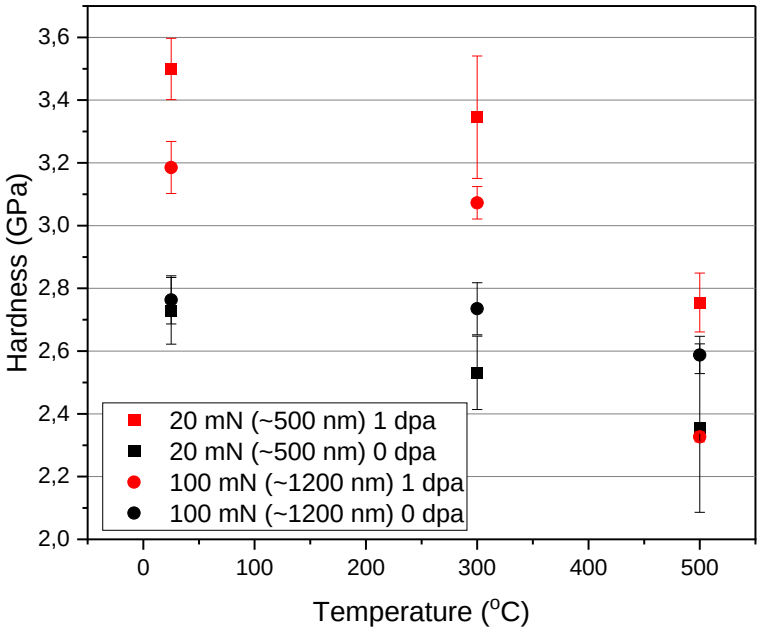

Figure 56. Corrected hardness versus temperature for reference and ion-irradiated Eurofer97 tested with 20 mN and 100 mN forces.

In Figure 56 one can clearly see the effect of irradiation hardening at room temperature and at 300°C: ~0.77 GPa with 20 mN and ~0.42 GPa with 100 mN force at room temperature; and ~0.815 GPa with 20 mN and ~0.34 GPa with 100 mN force at 300°C. However, at 500°C, the hardening seems to fade away, so that at 100 mN force the irradiated sample shows the same hardness as the unirradiated one. Similarly to the force-displacement curves, this is an expected observation, since the irradiation has been done at 300°C, so the damage should recover after heating to a higher temperature, so the microstructures of the samples become somewhat similar.

Another important observation is that H_{dpa} does not decrease once the temperature reaches 300°C, but becomes even greater. This is likely related to the thermally activated mobility of irradiation defects, which leads to their migration to the surface and the increase in density as the result, but not yet a damage recovery [107]. Another problem can be the limited number of data points obtained during the establishment of the contact between the surface and the indenter tip, which makes high temperature tests complicated in the correct determination of the contact point.

4.3 Microstructure investigations

4.3.1 Electron backscattered diffraction

Eurofer97 microstructure consists of complex features appropriate for steels, such as laths, blocks, and prior austenite grains (PAGs). Each feature has its own characterizing size and misorientation angle, which are dependent on the heat treatment of the material, and have an

influence on the mechanical properties [108]. The EBSD map of Eurofer97 obtained using Bruker ESPRIT software [109] is shown in Figure 57.

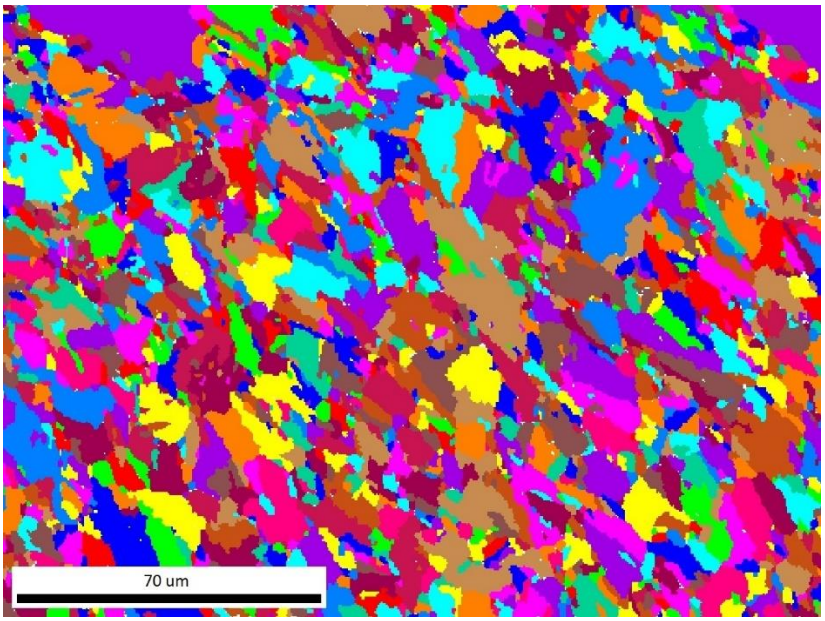

Figure 57. EBSD map of Eurofer97 steel.

On the EBSD map in Figure 57 the orientations of grains are not reflected, and the colors just represent each separate grain. The misorientation angle for this map has been chosen as 15°, which is typical for blocks, so the average block size was determined to be around 8 µm. The length scales for laths and PAGs cannot be estimated from this scan, however, it is known that laths in this material are typically 80-500 nanometers with 1-2° of misorientation angles, and PAGs are 30-50 microns misoriented on >20°.

The position of the nanoindentation test matrix was not analyzed, as the length scales of the microstructural features of Eurofer97 are comparable to the indentation imprints. It is very unlikely that at least two indents were placed onto two different blocks large enough to not affect the result by the adjacent blocks or their grain boundaries. The material response of Eurofer97 is correspondingly complex, as it is affected by the complex microstructure, whereas in the case of iron it is more similar to tests done on single crystals.

4.3.2 Scanning electron microscopy on nanoindents

The nanoindentation imprints on Eurofer97 in the reference and ion-irradiated states were also examined by SEM as presented in Figure 58 and Figure 59.

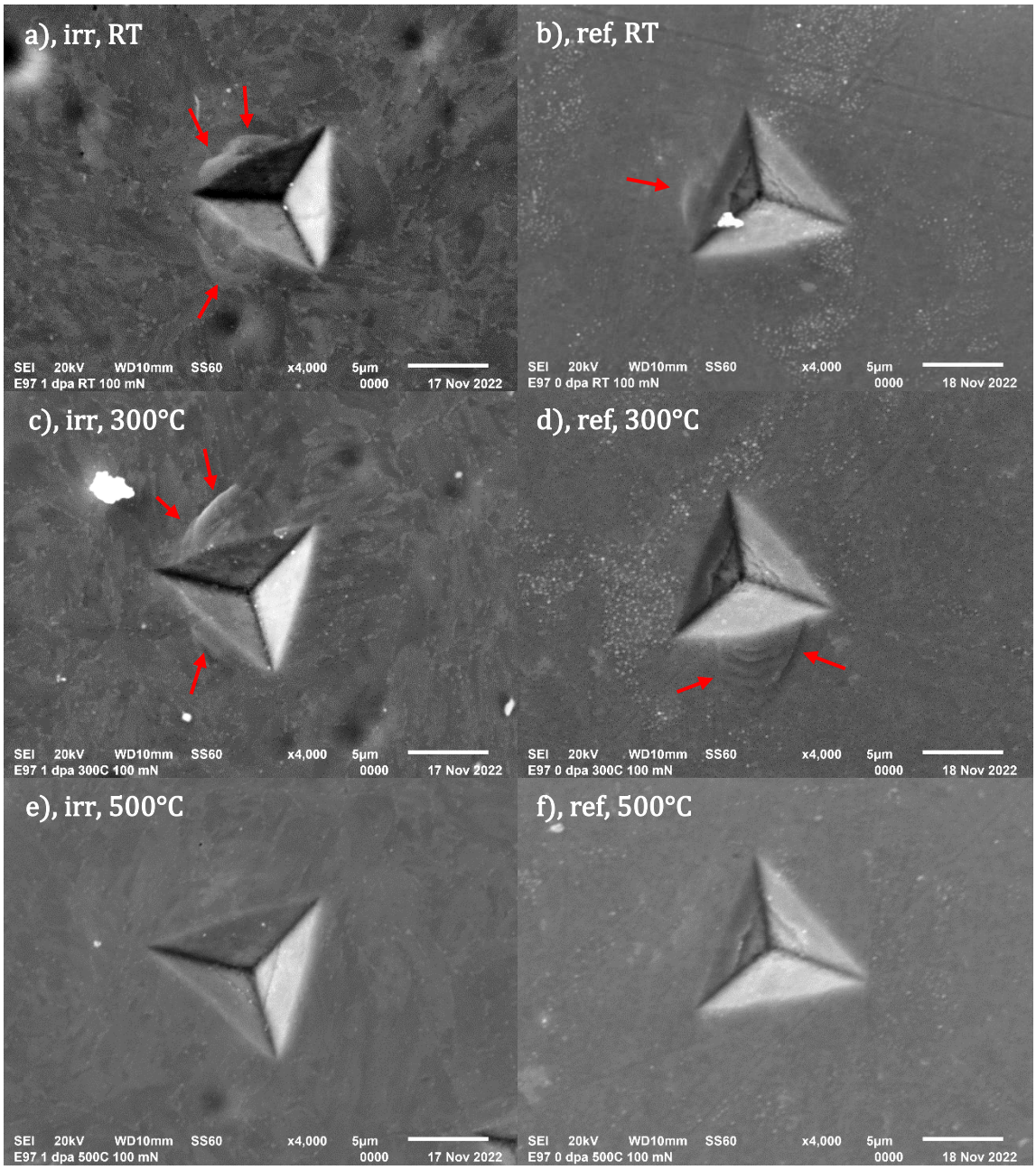

Figure 58. The shapes of nanoindents on Eurofer97 done at: a) room temperature, irradiated; b) room temperature, reference; c) 300°C, irradiated; d) 300°C, reference; e) 500°C, irradiated; f) 500°C, reference. The red arrows point to microfracturing.

Figure 58 has been composed in the way that one could observe the microfracturing which occurs instead of smooth piling-up as in the case of iron, especially as the maximum depths are around three times lower. This must be associated with the fact that Eurofer97 has a lower plastic capacity, so it cracks where the iron is still plastically deformed (see Figure 18 and Figure 49 (a)). Also, the indents done at 500°C show neither microfracturing nor significant pile-ups, which is expected due to the thermally enhanced plasticity at this temperature. Nevertheless, this is not a regular phenomenon, and some examples without fracturing are given in Figure 59.

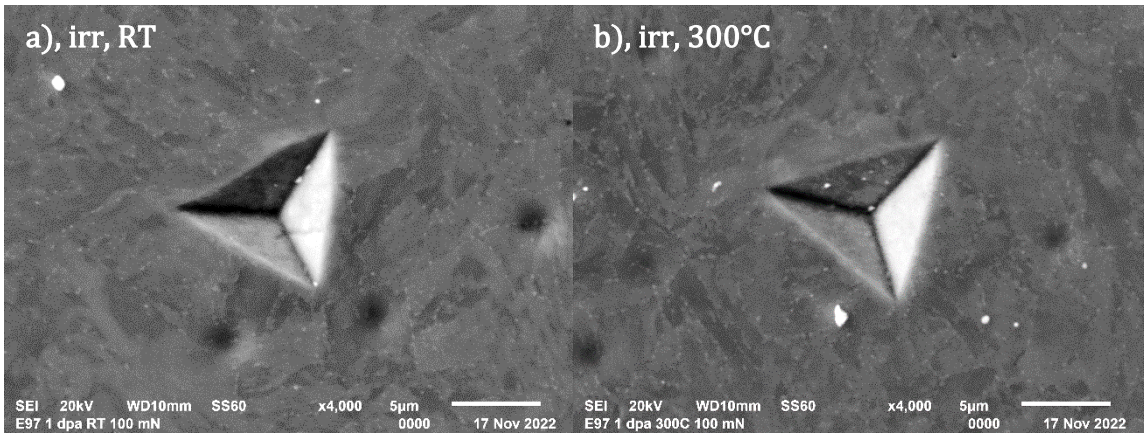

Figure 59. The shapes of nanoindents on Eurofer97 without microfracturing done at: a) room temperature, irradiated; b) 300°C, irradiated.

As can be concluded from Figure 59, no differences have been observed between the indents done on the reference and ion-irradiated states of the material.

4.3.3 Transmission electron microscopy in bulk

The same evaluation of the dislocation density has been performed for Eurofer97, however, only in the as-received state without pre-straining. Nevertheless, this should not be a problem, as the parameters responsible for the evolution of the dislocation density can still be determined by fitting the computational output to the experimental tensile stress-strain curve. The initial dislocation density of Eurofer97 has been calculated as $1.5 \cdot 10^{14}$ m^{-2}, and the corresponding TEM images are presented in Figure 60.

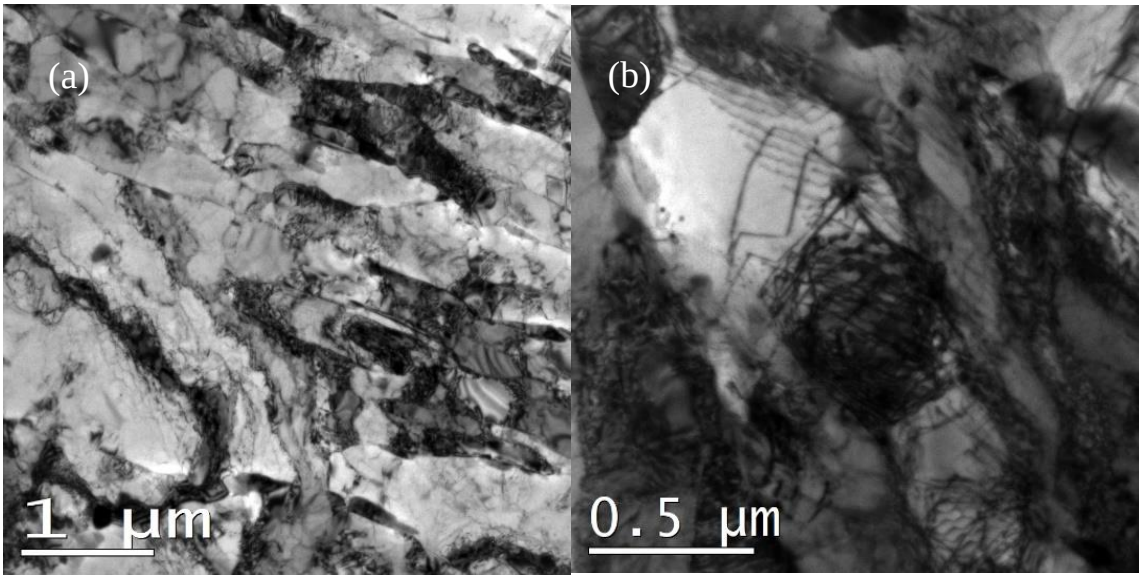

Figure 60. TEM images of Eurofer97 microstructure.

Figure 60(a) represents the typical ferritic/martensitic microstructure of Eurofer97 with laths and carbides, whereas Figure 60(b) shows one of the dislocation forests used for determination of the dislocation density.

4.4 CPFEM analysis of the reference and ion-irradiated Eurofer97

4.4.1 Establishment of the material law using uniaxial tensile tests

4.4.1.1 Unirradiated material

To establish the elastoplastic behavior of the material, a set of parameters responsible for the formation of the dislocation slip described in the paragraph §2.4.1.1 had to be determined. The following information was obtained similarly to the pure iron case described in §3.2.1 with slight changes due to the absence of TEM measurements in the deformed state. The number of slip systems used was 24, the elastic constants C_{11}, C_{12}, and C_{44} were taken from [93] (assumed to be constant for all of the studied temperatures), Burgers vector was taken for the $\frac{a}{2}\langle 111\rangle$ dislocation (so the magnitude of the Burgers vector is $\sqrt{3}\frac{a}{2}$), where a is α-Fe lattice parameter of 2.856 Å [94] (assumed to be constant for all of the studied temperatures), and the kink pair formation enthalpy was determined in Ref. [95]. The latter value was not changed from the value used for iron, as it was already high and nevertheless gave a good fit once replicating the constitutive laws of both materials. The initial dislocation density was taken from the TEM measurements presented in §4.3.3, but lowered from $1.5\cdot10^{14}$ m^{-2} to $5.5\cdot10^{13}$ m^{-2} what can be explained by a smaller fraction of mobile dislocations compared to the total measured value. Other parameters had to be fitted in order to correctly reproduce the true stress-strain ($\sigma-\varepsilon$) curve shown in Figure 49.

The summary of the parameters applied in the set of constitutive equations is provided in Table 9.

Parameter	Value	Source
Elastic coefficient, C_{11}	230 [GPa]	Literature [93]
Elastic coefficient, C_{12}	135 [GPa]	Literature [93]
Elastic coefficient, C_{44}	117 [GPa]	Literature [93]
Burger's vector, b	0.2482 [nm]	Literature [94]
Reference slip rate, $\dot{\gamma}_0$	10 [s^{-1}]	Fitted
Lattice friction stress + Hall-Petch stress + other strengthening mechanisms, S_0	100 [MPa]	Fitted
Initial dislocation density, ρ_0	$5.5\cdot10^{13}$ [m^{-2}]	Measured/Artificially decreased
Kink pair formation enthalpy, $2H_k$	2.365 [eV]	Literature [95]/Artificially increased [96]
Dislocations interaction strength, h_{dis}	0.115 - 0.13	Fitted
Saturated dislocation density, ρ_{sat}	$2.75\cdot10^{15}$ [m^{-2}]	Fitted
Kocks-Mecking parameter, k_1	$9.4\cdot10^{8}$ - $1.5\cdot10^{9}$ [m^{-1}]	Fitted
Thermal stress, $\hat{\tau}$	115.0 [MPa]	Fitted

Table 9. The list of constitutive parameters used to simulate the material law of the unirradiated Eurofer97.

Must be added that in the case of Eurofer97 steel, which has a more complex microstructure than pure iron, the S_0 parameter from (2.14) is now playing an additional role of other strengthening mechanisms, such as solid solution strengthening, precipitation hardening, or transformation hardening due to martensite formation. Further, this parameter will be used to introduce radiation-induced hardening for the simulations of the irradiated material.

As before, the dislocation interaction strength parameter h_{dis} decreases with temperature, which is the correct trend for BCC metals [80]. It is equal to 0.13 at room temperature and 0.115 at 300°C. Additionally, the Kocks-Mecking k_1 parameter grows proportionally to the temperature ($9.4 \cdot 10^8$ m^{-1} at room temperature and $1.5 \cdot 10^9$ m^{-1} at 300°C), what basically means a slight decrease of uniform elongation. These are expected phenomena once dealing with BCC steels, including Eurofer97 [31].

The constitutive parameters presented in Table 9 are correspondingly used to perform the uniaxial tension simulations applied to a polycrystalline sample consisting of 1000 grains. The computational cell is stretched in the direction *x* at a given temperature and strain rate and is free to deform along the directions *y* and *z*. The $(\sigma - \varepsilon)$ curves obtained from those simulations carried out at room temperature and 300°C are presented in Figure 61(a). To demonstrate the quality of the obtained match, the ratio of the simulated curve to the experimental one was expressed in percent and plotted versus true strain starting from ε_{true} = 0.2% in Figure 61(b). As can be seen, the maximum difference between the pair of experimental and simulated curves remains within 1% for both temperatures. The yield stress values agree with experimental data within 5% of divergence.

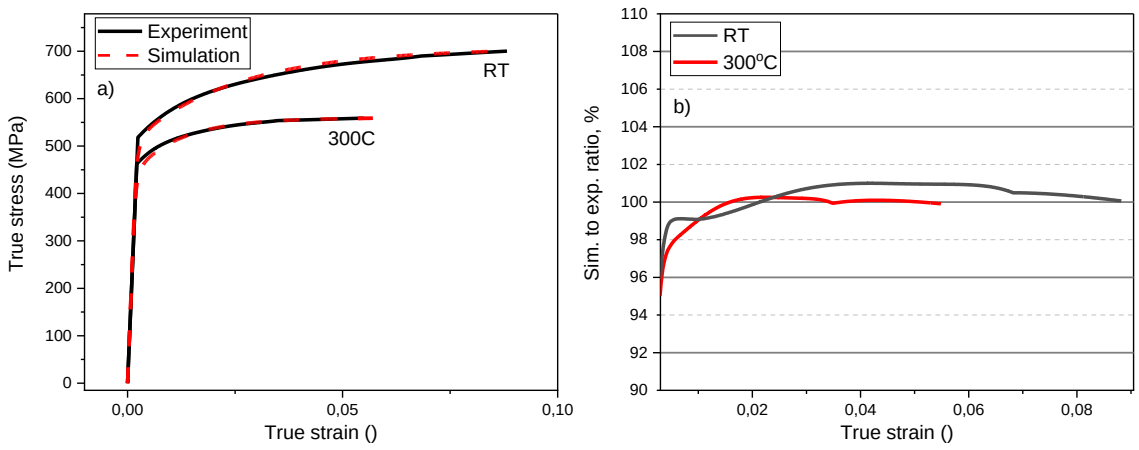

Figure 61. a) Simulated (dashed red) and experimental (solid black) true stress-strain curves of the unirradiated Eurofer97 in comparison, b) simulation to experimental σ-ε curves ratios in percent.

Upon analysis of the stress-strain curves of Eurofer97, one can see a lower uniform elongation compared to pure iron. Therefore, to further confirm the validity of constitutive laws, a simulation of a flat tensile specimen was performed. A specimen of dimensions similar to those used in the experiments ($5.2 \times 1.6 \times 0.75$ mm^3 in gauge) to the one used in the experiments has been constructed. The mesh was refined and structured in the middle of the gauge, where the localization of the deformation is expected. Overall, the mesh consists of 4094 nodes and 3272 1st-order hexahedral elements with volume averaging correction on the volumetric deformation gradient. The bottom plane of the specimen was fixed along the *x*, *y*, and *z* axes. The reader can familiarize themselves with the final look of the constructed geometry and meshing by checking Figure 62. The stress distribution at ε_{eng}= 23% and at room temperature

can be seen in Figure 63. The top plane was displaced along the *y* axis and fixed along the *x* and *z* axes to establish uniaxial deformation. Time and elongation were chosen in order to reproduce the strain rate used in the experiments ($2.78 \cdot 10^{-4}$ s^{-1}). Homogenization rules were applied to obtain an averaged response equal to 200 randomly oriented crystal orientations. This amount could decrease the CPU demand using FEM, while its response in the standalone mode was ensured to be almost equal to the 1000 grains case.

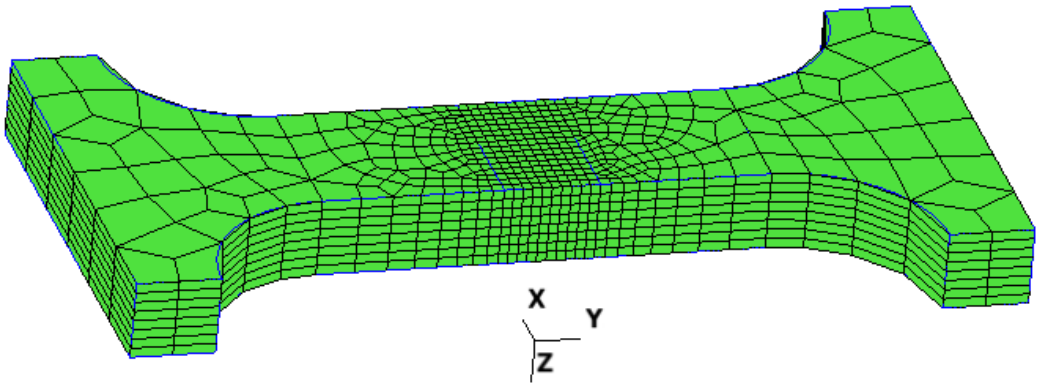

Figure 62. FEM setup of a flat tensile specimen.

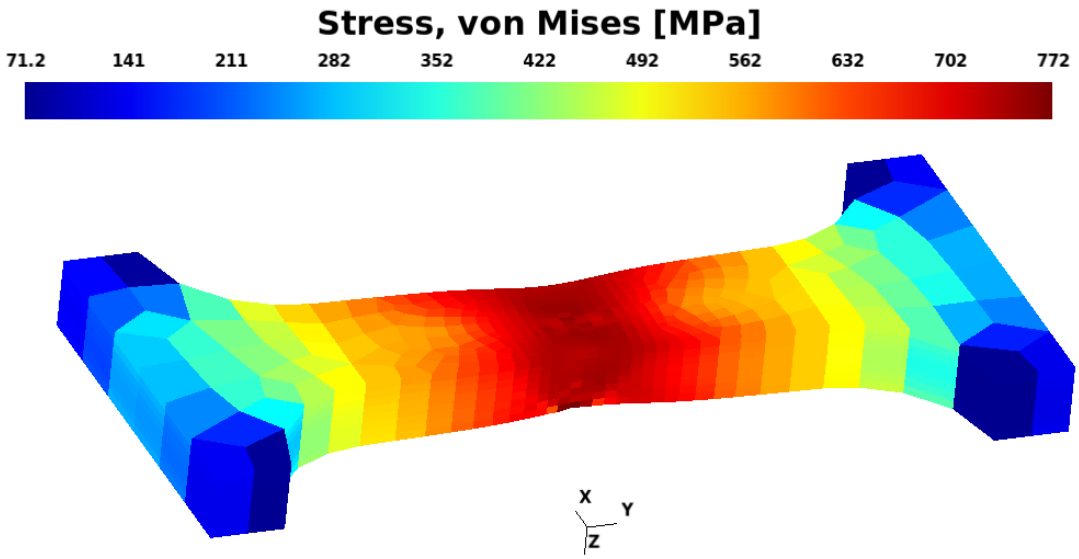

Figure 63. Von Mises stress distribution in the flat tensile specimen at ε_{eng} = 23%.

To confirm mesh applicability, another simulation was performed with twice lower the size of the elements in the middle of the sample. The mesh sensitivity analysis obtained is shown in Figure 64.

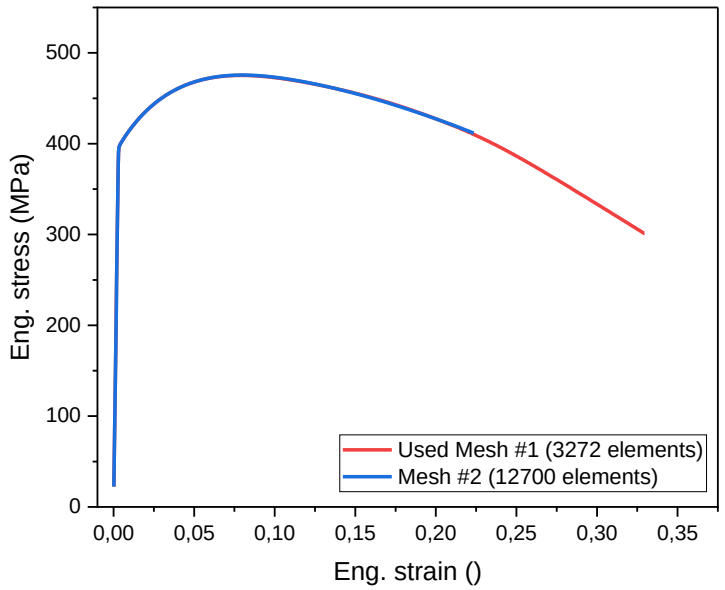

Figure 64. Mesh convergence analysis of the flat tensile FEM setup.

Figure 64 clearly shows that lowering the element size of the applied mesh does not affect the simulation result. It must be added that this analysis has been performed without applying the homogenization rules (only 1 grain is considered).

The simulated engineering stress-strain curves compared to the experimental ones from Figure 49 are provided in Figure 65.

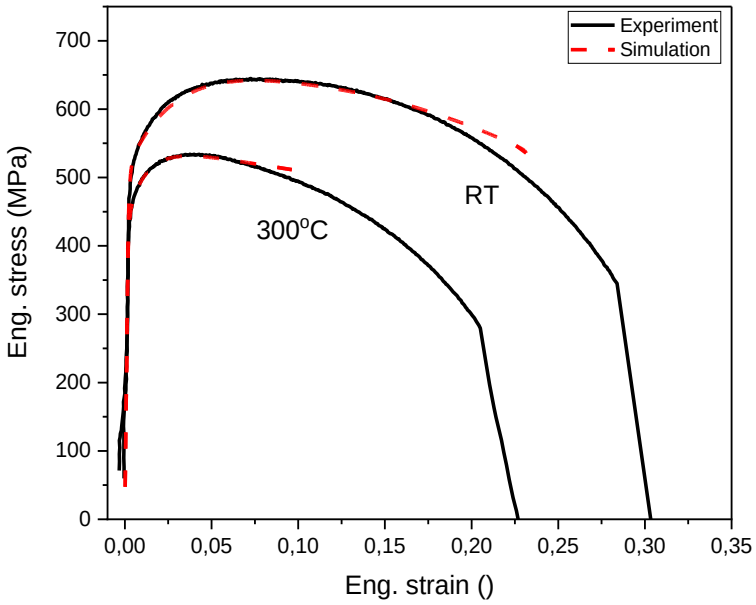

Figure 65. Simulated (dashed red) and experimental (solid black) engineering stress-strain curves of Eurofer97 in comparison.

One can see in Figure 65 that the presented approach of the flat tensile simulation allowed the validity of the constitutive laws to be confirmed until ~20% of strain at room temperature and ~10% at 300°C. This is around twice as much as by using just true stress-strain curves and

the standalone mode. For higher levels of stress, the considered true stress-strain conversion does not hold because of the non-uniform deformation, and the hardening law identification should be performed on the 3D simulation. Besides, beyond 20% and 10% deformation at respectively RT and 300°C, a significant damage nucleation onsets its strong contribution to the loss of ductility. However, no damage nucleation models were implemented in the computational framework used. Consequently, the plastic behavior of the stress-strain curves can diverge in high strains, as observed in Figure 65.

4.4.1.2 Radiation-affected material laws

To establish the material laws of the radiation-affected zones and simulate the irradiation hardening, the dpa dose distribution along the subsurface of the specimen must be differentiated into layers and analyzed. The constitutive parameter S_0 from the equation (2.14) responsible for the different hardening mechanisms will be parametrized to associate yield stress or hardness with a certain magnitude of the damage dose. In the case of this work the S_0 values are fit to the yield stresses from the real tensile tests of neutron-irradiated Eurofer97 shown in Figure 50. Then the established constitutive laws are transferred to the subsurface layers of the specimen box to simulate the ion-irradiated material. On replication of the experimental nanoindentation data, the interconnection between irradiation hardenings caused by ions and neutrons can be confirmed through the modified material laws.

To associate radiation-induced hardening in terms of yield stresses with the damage dose, the following formula has been used:

$$\Delta\sigma_{YS} = hd^n \qquad (4.1)$$

where $\Delta\sigma_{YS}$ is the irradiation hardening (the difference between the yield stresses of the reference and irradiated materials) in MPa, d is the damage dose in dpa, h and n are the fitting parameters. This power-law expression is one of the simplest models for irradiation hardening [110]. To find the $\Delta\sigma_{YS}$ values to apply in the simulations of the nanoindentation process, the tensile tests data of the neutron-irradiated Eurofer97 from Figure 50 have been used.

Now, the power law regression method can be used to deduce the h and n parameters to establish the power law relationship and apply it for the ion irradiation damage-depth profile presented in Figure 48. This will allow to see the irradiation hardening distribution along the subsurface of the ion-irradiated nanoindentation specimen through the association of the magnified yield stresses and damage doses. Power law regression is performed for both temperatures.

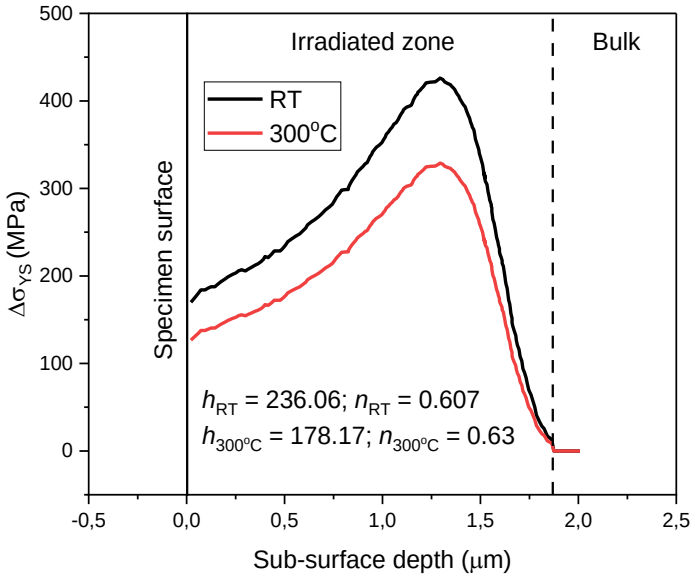

Figure 66. The magnitude of irradiation hardening in ion-irradiated Eurofer97 with respect to depth.

Figure 66 shows the distribution of irradiation hardening due to the floating damage dose introduced by ion irradiation. However, since only four layers are available to imitate hardening (Figure 11), the damage dose in dpa is differentiated and averaged by each layer of 0.5 μm depth. Then the S_0 parameter is parameterized by performing simulations of the uniaxial tension in the standalone mode. This will allow to obtain yield stresses at these averaged doses, in accordance with Figure 67.

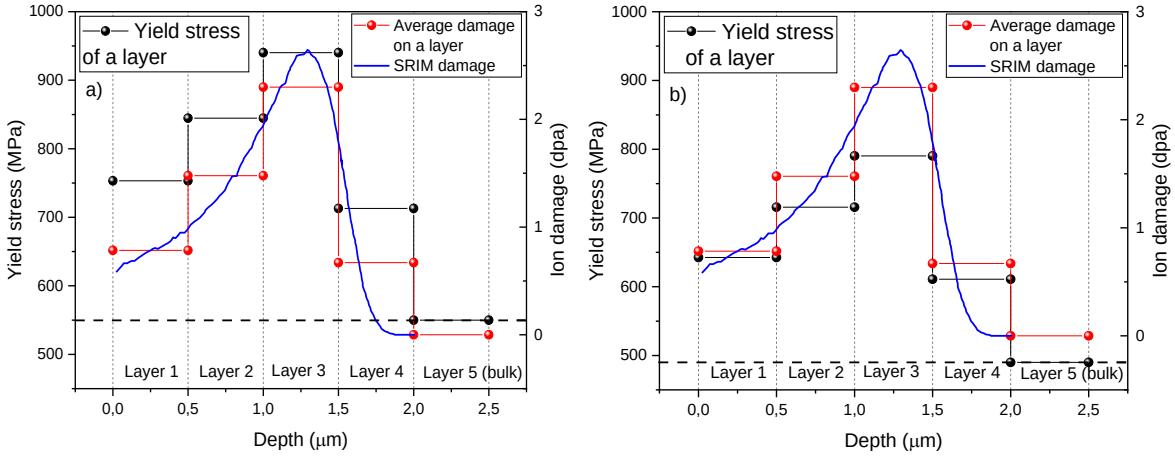

Figure 67. The damage-depth profile from SRIM (blue), the average dose on each layer (red), and the corresponding yield stress (black). a) Room temperature; b) 300°C.

One can note that the peak dose of 2.3 dpa in layer 3 in Figure 67 is higher than the measurement range provided in Figure 50. Therefore, the corresponding yield stress is extrapolated according to the power law applied to establish the hardening-depth profile (Figure 66). Once experimentally validated, this may point to the predictive capability of the method. However, since irradiation hardening is known to saturate at higher damage doses [111], an appropriate characterization dpa range must be chosen for each new material. On the other hand,

more advanced models of irradiation hardening accounting the saturation mode can be used instead of (4.1) (an example of such a model can be found in [110]).

Figure 68 collects true stress-strain curves simulated using the standalone mode in accordance with Figure 67 for both temperatures.

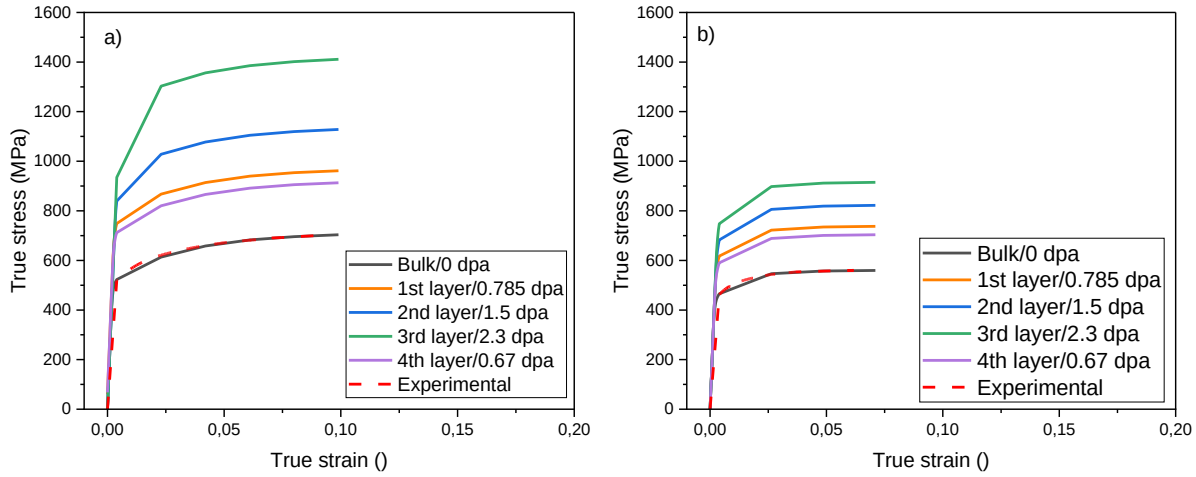

Figure 68. True stress-strain curves obtained from uniaxial tension simulations in the standalone mode. The S_0 parameter is adjusted until the reproduction of the yield stresses is obtained at a certain dose. a) Room temperature; b) 300°C.

It is important to understand that irradiation damage causes not only irradiation hardening, but also a reduction of uniform and total elongation [105] [112], so the constitutive laws presented in Figure 68 are not completely representative in the plastic mode. However, this work is focused on the application of nanoindentation as the main experimental technique, which is capable of hardness measurements (tightly connected with yield stress). There is no simple way to estimate the plastic behavior using just nanoindentation with Berkovich indenter; therefore, it is assumed that plasticity has not undergone any changes. This assumption must be sufficient in terms of determining irradiation hardening using the presented methodology.

Another point is that the presented approach is empirical rather than analytical. While based on the analytical formulation for dislocation dynamics, no equations were introduced for the behavior of irradiation defects, their densities, or types. Therefore, the S_0 parameter is used as an accumulative parameter, empirically reproducing the magnitude of irradiation hardening and other hardening mechanisms. Moreover, an introduction of such equations could increase the accuracy of the results, make the description of different hardening phenomena more fundamental and distinguishable. The obtained values of S_0 are given in Table 10.

Layer #	Damage dose, dpa	Yield stress at RT, MPa	S_0 at RT, MPa	Yield stress at 300°C, MPa	S_0 at 300°C, MPa
1 (surface)	0.785	753	190	643	163
2	1.5	845	250	716	193
3	2.3	940	350	790	226
4	0.67	713	170	611	151
5+ (bulk)	0	550	100	490	100

Table 10. Yield stresses and the corresponding S_0 values with respect to the damage dose at room temperature and 300°C.

Furthermore, by substituting the reference (bulk) value of S_0 from the ones affected by irradiation, the contribution of irradiation hardening to the critical resolved shear stress in a slip system α can be estimated. Values for both temperatures are presented in Figure 69.

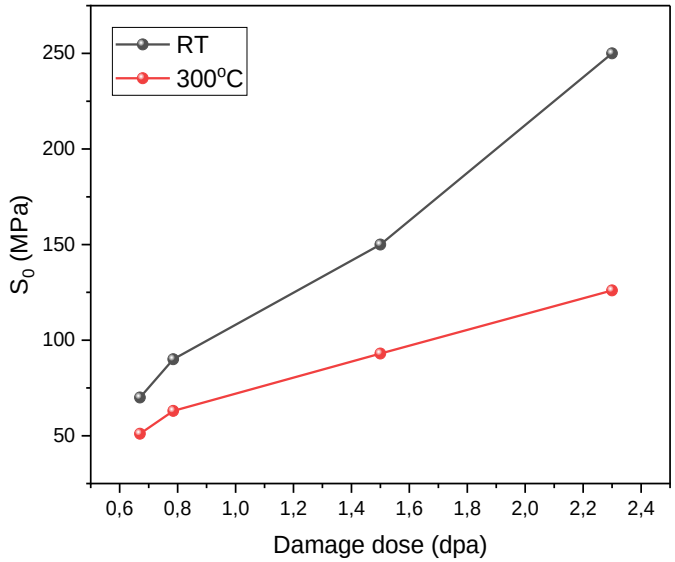

Figure 69. Stress contribution from irradiation hardening to the CRSS in a slip system α for room temperature (black) and 300°C (red).

The trend reflected in Figure 69 is correct, as the higher damage dose increases this contribution due to the higher density of the introduced irradiation defects. At the same time, the values decrease with ambient temperature, as the dislocation-defect interactions are thermally powered.

4.4.2 Nanoindentation simulations of the reference and ion-irradiated material

4.4.2.1 FEM setup

To simulate the nanoindentation process in ion-irradiated material, the previously described in §3.2.2.1 FEM setup was modified. As the experimental maximum depth is now limited to 1.25 µm, the specimen box size was reduced to 50 × 50 × 13 µm^3. However, the main newly introduced feature is the division of the 2 µm deep subsurface into four layers (see Figure 71), which represents the volume affected by ions. Each layer is equal to the depth of 0.5 µm and will eventually be assigned with a different material law. The established FEM model is given in Figure 70.

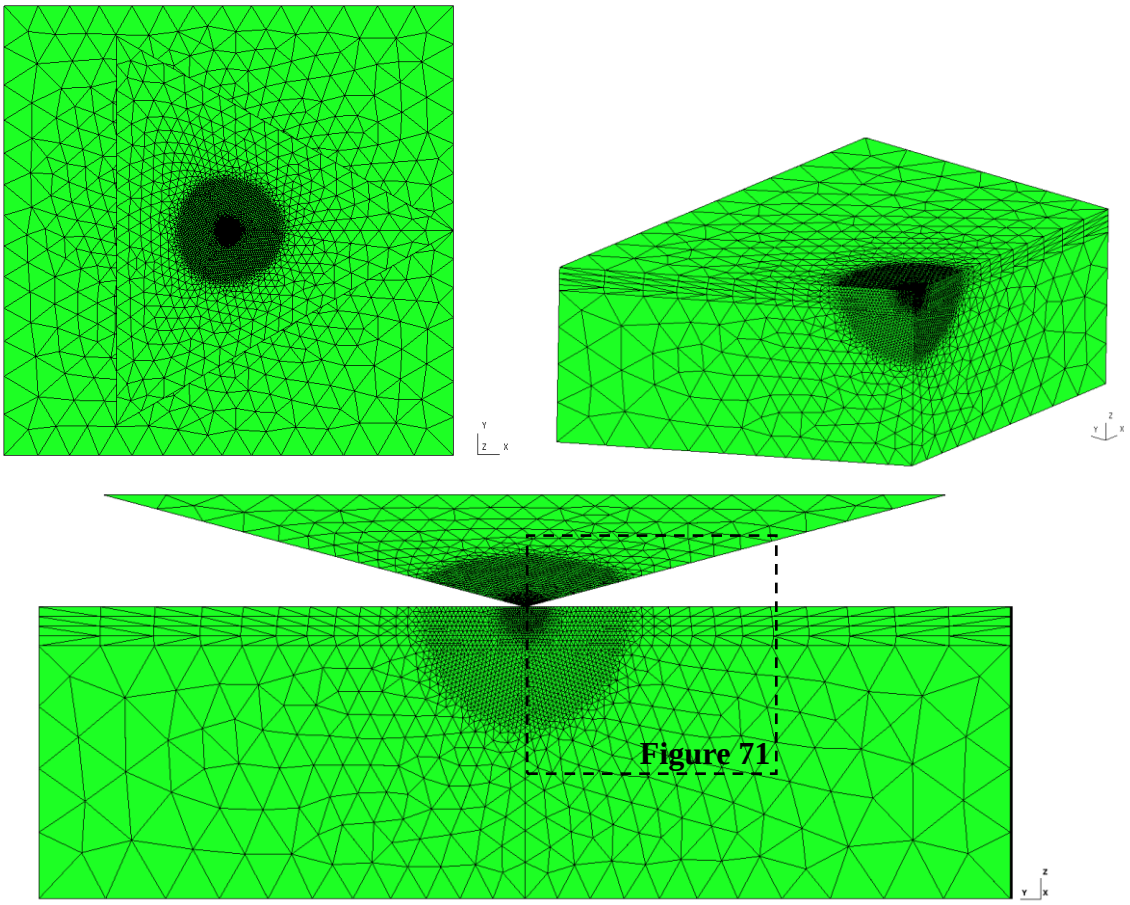

Figure 70. The FEM setup used for the simulations of the nanoindentation process in ion-irradiated Eurofer97.

During the mesh sensitivity analysis for this setup, it was found that the elastic regime prevailing on the first steps of indentation significantly contributes to the calculated hardness-depth profile on shallow depths. Moreover, this contribution strongly depends on the element size in the initial contact zone, thus, as the elements are smaller, the elastic regime fades sooner. This fact is visualized in Figure 72. Therefore, it was important to find the proper element size with absence of the elasticity at least at 500 nm depth, where the experimental validational value is known. On the other hand, the element size must be chosen in a way where the computing ability of the FEM workstation is still present and provides reasonable time ranges. To do this, a uniform mesh was generated and its refinement in the deforming area was obtained with two spherical mesh fields of different radii (see Figure 71). The first sphere has a radius of 1.3 µm and characteristic mesh length of 0.125 µm (to exclude the elastic effect on shallow depths), while the second sphere has a radius of 6 µm and characteristic mesh length of 0.25 µm (to save CPU resources). The area of the specimen box without expected deformation smoothly transits to the elements with characteristic mesh length of 5 µm at maximum.

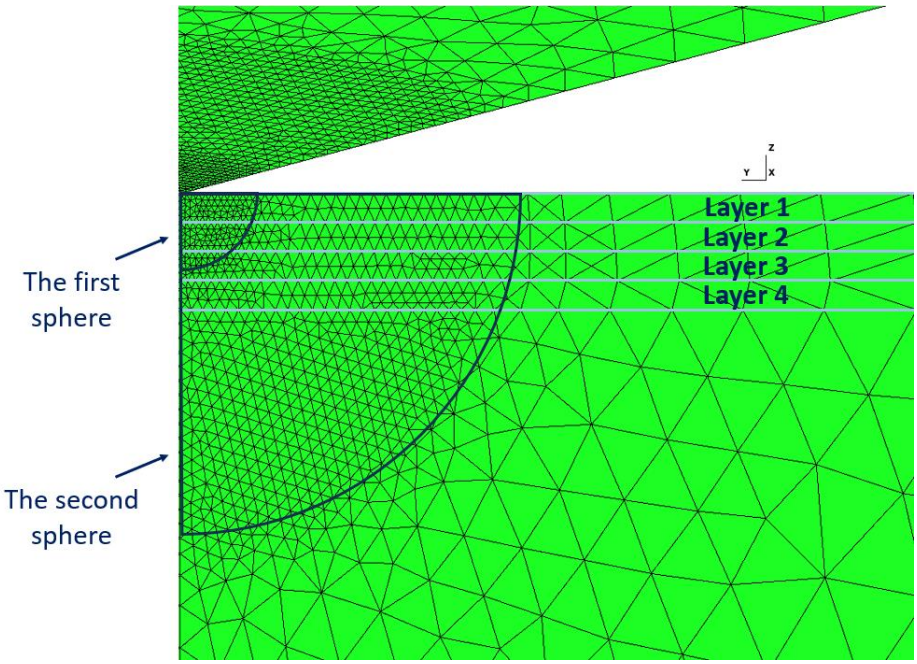

Figure 71. Layering and meshing used in the FEM nanoindentation setup of the ion-irradiated specimen.

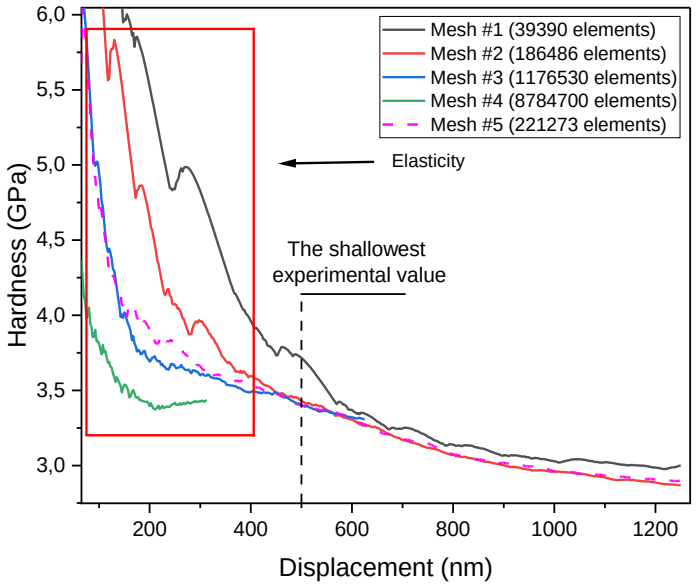

Figure 72. Mesh convergence analysis on the ion-irradiated material.

In Figure 72, one can see how the elastic regime can contribute to the initial magnitudes of hardness. When modeling the radiation-induced hardening, it is very important to minimize these contributions, as they can distort the difference when hardness is compared to the reference material or experimental data. The mesh convergence analysis has been done by applying the following meshes: Mesh #1 – one 6 µm radius refinement sphere with a characteristic mesh size of 0.5 µm inside it; Mesh #2 – 6 µm radius sphere and 0.25 µm mesh size; Mesh #3 – 6 µm radius sphere and 0.125 µm mesh size; Mesh #4 – 6 µm radius and 62.5 nm size. Mesh #5 was constructed of two spheres as specified before.

The largest Mesh #1 gives fast calculation time, however, the error which comes from elasticity goes beyond the available experimental value. Mesh #2 works well, but it is less accurate than Mesh #3 at depths less than 400 nm. On the other hand, Mesh #3 is already too volumetric, so in order to run this simulation, the dimensions of the specimen box have been proportionally reduced, which gives the maximum depth of 600 nm only. Mesh #4 seems to be perfect, as it catches the increase in hardness as it approaches Bragg's peak, so it is the most unaffected by elasticity. However, the geometry has been reduced so much that only 300 nm of depth could be reached, while calculating for unreasonably long. Using Mesh #4 could be worth using supercomputers instead of a workstation.

Mesh #5 used in this research is constructed of two spherical mesh fields, as was specified before (unlike Meshes #1-4 of only one) and combines the relatively fast calculation time of Mesh #2 and the accuracy of Mesh #3. Again, if a supercomputer was used, this method could be used to construct an intermediate mesh of Mesh #3 and Mesh #4 with decent accuracy and calculation time.

Eventually, the applied Mesh #5 consists of 221273 1st-order tetrahedral elements, where locking is avoided by averaging the volumetric deformation. The simulation was carried out along the surface orientations [100], [101], and [111] and the responses were averaged.

4.4.2.2 Simulations

By applying the described in §4.4.2.1 FEM setup, the nanoindentation tests were simulated at room temperature and 300°C; however, the loading time was chosen as in the 100 mN tests (30 s to ~1200 nm), which is not well representable for 20 mN simulations. In the case of reference material, each layer was assigned with the same material law derived from the tensile tests carried out on non-irradiated material, as described in §4.4.1.1. To simulate the ion-irradiated material, the layers were assigned with the corresponding combination of damage dose and constitutive law, as previously described in §4.4.1.2. The resulting force-displacement curves were obtained with respect to the three crystal orientations and then averaged to provide a comparison with the experimental ones, as presented in Figure 73. As in the case of iron, the difference between different orientations is low and equals approximately 3.5%. The experimental curves are taken from Figure 52 and Figure 53 and averaged, where the *x* error bar shows the divergence between each single nanoindentation cycle. The difference at h_{max} between the experimental and the simulated curves is the highest in the case of reference material tested at 300°C and equals 8.8%.

Figure 73 a better similarity between the curves compared to iron (§3.4.2.2), especially considering lower maximum depths (~1.2 µm vs. ~3-4 µm). This points to a weaker contribution from the indentation size effect in Eurofer97. It is expected, as the microstructure of steel is more heterogeneous because of the high defect density and significantly smaller grains, thus reducing the characteristic length of the strain gradients. Irradiated curves tested at room temperature show a very high similarity, as the characteristic length is even lower because of the introduced irradiation defects, thus approaching the material state to the minimal ISE. The reduction of the ISE after irradiation is a known behavior according to Refs. [58] [113].

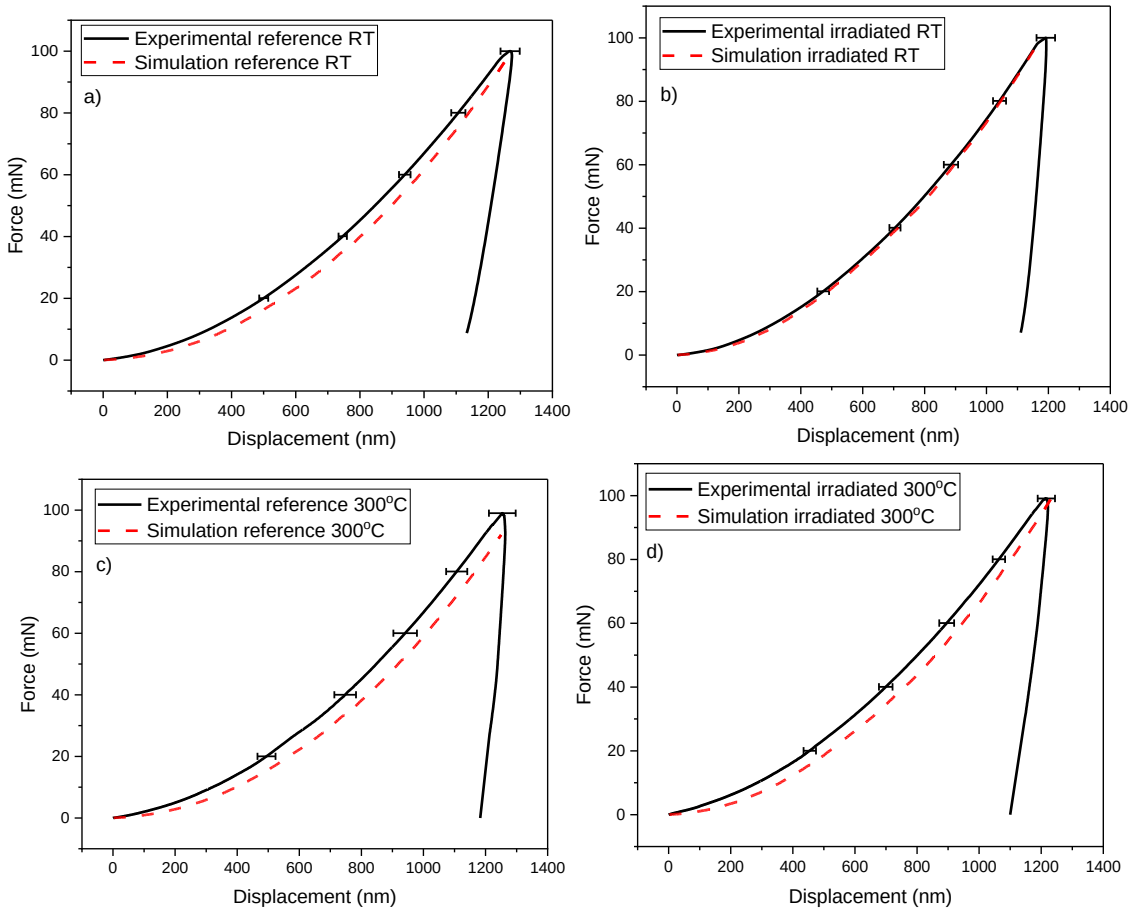

Figure 73. Averaged nanoindentation force-displacement curves obtained from the experiment (black) and FEA (red) in comparison: a) room temperature, reference; b) room temperature, irradiated; c) 300°C, reference; d) 300°C, irradiated.

As before, the simplified formula for hardness (3.2) is applied. However, hardness is now calculated as a function of depth to obtain the hardness-depth profiles for each case. These profiles are compared to the experimental single cycle indentations at two different depths and are shown in Figure 74.

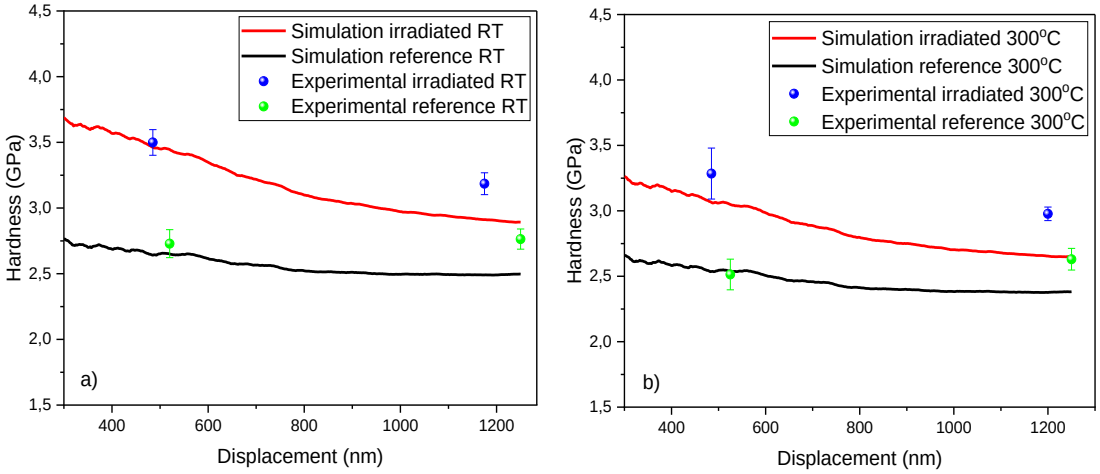

Figure 74. Hardness-depth profiles from the simulations and experimental single cycle values: a) room temperature; b) 300°C. Experimental values reach ~500 nm with 20 mN and ~1250 nm with 100 mN.

In the case of room temperature, one can see a good match between the simulated curves and the experimentally obtained values. The highest difference does not exceed 9%. Furthermore, during the experimental campaign the 20 mN indentations were mistakenly performed with the same loading time as the 100 mN indentations, giving inconsistency of the strain rate and a slight underestimation of hardness for the values obtained at ~500 nm depth. On the other hand, if the contact depth was used instead of the maximum depth ($h_c < h_{max}$) in simplified hardness calculations (Eq. (3.2)), this would give a shift-up of the simulated hardness-depth curves along the *y* axis, making them match 100 mN values and being higher than 20 mN values (which are also lowered due to the strain rate incompatibility). To minimize all these incompatibilities, the difference between the irradiated and reference curves is recommended to be used for the comparison, as will be demonstrated further.

Another situation is with the 300°C case. Once again, the 20 mN values must be slightly higher, and the difference is less than 12%. However, the divergence in this case is due to the unexpected increase in irradiation hardening at 300°C, which is not considered in the CPFEM model. This phenomenon is associated with the thermally powered mobility of irradiation defects and has been previously discussed in §4.2.3.1.

Apparently, analyzing radiation-induced hardening as the difference in hardness in the irradiated and reference states seems to be the most meaningful way to use this approach. So that:

$$H_{irr} - H_{ref} = H_{dpa} \tag{4.2}$$

where H_{dpa} is the radiation-induced hardening, and H_{irr} and H_{ref} are the absolute hardness values for both states of the material. But of course, the absolute computational values must be in an acceptable comparison with their experimental analogues. If one assumes that the distortions that come from the elastic regime and the simplified hardness calculations (in simulations) or the indentation size effect and the strain rate inconsistency (in experiments) are not changed after irradiation, then the usage of H_{dpa} allows one to subtract these artifacts. Apparently, this is not completely true for the ISE, which may change because of the irradiated microstructure. Nevertheless, the H_{dpa} difference anyway allows one to minimize the ISE

undesirable contribution by considering just that part of the ISE that has been changed due to irradiation. So, in the case of simulations:

$$Sim: \begin{cases} H_0 + H_{dpa} + \omega_{el} + \omega_S = H_{irr} \\ H_0 + \omega_{el} + \omega_S = H_{ref} \end{cases} \quad (4.3)$$

where ω_{el} and ω_S are the absolute errors coming from the elasticity and simplified hardness calculations respectively, H_0 is the bulk material hardness. The same assumption for the experimental data gives:

$$Exp: \begin{cases} H_0 + H_{ISE}^{irr} + H_{dpa} = H_{irr} \\ H_0 + H_{ISE}^{ref} = H_{ref} \end{cases} \quad (4.4)$$

where H_{ISE}^{irr} and H_{ISE}^{ref} are contributions to hardness from the ISE. Substitutions give:

$$Sim: H_{dpa} = H_{dpa} \quad (4.5)$$

$$Exp: H_{ISE}^{irr} - H_{ISE}^{ref} + H_{dpa} = H_{dpa} \quad (4.6)$$

So, the $H_{ISE}^{irr} - H_{ISE}^{ref}$ is the only term which brings an uncertainty in such a comparison. However, $H_{ISE}^{irr} - H_{ISE}^{ref} < H_{ISE}^{ref}$ in any case, which means that it suits better for the comparison than the use of absolute values. Also, as a result of the fine microstructure of steel, the ISE is low and, therefore, does not create a big fluence on the results. Eventually, the ISE decreases with the indentation depth, so only shallow depths measurements are affected. Uncertainties due to an inconsistent strain rate between two different sets of indentation testing parameters (force, depth, etc.) will also be neglected when working with H_{dpa}. Once again, using H_{dpa} in this analysis is acceptable only in the case where the absolute computational values are in the close range with the experimental ones.

Additionally, the continuous stiffness measurement method can be used to experimentally obtain hardness-depth profiles, where the ISE can be analyzed by deduction of the Nix and Gao parameters and their change after irradiation [58] [113] [114] [115]. This would allow one to separate the contribution from the ISE and minimize the calculation error even more, however, the experimental campaign presented in this work did not include the application of the CSM method.

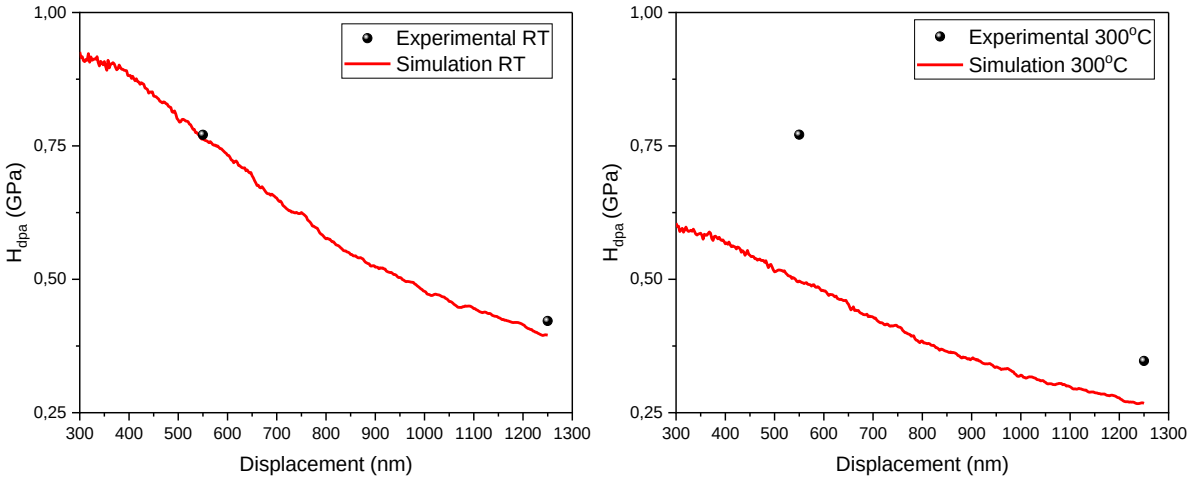

Figure 75. Difference between hardness of the reference and the irradiated material (radiation-induced hardening): a) room temperature; b) 300°C. Experimental values reach ~500 nm with 20 mN and ~1250 nm with 100 mN.

Figure 75 shows the comparison of the magnitudes of radiation-induced hardening obtained experimentally and by applying the numerical method presented. One can see a very accurate prediction of the irradiation hardening in the case of room temperature. Taking into account that the inputs for the CPFEM simulations are based on the tensile tests of neutron-irradiated material, it points to an interconnection between ion and neutron damage impact.

At 300°C, the situation is not that accurate, considering that extra hardening has occurred. It is worth noting that both experimental and simulation data tend to decrease with depth, while having different slopes. They must intersect at some point, thus reaching a mode in which radiation-induced damage does not contribute anymore to hardness. If the presented computational analysis as well as the experiments are correct, and only their hardening correlation factors are wrong, this intersection must occur at approximately $H_{dpa} = 0$ GPa and $h \approx 1800$ nm where the ion damage is no longer present according to Figure 48. A quick linear fit presented in Figure 76 confirms this assumption.

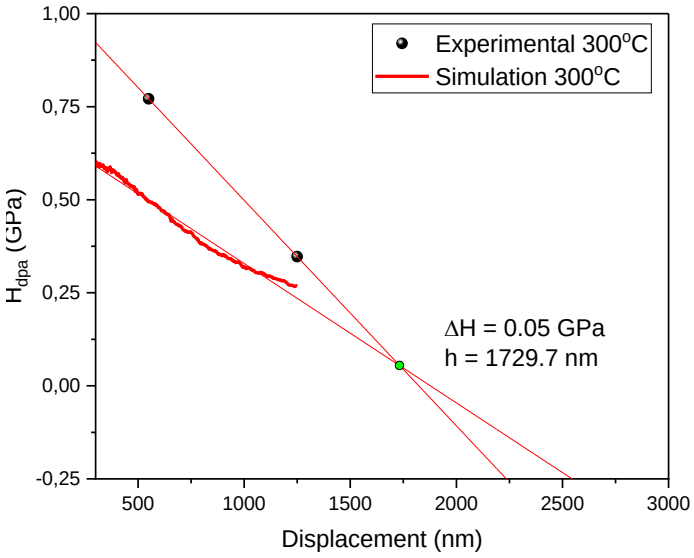

Figure 76. Intersection point of experimental and simulated H_{dpa} at 300°C.

In reality, a complete fade of irradiation hardening is impossible, as the Berkovich indenter has the pyramidal shape and, therefore, the evolving contact area. The ion-damaged subsurface will be constantly in contact with the base layers of the pyramid, although its contribution will be gradually decreasing.

4.4.3 Analysis of the FEM maps

As before, the FEM maps with the distributions and magnitudes of important quantities associated with mechanical deformation are analyzed. The 300°C cases are not provided, as the reproducibility of the experimental data is not achieved realistically.

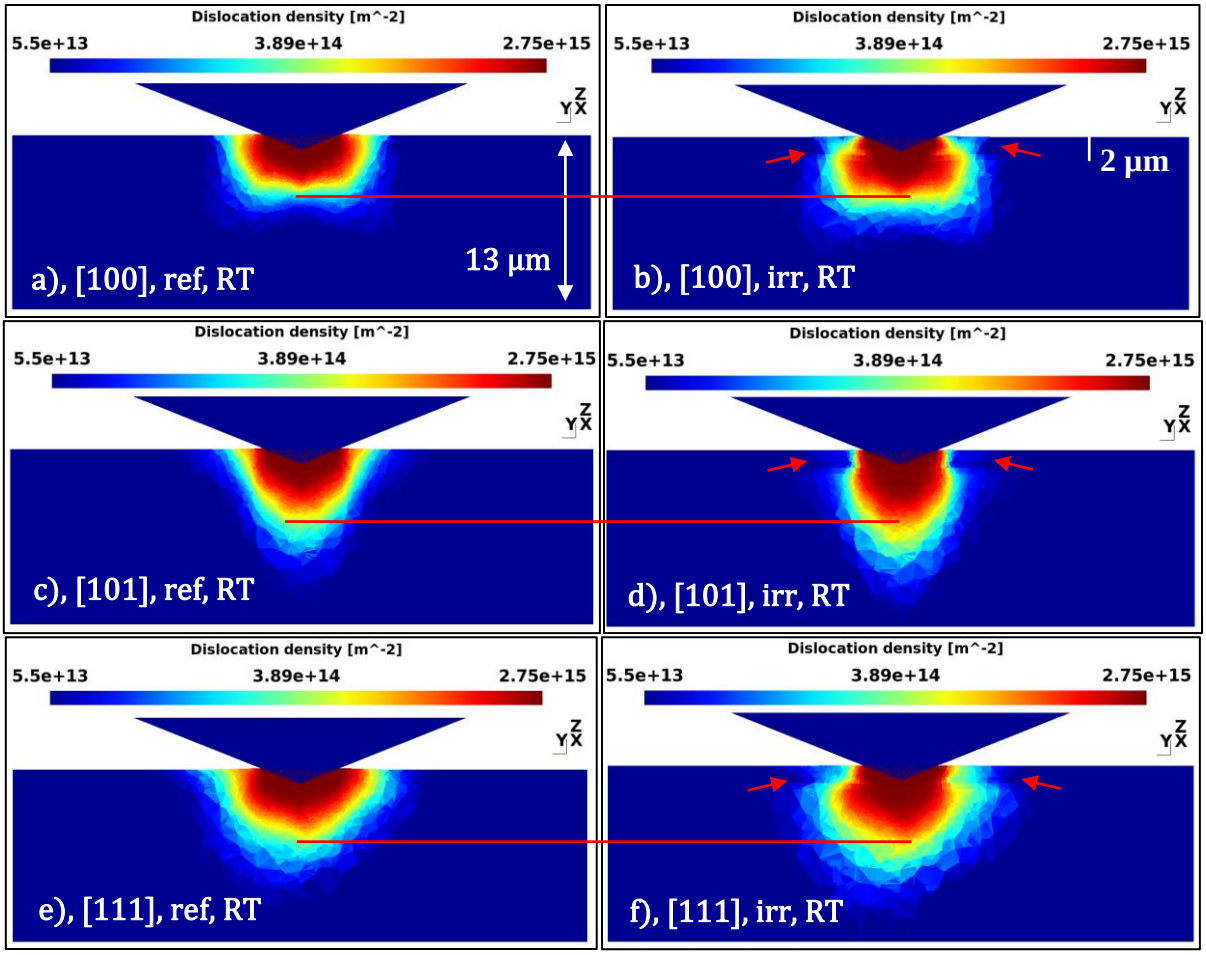

Figure 77. Dislocation density distributions (log scale) distributions at h_{max} and room temperature for different surface orientations from FEA: a) [100], reference; b) [100], irradiated; c) [101], reference; d) [101], irradiated (red arrows show suppression of the dislocation density distribution); e) [111], reference; f) [111], irradiated. All figures are taken at h = 1250 nm.

Distributions of dislocation densities are given in Figure 77, scalebars for the specimen height and irradiated subsurface can be seen in Figure 77(a). The first thing observed is that the evolution of dislocation density is suppressed in the area where irradiation hardening is present. This shrinks the dislocation forest, making its distribution more concentrated around the indenter tip (indicated by the red arrows in Figure 77(b, d, f)). Further observation is that the dislocation density evolution propagates deeper into the specimen, once passing through the

hardened subsurface. The parallel red lines between each pair of pictures show that the magnitudes of the reference material are behind the "irradiated" ones. It seems that the quantity is accumulating in the irradiated zone until the stress required to pass it through is reached. Then its evolution concentrates in the less hardened zone (bulk), whereas in the case of the reference material it can propagate along the surface, reducing its own ability to propagate into bulk. This effect must be accounted for when, for example, FIB lamellas of the irradiated subsurface are made for further examination by TEM. If a composite picture of the deformed area is required, one must focus on its depth rather than its width. As before, favorable directions for the quantity propagation are associated with the slip systems.

By analyzing accumulated slip maps, one can see the same effect. As in Figure 45, the plastic zones are presented as all elements that have undergone any value of plastic deformation as accumulated slip (the values lower than 0.0001 would not extend the plastic hemisphere further). The extension of the plastic zone is suppressed on the sides of the irradiated subsurface, thus accumulating deformation deeper in the specimen. This makes the plastic zone radius to indentation depth ratio higher in the case of the irradiated material. An exemplary comparison is given in Figure 78 for the [100] surface orientation case.

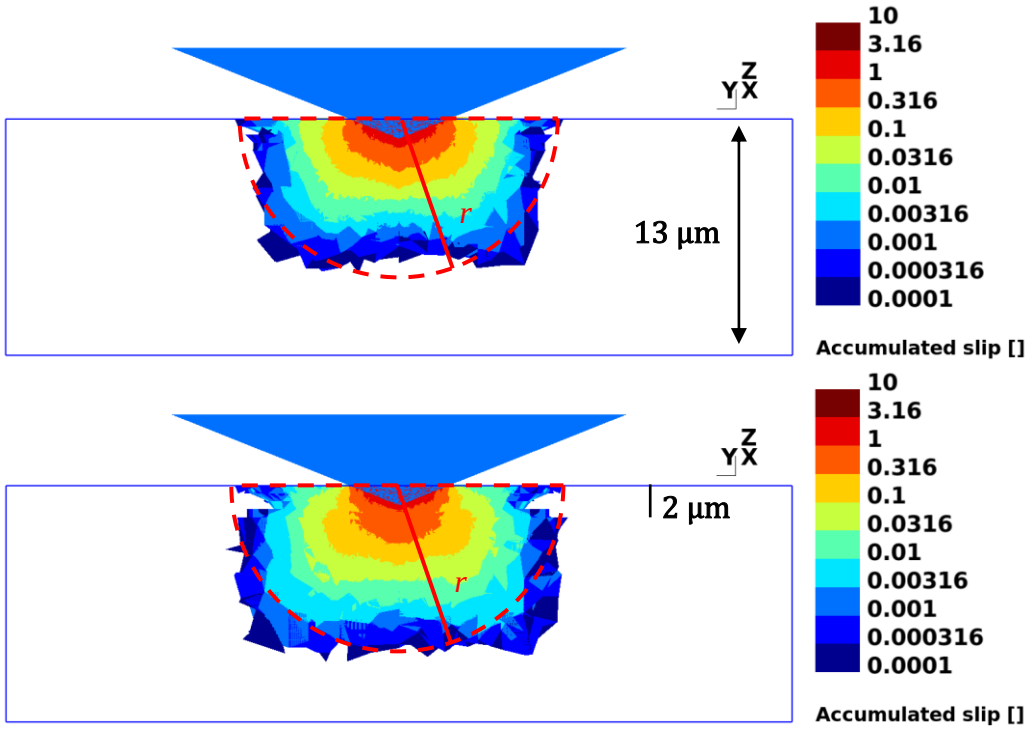

Figure 78. Accumulated slip (log scale) at h_{max} and room temperature from FEA: a) reference, b) irradiated. All figures are taken at h = 1250 nm.

Figure 78 shows that the resulting plastic hemispheres are not perfectly hemispherical, so the determination of the plastic zone can be arguable. However, if the same rule is applied to both materials to determine the plastic zone, the irradiated case will always be larger than the reference.

The plastic zone radius to indentation depth ratios are calculated and presented in Table 11.

Surface orientation	*r/h*, Reference	*r/h*, Irradiated
[100]	7.5	9.0
[101]	10.6	12.3
[111]	9.6	11.3
Averaged	9.23 ± 1.41	10.86 ± 1.65

Table 11. The plastic zone radius to indentation depth ratios for both states of the material.

Despite the enhanced extension of the plastic zone in the irradiated material, the maximal values of the accumulated slip are higher in the reference case. Once averaged across the three orientations, they are equal to 3.6 ± 0.79 in the irradiated case and to 4.06±0.79 in the reference case. This fact justifies the intuitive assumption that the hardened subsurface must reduce the degree of deformation. As expected, these zones are concentrated closely around the indenter tip.

It can be expected that the extension of deformation on lower indentation depths in the irradiated material can be suppressed not only along the surface but also in depth. This assumption was verified by studying the plastic zones at intermediate indentation depths of 250, 500, 750 and 1000 nanometers. However, no suppression was found and in each case the plastic zone of the irradiated material is larger than the reference, whereas the highest deformation level is vice versa.

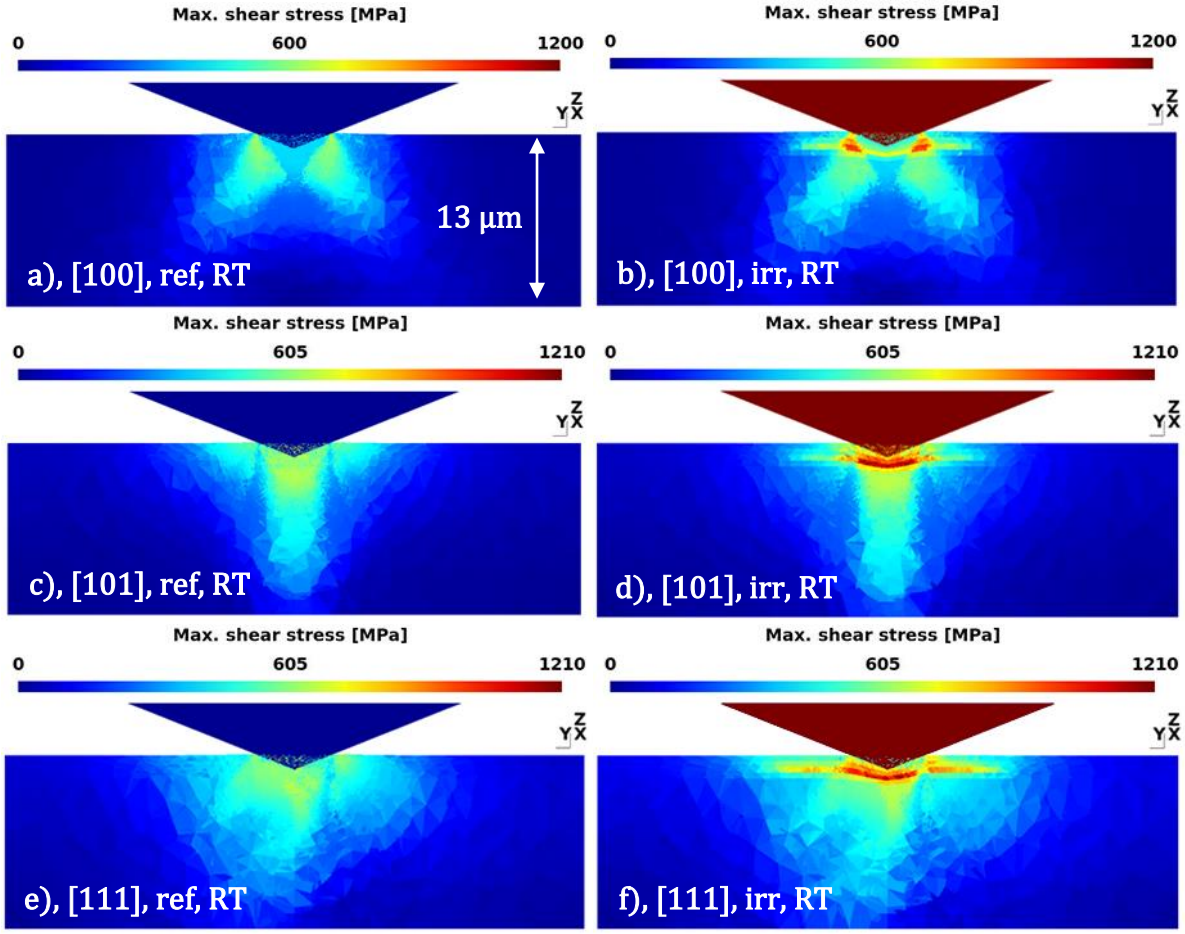

Figure 79. Maximum shear stress at h_{max} and room temperature for different surface orientations from FEA: a) [100], reference; b) [100], irradiated; c) [101], reference; d) [101], irradiated; e) [111], reference; f) [111], irradiated. All figures are taken at h = 1250 nm.

In Figure 79 the maximum shear stress profiles are presented. As expected, the highest stress concentrations are found in the hardened layers. The magnitudes reach approximately 600 MPa in natural stress distributions, and at least 1200 MPa on the subsurface, so it increases around twice. Also, as before, the propagation of this quantity is a little deeper than in the reference material. Favorable directions are aligned with the slip systems.

4.5 Summary & conclusions

As before, the conclusions from the presented chapter will be given as two different sections: physical conclusions, describing the observed physical phenomena; and technical conclusions, gathering the lessons learned from the establishment and application of the methodology. Conclusions 1, 2, 3, 5, 6, 9, 10, 11 are related to the validational nanoindentation experiments done on ion-irradiated Eurofer97. Conclusions 5, 7, 8, 9, 10 cover the findings regarding the CPFEM nanoindentation model. Conclusions 4, 7 are about the tensile tests used for the model calibration.

4.5.1 Physical conclusions

1. The nanoindentation experimental campaign done on the reference and ion-irradiated Eurofer97 in a range of temperatures has shown the presence of irradiation hardening. The tests have been carried out at two force levels: 20 mN and 100 mN, to explore an effect of the spatial distribution of the irradiation damage. Moreover, as stiffness could not be measured correctly, the elastic modulus correction technique was applied. It is found that the irradiation hardening is equal to ~0.77 GPa at ~500 nm (20 mN) and ~0.42 GPa at ~1200 nm (100 mN) at room temperature, and ~0.815 GPa at ~500 nm (20 mN) and ~0.34 GPa at ~1200 nm (100 mN) at 300°C. Experiments performed at 500°C have not shown any irradiation hardening due to damage annealing.

2. Depending on the indentation depth reached and used to determine the material hardness, the magnitude of the irradiation hardening is different and tends to decrease at the higher depth. The reason for this is the smaller plastic zone created by the indenter tip at shallow depths, so it predominantly stays within the irradiated region, and therefore is more affected by the ion damage. As the indentation depth increases, the coverage of the damaged area by the plastic zone reduces, so the material response approaches to the bulk unaffected by ions. This observation is known and has been experimentally confirmed rather than concluded.

3. Nanoindentation tests done at 300°C have shown a magnitude of irradiation hardening very similar to that at room temperature. This behavior can be explained by either the thermally enhanced defect mobility or uncertain post-processing of the force-displacement curves, caused by the wrong set of data acquisition parameters. However, the mechanical response seems to be correct in both experimental and computational cases, as the hardness-depth profiles strive to intersect in the point where the ion damage fades, what has been confirmed by linear fitting.

4. On the basis of the literature, tensile experimental measurements, and fitting, the obtained constitutive parameters (i.e. activation energy) are in the reasonable range considering the underlying physical processes. The dislocation-dislocation interaction factor and Kocks-Mecking parameter are the only parameters changing with the temperature and this behavior is in accordance with the information available in the literature. The initial dislocation density was reduced (from $1.5 \cdot 10^{14}$ to $5.5 \cdot 10^{13}$ m^{-2}) which can be explained by the fact that only a fraction represents mobile dislocations of the whole dislocation forest.

5. Nanoindentation distribution patterns of dislocation density, accumulated slip, and equivalent stress in the irradiated material are being suppressed along the surface at the irradiated region. Their depth propagation, however, is not suppressed and is even more enhanced than in the reference material. On the other hand, the maximum accumulated slip values are higher in the reference material (~3.6 versus ~4.06), which means that the deformation scales are affected by the irradiation-hardened layers. Irradiation defects accumulate stress on the hardened subsurface, as it reaches the value of ~1200 MPa compared to the bulk value of ~600 MPa. The extension of the plastic zone slightly overestimates the literature values in the irradiated case (~10.86) and remains within the range in the reference case (~9.23).

6. SEM analysis of the nanoindentation imprints on Eurofer97 in the irradiated and reference states has shown that piling-up is accompanied by microfracturing at room temperature and 300°C. At 500°C, as well as in pure iron at any temperature, microfracturing has not been observed. It is associated with the lower plastic deformation capacity of Eurofer97 compared to iron, which cracks the outcoming volumes of material instead of their continuous deformation.

4.5.2 Technical/Methodological conclusions

7. The material laws responsible for the mechanical response on the ion-irradiated subsurface were obtained as a combination of neutron-irradiated tensile data (yield stresses) and non-irradiated stress-strain curves. This allows one to deduce a set of magnitudes of the irradiation hardening (i.e. increase of the yield stress) with respect to different damage doses, while working just with one irradiated specimen (one irradiation damage-depth profile). Moreover, the proposed semi-empirical methodology allows complex investigations such as TEM/FIB of the irradiated zone to be avoided, as the key-steps are not associated with microstructural features or defects and are based on anisotropic material response, but at the same (micro/nano) scale. However, additional assessment of the model efficiency is required with the complementary analysis done with more precise high temperature tests and different irradiation parameters.

8. The ability of the presented novel approach to represent the ion-irradiated material has been shown to be effective by closely reproducing experimental data at room temperature. However, the effect of elasticity in the initial stages of the nanoindentation process has a significant impact on the calculated lower depths (200 – 600 nm) hardness values when modeled with CPFEM. Moreover, this impact is strongly dependent on the element size; thus, the mesh convergence analysis must be performed to neglect its contribution. In the presented work, the mesh was fined to a sufficient, but not perfect size, due to the CPU power limitations of the workstation used for calculations. In the future, the best mesh can be applied by using a supercomputer. It must be added that the simulated material response is not affected after the depths of 400 nm in this particular case. Therefore, no hardness or any other quantities are distorted after this value.

9. The agreement of the experimental and simulated force-displacement curves is higher than in the case of the pure iron product, which points to the lower indentation size effect.

10. When analyzing and comparing the hardness obtained both computationally and experimentally, it is more accurate and meaningful to use their differences ΔH, rather than the absolute values. It allows to subtract (i.e. neglect) any experimental and modeling artifacts, which are not associated with the effect of irradiation (assuming them to be equally inherent for each irradiated-reference couple of curves). However, the usage of H_{dpa} is only justified in the case when the absolute values are also in an acceptable comparable range.

11. The thinned and elongated dislocation density distribution shapes in the irradiated material should be considered if a composite picture of dislocation density of the

indented zone is being formed for inspection using TEM and FIB. It is recommended to focus on investigating the depth of the plastic deformation extension, rather than the widt

Chapter 5. Conclusions & outlook

In this chapter, the discussion of the further improvements and general applicability of the presented research will take place. Summarized conclusions from the entire manuscript will be presented. It will also include other potential developments related to the main subject of the study, which have been studied during the research period.

5.1 Summary & conclusions

The presented research has demonstrated an attempt to solve the problem of high temperature characterization of mechanical properties of irradiated metallic materials for nuclear applications. The focus has been set on the phenomenon of irradiation hardening, which is in the case of neutron irradiation being a long and expensive process to achieve. A characterization protocol is proposed, which seeks to avoid neutron irradiation for research purposes, substituting it with a safer and faster irradiation with ions. The protocol is based on a set of research methods built around nanoindentation experiments, tensile testing, scanning and transmission electron microscopies, electron backscattered diffraction technique, and crystal plasticity finite element modeling. It has been established and experimentally validated using a pure iron product and Eurofer97 reduced activation ferritic/martensitic steel. Conclusions are given after working with each material.

5.1.1 Pure iron

In this contribution, the CP model in combination with FEM solver has been applied to simulate the nanoindentation process in BCC Fe in the range of temperatures from room temperature up to 500°C. The constitutive laws for the CPFEM model were derived using the tensile deformation data and experimentally characterized microstructure (SEM-EBSD and TEM data) of the material. Thermal activation and strain rate dependence of the plastic slip have been introduced through the equations and parameterized by adopting the open literature data for α-iron. After nanoindentation, the dimensions of the imprints and profiles of the dislocation density around the indents were experimentally measured by means of scanning and transmission electron microscopy to compare with the predictions of the CPFEM model. It is shown that the material behavior is properly caught by CPFEM setup, which is proven not only by the outcoming load-displacement curves but also by the stress distribution maps, accumulated slip distribution maps, associated dislocation density fields, and the shape of final imprints represent the microstructural features in a good agreement with the results obtained using TEM and SEM and correlate well with predictions done in other studies. Hardness calculations are also in good agreement with experimental values if obtained just by using the formula for perfect indenter, which is applied in the present simulations. Despite the good match between the experiments and the CPFEM approach for the maximum applied force in the nanoindentation force-displacement curves, the initial force values appear to be significantly different (up to 60%). The reason for that can be a completely neglected tip imperfection in the model or a set of experimental artifacts. Another good explanation can be the fact that the strain gradient theory is not introduced in the present model, so it affects the output curve at shallow depths, where the size effect is present, and therefore affects the overall evolution of the force. It is possible to introduce the mentioned models into CPFEM; however, it would require consideration of additional degrees of freedom, hence a complicated implementation and higher computational demand. To conclude, the set of the constitutive parameters defined from the tensile experiments is precise enough to reproduce true stress-strain curves of the studied

material and in combination with the presented CPFEM nanoindentation setup can also reproduce the nanoindentation force-displacement curves of the same material and testing conditions. The mathematical functional and the CPFEM model open the way to incorporate the effect coming from the irradiation defects (such as dislocation loops and voids), given that the thermally activated dislocation-defect interaction can be parameterized on the basis on the available theoretical and atomistic modeling studies. Therefore, the presented computational approach is a prospective tool to investigate the mechanical response of the material to compressive deformation under nanoindentation experimental conditions. On the one hand, the approach adequately grasps the heterogeneity of the plastic deformation under the indenter, and, on the other hand, it correctly transfers the constitutive law derived from the tensile tests. Importantly, the implemented computational approach remains rather flexible to introduce other sources that alternate plastic deformation, such as irradiation defects or strain rate sensitivity. In practice, this part is the probatory step towards the development of the CPFEM model which could treat the heterogeneous microstructure generated by the ion irradiation damage and thereby help to retrieve the local property of the material. To complete this model for ion-irradiated steels it is updated and validated to treat non-irradiated F/M steel (to include the response of the martensitic microstructure) and finally to treat ion-irradiated F/M steel.

5.1.2 Eurofer97

This part accumulates the results of the application of the CP model in combination with the FEM solver to simulate the nanoindentation process in Eurofer97 RAFM steel in reference and ion-irradiated states and in the range of temperatures from room temperature to 300°C. The constitutive laws for the CPFEM model were derived using the tensile deformation data and experimentally characterized microstructure (SEM-EBSD and TEM data) of that material. Thermal activation and strain rate dependence of the plastic slip have been introduced through the equations and parameterized by adopting the open literature data for α-iron/BCC steel. It is shown that the material behavior is properly caught by the CPFEM setup, which is proven by the realistic reproduction of the tensile true and engineering stress-strain curves, nanoindentation force-displacement curves, and hardness calculations. The latter were calculated by using simplified formula, however, still giving appropriate values.

A novel approach to simulate ion-irradiated material has been introduced. This approach presumes the division of the specimen subsurface into several layers, each assigned with a material law representing a certain magnitude of the irradiation hardening typical for the averaged dpa damage dose in that layer. The magnitudes are obtained from the tensile tests on neutron-irradiated Eurofer97. Experimental validation data for the ion-irradiated material have been obtained by performing ion irradiation of the Eurofer97 specimens and their subsequent nanoindentation testing at room temperature and 300°C. The computational CPFEM analysis has shown high reproducibility of the experimental data at room temperature. The magnitudes of irradiation hardening throughout the indentation depth have been accurately reproduced, with an error not exceeding 9%. Considering the path from neutron irradiation and macrotensile deformations to ion irradiation and microcompressive deformation, this approach seems to be highly efficient and points to a good interconnection between the mentioned factors. It is important to emphasize that the correlation between radiation-induced hardenings in a broad dpa damage range in ion and neutron-irradiated material was obtained by using just one sample exposed to the ion irradiation. The 300°C experimental data have shown excessive hardening and therefore have not been adequately computationally reproduced by the model based on only thermal activation. The 500°C experimental data have not shown any irradiation hardening due to the damage annealing and therefore have not been used for the computational analysis.

The obtained dislocation density, accumulated slip, and shear stress maps have been analyzed. In each case, the irradiated material shows the suppression of the plastic deformation along the hardened sub-surface; instead, the deformation is propagating into depth. This propagation appears to be deeper than in the reference material, which does not confirm the intuitive assumption of suppression of stress and strain distributions within the material. However, this assumption is partly justified by the magnitudes of accumulated slip deformation, which are significantly higher in the reference material. As expected, stress accumulates on the hardened layers and becomes approximately double the amount in the bulk. A practical conclusion can be made from the dislocation density distribution profiles of the irradiated material: If a composite picture of dislocation density of the indented zone is being formed for inspection using TEM and FIB, one must focus less on the width of the picture, but more on its depth.

Hence, the presented computational approach is a prospective method to investigate the mechanical response of the material after ion irradiation to compressive deformation under nanoindentation experimental conditions, and to predict neutron damage-based hardenings if a fitting procedure to find the correlation factors will be established.

5.2 Technical outlook

Some work has been done on other ideas towards improvement of the presented CPFEM model. Two main developments will be covered: a model of polycrystalline imitating a specimen made of a variety of grains created by Voronoi tessellation; and the opposite approach of fitting the irradiation hardening levels not by using the neutron-irradiated data but for predicting it.

5.2.1 Strain gradient crystal plasticity

Eventually, it was demonstrated in Appendix 1 that polycrystal geometry has an interesting potential in simulations of nanoindentation process, especially when the grain size levels are comparable to the indentation depths or extension of the plastic zones generated by the indenter tip. However, the absence of strain gradient theory makes its usage unworthy. Even if the distribution of quantities responsible for the deformation process is affected by adjacent grains, this process represents the minimum of the underlying physical processes. Therefore, the implementation of strain gradient theory is recommended in the future, which will also positively reflect the presence of the indentation size effect. Then the presented development can be additionally improved by using 3D Voronoi tessellation, geometrical introduction of microstructural features specific for steels (laths, blocks, PAGs), meaningful grain misorientations with respect to EBSD measurements, etc. The difficulty with strain gradient formulation is the requirement for higher-order continua in finite elements, which are only C0 in nature. This usually requires considering other degrees of freedom than displacement alone.

5.2.2 Predicting the neutron damage

When nanoindentation analysis of ion-irradiated materials is discussed, the real interest and ultimate goal is to use it to predict the effect of neutron damage. The presented research establishes the opposite procedure: when a knowledge about the impact of neutron damage allows the performance of an ion-irradiated material to be reproduced. This allows to confirm the validity of the approach, but on the other hand, it cannot be applied practically (there is no

sense to irradiate material with neutrons to predict the ion damage). A reversed method is crucial to make this method useful in real applications.

However, originally the presented method was developed based on its applicability in the "proper" direction. The input material laws were fit to have the macrotensile yield stresses appropriate for the replication of nanoindentation experimental data done on the ion-irradiated material. When the average damage dose on each layer is known from SRIM as shown in Figure 67, it is possible to roughly estimate the corresponding irradiation hardening. Basically, the direct procedure, i.e. calibrating the material model from nanoindentation tests performed on ion-irradiated material, which can in turn be used to predict macroscale response of neutron-irradiated material, includes several steps: estimation of the modified "irradiated" material laws with respect to damage doses, CPFEM simulation of the nanoindentation process, comparison with the experimental data, corrections if needed, another cycle. Several cycles had been made before a good match was obtained, as shown in Figure 80.

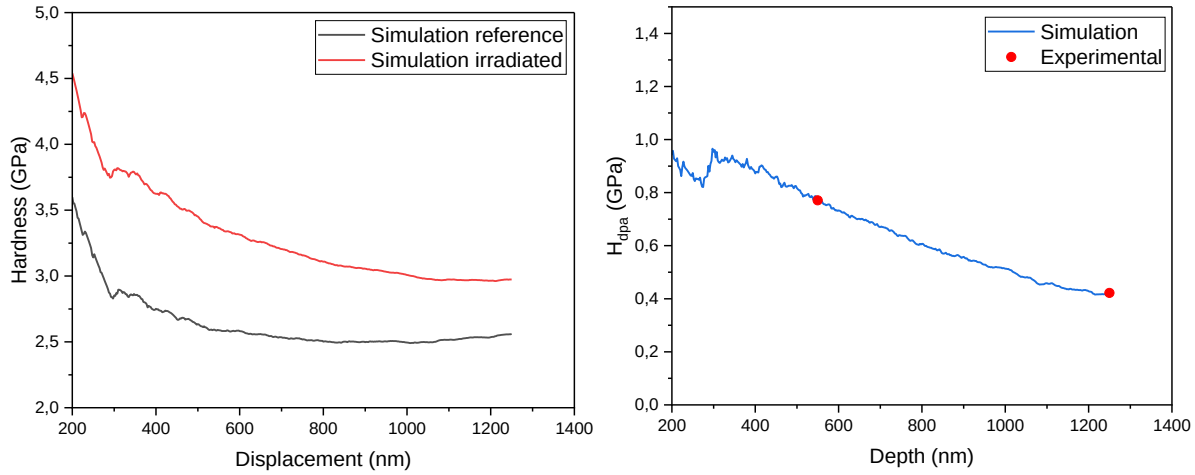

Figure 80. a) Hardness-depth profiles from CPFEM; b) CPFEM H_{dpa} (blue) compared to the experiments (red).

It is important to note that the results from Figure 80 were obtained before the mesh analysis and development was complete. Therefore, a more sensitive mesh was used similar to Mesh #2 in Figure 72, also with an insufficient spherical refinement radius. The latter leads to the growth of the element size before the simulated indenter reaches the maximum depth. Consequently, it distorts the force output and affects hardness calculations, which can be seen in Figure 80(a) as an unexpected slight hardness increase on the reference curve after 1000 nm depth. Nevertheless, it must affect the irradiated curve as well, so their difference will neglect this undesired effect according to the Eq. (4.3) and (4.5).

Such a fitting can provide a good replication of the yield stresses of the neutron-irradiated material [106], eventually used to confirm the validity of this approach.

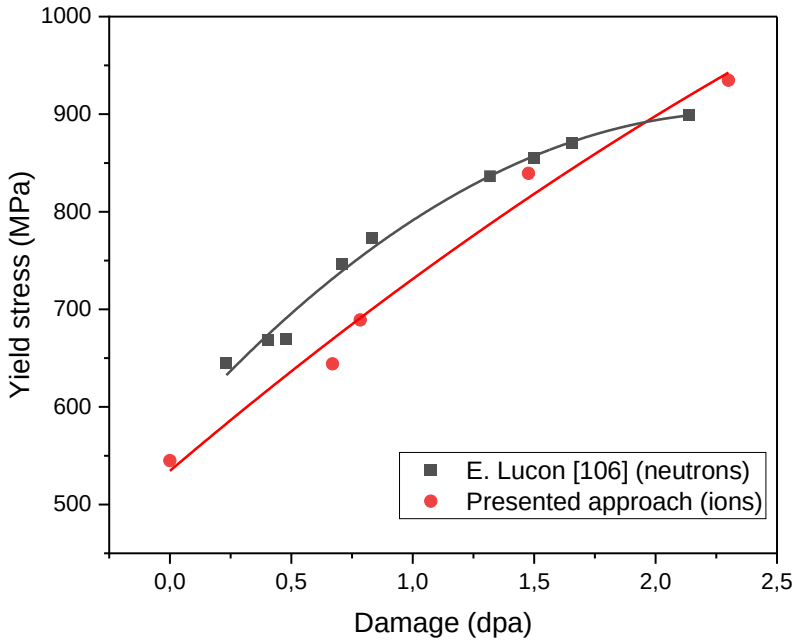

Figure 81. Experimental yield stresses of neutron-irradiated Eurofer97 (black); yield stresses obtained using the presented approach (red).

Figure 81 shows the comparison of yield stresses obtained experimentally on the neutron-irradiated material and using the presented approach applied on the ion-irradiated material. The differences are in the range from ~2% (19 MPa) to ~16% (102 MPa), which is a reasonable mismatch considering that manual fitting was used.

However, manual fitting of four closely related parameters (hardness of each layer) is not an efficient procedure. This process requires a computational algorithm, which will combine several aspects, such as: fitting of the material laws, transferring them into CPFEM simulations, performing these simulations, and simultaneously analyzing the output to be in match with the experimental data; making corrections if the output is outside a certain tolerance, and following the distributions of the damage doses. Development of such an algorithm would require additional efforts; thus, to perform this research in reasonable time ranges, the reversed approach has been realized (from neutrons to ions).

5.3 The scope of future studies

The scope of future studies and improvements will be given in this subsection. During the preparation of this manuscript, an application for the POLONEZ BIS 3 research grant [116] was submitted. The POLONEZ BIS is a possibility to carry out a 24-month research in a variety of research institutions in Poland. This grant is co-funded by the European Commission and the Polish National Science Centre under the Marie Skłodowska-Curie COFUND grant. The proposed project is fully based on the presented research and is a clear continuation of this Ph.D. project. The proposed within the POLONEZ BIS project has also been recommended for funding allowed to be performed at the NOMATEN Centre of Excellence associated with the National Centre for Nuclear Research in Warsaw.

In the new project, it is proposed to extend the presented nanoindentation experimentally computational analysis of ion-irradiated materials with respect to the new doses and temperatures. A set of Eurofer97 specimens has already been irradiated at HZDR to 1 and 5 dpa at 300°C, and 3 dpa is planned in the future. High temperature nanoindentation will be

performed at room temperature, 100°C, 200°C, and 300°C, thus giving a better understanding of the thermal impact on the behavior of the irradiation defects. In addition, the CSM method will be applied, so that more experimental data points will be available. These actions may prove the stability, predictivity, and further potential of the approach, as well as confirm the possibility of applying it to other metallic materials.

Additionally, the idea is to establish a self-sufficient approach to estimate the irradiation hardening caused by neutrons, while dealing only with ion-irradiated specimens. The method is based on nanoindentation tests and their CPFEM simulations (as presented in the given manuscript) together with complementary analysis to minimize the negative impact of different artifacts, such as indentation size effect, specimen compliance and roughness, indentation pile-ups, etc. It is planned to perform a deep study of microstructural evolution with respect to the magnitude of irradiation and subsequent mechanical response. By using FIB to extract the subsurface regions of the indented areas and inspect them using SEM/TEM techniques it will be possible to analyze the density and distribution of the radiation-induced defects, thus supporting the parameterization of the (advanced) Nix and Gao ISE models, as well as to compare the investigated microstructural features with molecular dynamics calculations. Furthermore, the indentation pile-ups will be investigated with AFM to estimate their impact on the measured stiffness, i.e. hardness, and perform the stiffness corrections to minimize the measuring error. The host institution provides access to all the mentioned crucial setups (metallography laboratory, SEM/EBSD, FIB, TEM, and AFM), as well as to the high temperature nanoindentation testing bench, which unties the opportunity to perform a statistical study on the specimen preparation process, essential to standardize a procedure, where the impact of the surface roughness and specimen dimensions will be lowered to the minimum. Most importantly, the listed activities will be performed in the same lab and on the same specimens, thus establishing complete control of the research team in the multidisciplinary investigation process.

Another important moment is that the CPFEM model is planned to be extended by introducing strain gradient theory and its parameterization, including accordance with FIB/TEM investigations of the subsurface areas before and after irradiation. The reverse approach of fitting the H_{dpa} to the nanoindentation response and thus obtaining the radiation-affected material laws is to be established.

Successful implementation of the project will result in the development of an accumulative and proven technique allowing relatively quick, accurate, and safe measurement of the impact of ion irradiation damage on the plastic properties such as hardness and yield stress of the RAFM steel Eurofer97 in a range of temperatures and with the lowest uncertainty, which can be consequently applied to other metallic materials by repeating validation steps to be established during the project. Moreover, the issue of interconnection between microscale and macroscale will contribute to the multiscale modeling approach applied to radiation effects in F/M alloys. The outcomes of this technique are to be compared with the available experimental data done on neutron irradiated material, to demonstrate its transferability and applicability. This research may serve the nuclear material sciences community as a characterization tool for more paced delivery of new research data done on structural nuclear materials after irradiation and consequently will accelerate our joint efforts on the way to a more stable, clean, and sustainable energy source for humanity.

Bibliography

[1] J. Ongena, "Fusion: a true challenge for an enormous reward," *EPJ Web of Conferences,* vol. 189, 2018.

[2] S. Konishi, "Functional materials for breeding blankets - status and developments," *Nuclear Fusion,* vol. 57, 2017.

[3] L. Giancarli, M. Abdou, D. Campbell, V. Chuyanov, M. Ahn, M. Enoeda, C. Pan, Y. Poitevin, E. R. Kumar, I. Ricapito, Y. Strebkov, S. Suzuki, P. Wong and M. Zmitko, "Overview of the ITER TBM Program," *Fusion Engineering and Design,* vol. 87, no. 5-6, pp. 395-402, 2012.

[4] Y. Poitevin, I. Ricapito, M. Zmitko, F. Tavassoli, N. Thomas, G. D. Dinechin, P. Bucci, J. Rey, A. Ibarra, D. Panayotov, L. Giancarli, P. Calderoni, J. Galabert, J. Vallory and A. Aiello, "Progresses and challenges in supporting activities toward a license to operate European TBM systems in ITER," *Fusion Engineering and Design,* vol. 89, no. 7-8, pp. 1113-1118, 2014.

[5] G. Kinchin and R. Pease, "The Displacement of Atoms in Solids by Radiation," *Reports on Progress in Physics,* vol. 18, 1955.

[6] G. Was, Fundamentals of Radiation Materials Science: Metals and Alloys, Springer, 2016.

[7] D. Hull and D. Bacon, "Movement of Dislocations," in *Introduction to Dislocations,* 2011, p. 55.

[8] R. Chaouadi, "Effect of irradiation-induced plastic flow localization on ductile crack resistance behavior of a 9%Cr tempered martensitic steel," *Journal of Nuclear Materials,* vol. 372, no. 2-3, pp. 379-390, 2008.

[9] F. Garner, M. Hamilton, N. Panayotou and G. Johnson, "The microstructural origins of yield strength changes in aisi 316 during fission or fusion irradiation," *Journal of Nuclear Materials,* vol. 104, pp. 803-807, 1981.

[10] G. Odette and G. Lucas, "Recent progress in understanding reactor pressure vessel steel embrittlement," *Radiation Effects and Defects in Solids,* vol. 144, no. 1-4, pp. 189-231, 1997.

[11] E. Gaganidze and J. Aktaa, "Assessment of neutron irradiation effects on RAFM steels," *Fusion Engineering and Design,* vol. 88, no. 3, pp. 118-128, 2013.

[12] E. Wakai, S. Takaya, Y. Matsui, Y. Nagae, S. Kato, T. Suzudo, M. Yamaguchi, K. Aoto, S. Nogami, A. Hasegawa, H. Abe, K. Sato, T. Ishida, S. Makimura, P. G.

Hurh, K. Ammigan and D. J. Se, "Irradiation damages of structural materials under different irradiation environments," *Journal of Nuclear Materials,* vol. 543, 2021.

[13] V. Slugeň, S. Sojak, W. Egger, V. Krsjak, J. Veternikova and M. Petriska, "Radiation Damage of Reactor Pressure Vessel Steels Studied by Positron Annihilation Spectroscopy—A Review," *Metals,* vol. 10, 2020.

[14] S. Zinkle, P. Maziasz and R. Stoller, "Dose dependence of the microstructural evolution in neutron-irradiated austenitic stainless steel," *Journal of Nuclear Materials,* vol. 206, no. 2-3, pp. 266-286, 1993.

[15] A. Kohyama, Y. Kohno, K. Asakura, M. Yoshino, C. Namba and C. Eiholzer, "Irradiation creep of low-activation ferritic steels in FFTF/MOTA," *Journal of Nuclear Materials,* Vols. 212-215, pp. 751-754, 1994.

[16] P. Zheng, R. Chen, H. Liu, J. Chen, Z. Zhang, X. Liu and Y. Shen, "On the standards and practices for miniaturized tensile test – A review," *Fusion Engineering and Design,* vol. 161, 2020.

[17] G. Lucas, G. Odette, M. Sokolov, P. Spätig, T. Yamamoto and P. Jung, "Recent progress in small specimen test technology," *Journal of Nuclear Materials,* Vols. 307-311, 2002.

[18] P. Hosemann, "Small-scale mechanical testing on nuclear materials: bridging the experimental length-scale gap," *Scripta Materialia,* vol. 143, pp. 161-168, 2018.

[19] Z. S.J. and J. Busby, "Structural materials for fission & fusion energy," *Materials Today,* vol. 12, 2009.

[20] R. Lässer, N. Baluc, J.-L. Boutard, E. Diegele, S. Dudarev, M. Gasparotto, A. Möslang, R. Pippan, B. Riccardi and B. v. d. Schaaf, "Structural materials for DEMO: The EU development, strategy, testing and modelling," *Fusion Engineering and Design,* vol. 82, pp. 511-520, 2007.

[21] G. Was, "Challenges to the use of ion irradiation for emulating reactor irradiation," *Journal of Materials Reseach,* vol. 30, pp. 1158-1182, 2015.

[22] J. Ziegler, M. Ziegler and J. Biersack, "SRIM – The stopping and range of ions in matter," *Nuclear Instruments and Methods in Physics Research Section B,* no. 268, pp. 1818-1823, 2010.

[23] E. Aydogan, S. Maloy, O. Anderoglu, C. Sun, J. Gigax, L. Shao, F. Garner, I. Anderson and J. Lewandowski, "Effect of tube processing methods on microstructure, mechanical properties and irradiation response of 14YWT nanostructured ferritic alloys," *Acta Materialia,* vol. 134, pp. 116-127, 2017.

[24] R. Klueh and A. Nelson, "Ferritic steels for next-generation reactors," *Journal of Nuclear Materials,* vol. 371, pp. 37-52, 2007.

[25] B. Singh and J. Evans, "Significant differences in defect accumulation behaviour between fcc and bcc crystals under cascade damage conditions," *Journal of Nuclear Materials,* vol. 226, pp. 277-285, 1995.

[26] D. Terentyev, A. Puype, O. Kachko, W. V. Renterghem and J. Henry, "Development of RAFM steel for nuclear applications with reduced manganese, silicon and carbon content," *Nuclear Materials and Energy,* vol. 29, 2021.

[27] O. Kachko, A. Puype, D. Terentyev, G. Bonny, W. V. Renterghem and R. Petrov, "Development of RAFM steels for high temperature applications guided by thermodynamic modelling," *Nuclear Materials and Energy,* vol. 32, 2022.

[28] L. Tan, L. Snead and Y. Katoh, "Development of New Generation Reduced Activation Ferritic-Martensitic Steels for Advanced Fusion Reactors," *Journal of Nuclear Materials,* vol. 478, pp. 42-49, 2019.

[29] H. Tanigawa, E. Gaganidze, T. Hirose, M. Ando, S. Zinkle, R. Lindau and E. Diegele, "Development of benchmark reduced activation ferritic/martensitic steels for fusion energy applications," *Nuclear Fusion,* vol. 57, 2017.

[30] A. Möslang, E. Diegele, M. Klimiankou, R. Lässer, R. Lindau, E. Lucon, E. Materna-Morris, C. Petersen, R. Pippan, J. Rensman, M. Rieth, B. v. d. Schaaf, H.-C. Schneider and F. Tavassoli, "Towards reduced activation structural materials data for fusion DEMO reactors," *Nuclear Fusion,* vol. 45, 2005.

[31] E. Gaganidze, F. Gillemot, I. Szenthe, M. Gorley, M. Rieth and E. Diegele, "Development of EUROFER97 database and material property handbook," *Fusion Engineering and Design,* vol. 135, pp. 9-14, 2018.

[32] G. Federici, L. Boccaccini, F. Cismondi, M. Gasparotto, Y. Poitevin and I. Ricapito, "An overview of the EU breeding blanket design strategy as an integral part of the DEMO design effort," *Fusion Engineering and Design,* vol. 141, pp. 30-42, 2019.

[33] J. You, E. Visca, C. Bachmann, T. Barrett, F. Crescenzi, M. Fursdon, H. Greuner, D. Guilhem, P. Languille, M. Li, S. McIntosh, A. Müller, J. Reiser, M. Richou and M. Rieth, "European DEMO divertor target: Operational requirements and material-design interface," *Nuclear Materials and Energy,* vol. 9, pp. 171-176, 2016.

[34] M. Gorley, E. Diegele, E. Gaganidze, F. Gillemot, G. Pintsuk, F. Schoofs and I. Szenthe, "The EUROfusion materials property handbook for DEMO in-vessel components—Status and the challenge to improve confidence level for engineering data," *Fusion Engineering and Design,* vol. 158, 2020.

[35] D. Kramer, H. Huang, M. Kriese, J. Robach, J. Nelson, A. Wright, D. Bahr and G. W.W., "Yield Strength Predictions From the Plastic Zone Around Nanocontacts," *Acta Materialia,* vol. 47, no. 1, pp. 333-343, 1998.

[36] P. Hosemann, D. Kiener, Y. Wang and S. A. Maloy, "Issues to consider using nano indentation on shallow ion beam irradiated materials," *Journal of Nuclear Materials,* vol. 425, no. 1-3, pp. 136-139, 2012.

[37] M. Saleh, Z. Zaidi, C. Hurt, M. Ionescu, P. Munroe and D. Bhattacharyya, "Comparative study of two nanoindentation approaches for assessing mechanical properties of ion-irradiated stainless steel 316," *Metals,* vol. 8, p. 719, 2018.

[38] P. Lin, J. Nie and M. Liu, "Study on irradiation effect in stress-strain response with CPFEM during nano-indentation," *Nuclear Materials and Energy,* vol. 22, 2020.

[39] C. Deo, C. Tome, R. Lebensohn and S. Maloy, "Modeling and simulation of irradiation hardening in structural ferritic steels for advanced nuclear reactors," *Journal of Nuclear Materials,* vol. 377, pp. 136-140, 2008.

[40] X. Xiao, L. Chen, L. Yu and H. Duan, "Modelling nano-indentation of ion-irradiated FCC single crystals by strain-gradient crystal plasticity theory," *International Journal of Plasticity,* vol. 116, pp. 216-231, 2019.

[41] X. Xiao, D. Terentyev, A. Ruiz, A. Zinovev, A. Bakaev and E. Zhurkin, "High temperature nano-indentation of tungsten: modelling and experimental validation," *Materials Science and Engineering: A,* vol. 743, pp. 106-113, 2019.

[42] J. Nie, P. Lin, Y. Liu, H. Zhang and X. Wang, "Simulation of the irradiation effect on hardness of Chinese HTGR A508-3 steels with CPFEM," *Nuclear Engineering and Technology,* vol. 51, no. 8, pp. 1970-1977, 2019.

[43] J. Knapp, F. D.M., S. Myers, J. Barbour and T. Friedmann, "Finite-element modeling of nanoindentation," *Journal of Applied Physics,* vol. 85, pp. 1460-1474, 1999.

[44] P. Hosemann, C. Vieh, R. Greco, S. Kabra, J. Valdez, M. Cappiello and S. Maloy, "Nanoindentation on ion irradiated steels," *Journal of Nuclear Materials,* vol. 389, pp. 239-247, 2009.

[45] L. Veleva, P. Hähner, A. Dubinko, T. Khvan, D. Terentyev and A. Ruiz-Moreno, "Depth-Sensing Hardness Measurements to Probe Hardening Behaviour and Dynamic Strain Ageing Effects of Iron during Tensile Pre-Deformation," *Nanomaterials,* vol. 11, 2021.

[46] Y. Su, C. Zambaldi, D. Mercier, P. Eisenlohr, T. Bieler and M. Crimp, "Quantifying deformation processes near grain boundaries in α titanium using nanoindentation and crystal plasticity modeling," *International Journal of Plasticity,* vol. 86, pp. 170-186, 2016.

[47] G. Taylor, "Plastic strain in metals," *Journal of the Institute of Metals,* vol. 62, pp. 307-324, 1938.

[48] E. Marin and P. Dawson, "On modelling the elasto-viscoplastic response of metals using polycrystal plasticity," *Computer Methods in Applied Mechanics and Engineering,* vol. 165, no. 1-4, pp. 1-21, 1998.

[49] D. McDowell, "Connecting Lower and Higher Scales in Crystal Plasticity Modeling," *Handbook of Materials Modeling,* pp. 1-21, 2018.

[50] J. Massoud, S. Bugat, B. Marini, D. Lidbury and S. Dyck, "PERFECT - Preditction of Irradiation Damage Effects on Reactor Components: A summary," *Journal of Nuclear Materials,* vol. 406, pp. 2-6, 2010.

[51] C. Fazio, D. Briceno, M. Rieth, A. Gessi, J. Henry and L. Malerba, "Innovative materials for Gen IV systems and transmutation facilities: The cross-cutting research project GETMAT," *Nuclear Engineering and Design,* vol. 241, pp. 3514-3520, 2011.

[52] L. Malerba, M. Caturla, E. Gaganidze, C. Kaden, M. Konstantinović, P. Olsson, C. Robertson, D. Rodney, A. Ruiz-Moreno, M. Serrano, J. Aktaa, N. Anento, S. Austin, A. Bakaev, J. Balbuena, F. Bergner, F. Boioli, M. Boleininger, G. Bonny, N. Castin, J. Chapman, P. Chekhonin, M. Clozel, B. Devincre, L. Dupuy, G. Diego, D. S.L., C.-C. Fu, R. Gatti, L. Gélébart, B. Gómez-Ferrer, B. Gonçalves, C. Guerrero, P. Gueye, P. Hähner, S. Hannula, Q. Hayat, M. Hernández-Mayoral, J. Jagielski, N. Jennett, F. Jiménez, G. Kapoor, A. Kraych, T. Khvan, L. Kurpaska, A. Kuronen, N. Kvashin, O. Libera, P.-W. Ma, T. Manninen, M.-C. Marinica, S. Merino, E. Meslin, F. Mompiou, F. Mota, H. Namburi, C. Ortiz, C. Pareige, M. Prester, R. Rajakrishnan, M. Sauzay, A. Serra, I. Simonovski, F. Soisson, P. Spätig, D. Tanguy, D. Terentyev, M. Trebala, M. Trochet, A. Ulbricht, M. Vallet, K. Vogel, T. Yalchinkaya and J. Zhao, "Multiscale modelling for fusion and fission materials: The M4F project," *Nuclear Materials and Energy,* vol. 29, 2021.

[53] D. Terentyev, G. Bonny and L. Malerba, "Mobility of dislocations in thermal aged and irradiated Fe-Cr alloys," *Journal of Nuclear Materials,* Vols. 386-388, pp. 257-260, 2009.

[54] D. Terentyev, G. Bonny, C. Domain, G. Monnet and L. Malerba, "Mechanisms of radiation strengthening in Fe-Cr alloys as revealed by atomistic studies," *Journal of Nuclear Materials,* vol. 442, pp. 470-485, 2013.

[55] G. Monnet, "Multiscale modeling of irradiation hardening: Application to important nuclear materials," *Journal of Nuclear Materials,* vol. 508, pp. 609-627, 2018.

[56] K. Frydrych, "Crystal plasticity finite element simulations of the indentation test," *Computer Methods in Materials Science,* vol. 19, 2019.

[57] S. Stupkiewicz and H. Petryk, "A minimal gradient-enhancement of the classical continuum theory of crystal plasticity. Part II: Size effects," *Archives of Mechanics,* vol. 68, pp. 487-513, 2016.

[58] A. Kareer, A. Prasitthipayong, D. Krumwiede, D. Collins, P. Hosemann and S. Roberts, "An analytical method to extract irradiation hardening from nanoindentation hardness-depth curves," *Journal of Nuclear Materials,* vol. 498, pp. 274-281, 2018.

[59] T. Khvan, L. Noels, D. Terentyev, F. Dencker, D. Stauffer, U. Hangen, W. V. Renterghem, C. Chang and A. Zinovev, "High temperature nanoindentation of iron: Experimental and computational study," *Journal of Nuclear Materials,* vol. 567, p. 153815, 2022.

[60] A. Ruiz-Moreno, P. Hägner, L. Kurpaska, J. Jagielski, P. Spätig, M. Trebala, S.-P. Hannula, S. Merino, G. d. Diego, H. Namburi, O. Libera, D. Terentyev, T. Khvan, C. Heintze and N. Jennet, "Round Robin into Best Practices for the Determination of Indentation Size Effects," *Nanomaterials,* vol. 10, 2020.

[61] O. W.C. and P. G.M., "An Improved Technique for Determining Hardness and Elastic Modulus Using Load and Displacement Sensing Indentation Experiments," *Journal of Materials Research,* vol. 7, pp. 1564-1583, 1992.

[62] D. Tabor, The Hardness of Metals, New York: Oxford University Press, 1951.

[63] Bruker, "Software: ESPRIT Family," Bruker, [Online]. Available: https://www.bruker.com/en/products-and-solutions/elemental-analyzers/eds-wds-ebsd-SEM-Micro-XRF/software-esprit-family.html.

[64] M. Silva and F. Ferri, "Scanning Electron Microscopy," in *Nanocharacterization Techniques*, 2017.

[65] S. Amelinckx and J. Van Landuyt, "Encyclopedia of Physical Science and Technology," in *Encyclopedia of Physical Sceince and Technology*, 3rd ed., 2003, pp. 53-87.

[66] R. v. Mises, "Mechanik der festen Körper im plastisch-deformablen Zustand," *Mathematisch-Physikalische Klasse,* vol. 1, pp. 582-592, 1913.

[67] F. Roters, P. Eisenlohr, L. Hantcherli, D. Tjahjanto, T. Bieler and D. Raabe, "Overview of constitutive laws, kinematics, homogenization and multiscale methods in crystal plasticity finite-element modeling: Theory, experiments, applications," *Acta Materialia,* vol. 58, no. 4, pp. 1152-1211, 2010.

[68] C. Geuzaine and J. Remacle, "Gmsh: A 3-D finite element mesh generator with built-in pre- and post-processing facilities," *International Journal for Numerical Methods in Engineering,* vol. 79, pp. 1309-1331, 2009.

[69] L. Noels, "Computational & Multiscale Mechanics of Materials," Aerospace and Mechanical Engineering Department at the University of Liège, [Online]. Available: http://www.ltas-cm3.ulg.ac.be.

[70] G. Lemoine, L. Delannay, H. Idrissi, M. Colla and T. Pardoen, "Dislocation and back stress dominated viscoplasticity in freestanding sub-micron Pd films," *Acta Materialia*, vol. 111, pp. 10-21, 2016.

[71] F. Lin, M. Marteleur, P. Jacques and L. Delannay, "Transmission of {332}<113> twins across grain boundaries in a metastable β-titanium alloy," *International Journal of Plasticity*, vol. 105, pp. 195-210, 2018.

[72] U. Kocks, A. Argon and M. Ashby, Thermodynamics and kinetics of slip, Oxford: Pergamon Press, 1975.

[73] H. Frost and M. Ashby, Deformation-mechanism maps: the plasticity and creep of metals and ceramics, Oxford: Pergamon Press, 1982.

[74] F. Nabarro, "One-dimensional models of thermal activation under shear stress," *Philosophical Magazine*, vol. 83, pp. 3047-3054, 2003.

[75] J. Amodeo, S. Dancette and L. Delannay, "Atomistically-informed crystal plasticity in MgO polycrystals under pressure," *International Journal of Plasticity*, vol. 82, pp. 177-191, 2016.

[76] A. Zinovev, *Crystal plasticity modelling of thermomechanical fatigue in ITER relevant tungsten*, UCLouvain, 2019.

[77] K. Ono, "Temperature Dependence of Dispersed Barrier Hardening," *Journal of Applied Physics*, vol. 39, pp. 1803-1806, 1968.

[78] M. Beck, *Dispersed barrier hardening in irradiated metals*, Retrospective Theses and Dissertations, 1978.

[79] E. Hall, "The Deformation and Ageing of Mild Steel: III Discussion of Results," *Proceedings of the Physical Society B*, vol. 64, 1951.

[80] D. Terentyev, X. Xiao, A. Dubinko, A. Bakaeva and H. Duan, "Dislocation-mediated strain hardening in tungsten: thermo-mechanical plasticity theory and experimental validation," *Journal of the Mechanics and Physics of Solids*, vol. 85, pp. 1-15, 2015.

[81] H. Mecking and U. Kocks, "Kinetics of flow and strain-hardening," *Acta Metallurgica*, vol. 29, pp. 1865-1875, 1981.

[82] U. Kocks, "Realistic constitutive relations for metal plasticity," *Material Science and Engineering: A*, vol. 317, pp. 181-187, 2001.

[83] F. Roters, P. Eisenlohr, T. Bieler and D. Raabe, Crystal Plasticity Finite Element Methods: In Materials Science and Engineering, 2010.

[84] X. Xiao, D. Song, J. Xue, H. Chu and H. Duan, "A self-consistent plasticity theory for modeling the thermo-mechanical properties of irradiated FCC metallic polycrystals," *Journal of the Mechanics and Physics of Solids,* vol. 78, pp. 1-16, 2015.

[85] J. Dedieu, "Newton-Raphson Method," *Encyclopedia of Applied and Computational Mathematics,* pp. 1023-1028, 2015.

[86] L. Delannay, P. Jacques and S. Kalidindi, "Finite element modeling of crystal plasticity with grains shaped as truncated octahedrons," *International Journal of Plasticity,* vol. 22, pp. 1879-1898, 2006.

[87] D. Caillard, "Dynamic Strain Ageing in Iron Alloys: The Shielding Effect of Carbon," *Acta Materialia,* vol. 112, pp. 273-284, 2016.

[88] A. Van Den Beukel, "Theory of the Effect of Dynamic Strain Aging on Mechanical Properties," *Physica Status Solidi A,* vol. 30, pp. 197-206, 1975.

[89] *Metallic materials — Instrumented indentation test for hardness and materials parameters — Part 1: Test method,* International Organization for Standardization (ISO), 2015.

[90] *Standard test method for Young's modulus, tangent modulus, and chord modulus,* vol. 3.01, ASTM: Metals - Mechanical testing; Elevated and Low-temperature tests; Metallography, 2010.

[91] B. Beausir and J.-J. Fundenberger, "Analysis Tools For Electron And X-ray diffraction, ATEX - software," Université de Lorraine, 2017. [Online]. Available: www.atex-software.eu.

[92] O. Wilhelmi, R. Steve, V. L. Brandon and A. A. P. A. G. Lucille, "Focused Ion and Electron Beam Techniques," in *Handbook of Silicon Based MEMS Materials and Technologies,* Micro and Nano Technologies, 2010, pp. 323-325.

[93] J. Adams, D. Agosta and R. Leisure, "Elastic constants of monocrystal iron from 3 to 500K," *Journal of the Applied Physics,* vol. 100, p. 113530, 2006.

[94] D. W.P., "Presicion measurements of the lattice constants of twelve common metals," *Physical Reviews,* vol. 25, pp. 753-761, 1925.

[95] K. Okazaki, "Solid-solution hardening and softening in binary iron alloys," *Journal of Material Sciences,* vol. 31, pp. 1087-1099, 1996.

[96] H. Khater, G. Monnet, D. Terentyev and A. Serra, "Dislocation glide in Fe–carbon solid solution: from atomistic to continuum level description," *International Journal of Plasticity,* vol. 62, pp. 34-49, 2014.

[97] G. Deng, A. Tieu, L. Su, H. Zhu, Q. Zhu, W. Zamri and C. Kong, "Characterizing deformation behaviour of an oxidized high speed steel: Effects of nanoindentation depth, friction and oxide scale porosity Effects of nanoindentation depth, friction and oxide scale porosity," *International Journal of Mechanical Sciences,* vol. 155, pp. 267-285, 2019.

[98] T. Wang, T.-H. Fang and Y.-C. Lin, "A numerical study of factors affecting the characterization of nanoindentation on silicon," *Materials Science & Engineering A,* vol. 447, pp. 244-253, 2007.

[99] J. Krier and J. Breuils, "Introduction of the real tip defect of Berkovich indenter to reproduce with FEM nanoindentation test at shallow penetration depth," *Journal of Materials Research,* vol. 27, pp. 28-38, 2012.

[100] F. Zhang, Y. Huang and K.-C. Hwang, "The indenter tip radius effect in micro- and nanoindentation hardness experiments," *Acta Mechanica Sinica,* vol. 22, pp. 1-8, 2006.

[101] A. Diwo, "Manufacture of Rolled Plates, Thicknesses of 1mm-8mm-10mm-12mm-16mm-20mm-25mm-25mm-32mm-35mm-48mm and Billet Material 100mm squared, made from Reduced Activation F/M Steel Type 9 CrWTaV (Eurofer 97-3) for TBM Fabrication Technology Trials and Mock-ups," Saarschmiede GmbH Freiformschmiede, Völklingen, 2009.

[102] Böhler Edelstahl,, *Inspection Certificate 029060,* 1999.

[103] M. Matijasevic, E. Lucon and A. Almazouzi, "Behavior of ferritic/martensitic steels after n-irradiation at 200 and 300°C," *Journal of Nuclear Materials,* vol. 377, no. 1, pp. 101-108, 2008.

[104] A. E8/E8M-22, *Standard Test Methods for Tension Testing of Metallic Materials,* 2022.

[105] E. Lucon and W. Vanermeulen, "Overview of the tensile properties of EUROFER in the unirradiated and irradiated conditions," *Journal of Nuclear Materials,* Vols. 386-388, pp. 254-256, 2009.

[106] E. Lucon, R. Chaouadi and M. Decreton, "Mechanical properties of the European reference RAFM steel (EUROFER97) before and after irradiation at 300C," *Journal of Nuclear Materials,* Vols. 329-333, pp. 1078-1082, 2004.

[107] Z. Fan, G. Velisa, K. Jin, M. Crespillo, H. Bei, W. Weber and Z. Y., "Temperature-dependent defect accumulation and evolution in Ni-irradiated NiFe concentrated solid-solution alloy," *Journal of Nuclear Materials,* vol. 519, pp. 1-9, 2019.

[108] T. Simm, L. Sun, S. McAdam, P. Hill, M. Rawson and K. Perkins, "The Influence of Lath, Block and Prior Austenite," *Materials,* vol. 10, no. 7, 2017.

[109] Bruker, "Software: ESPRIT Family," Bruker, [Online]. Available: https://www.bruker.com/en/products-and-solutions/elemental-analyzers/eds-wds-ebsd-SEM-Micro-XRF/software-esprit-family.html.

[110] T. Byun and K. Farrel, "Irradiation hardening behavior of polycrystalline metals after low temperature irradiation," *Journal of Nuclear Materials,* vol. 326, pp. 86-96, 2004.

[111] M. Grossbeck, "1.04 - Effect of Radiation and Strength and Ductility of Metals and Alloys," *Materials Science and Materials Engineering,* vol. 1, pp. 99-122, 2012.

[112] T. Zhang, C. Vieh, K. Wang and Y. Dai, "Irradiation-induced evolution of mechanical properties and microstructure of Eurofer 97," *Journal of Nuclear Materials,* vol. 450, pp. 48-53, 2014.

[113] F. Bergner, C. Kaden, A. Das, S. Merino, G. Diego and P. Hähner, "Nanoindentation applied to ion-irradiated and neutron-irradiated Fe-9Cr and Fe-9Cr-NiSiP model alloys," *Journal of Applied Physics,* vol. 132, 2022.

[114] W. Nix and H. Gao, "Indentation size effects in crystalline materials: a law for strain gradient plasticity," *Journal of the Mechanics and Physics of Solids,* vol. 46, pp. 411-425, 1998.

[115] A. Ruiz-Moreno and P. Hähner, "Indentation size effects of ferritic/martensitic steels: A comparative experimental and modelling study," *Materials & Design,* vol. 145, pp. 168-180, 2018.

[116] "POLONEZ BIS 3," National Science Centre in Poland, 15 September 2022. [Online]. Available: https://www.ncn.gov.pl/en/ogloszenia/konkursy/polonez-bis3.

[117] H. Edelsbrunner and R. Seidel, "Voronoi diagrams and arrangements," *Discrete & Computational Geometry,* vol. 1, pp. 25-44, 1986.

[118] "Interpreting the Diffraction Pattern," Oxford Instruments, [Online]. Available: https://www.ebsd.com/ebsd-explained/interpreting-the-diffraction-pattern.

Appendix 1. Pollycrystalline specimen box

Within the project, an attempt to simulate polycrystalline geometry has been made. However, as has been mentioned several times throughout the presented manuscript, strain gradient theory is not presented in the applied computational analysis. Therefore, the phenomenon of characteristic length or GNDs is simply absent in the model, consequently making the variative grains in terms of their geometrical size and shapes pointless. Nevertheless, this is an interesting development, which can be applied after solving the above-mentioned problem.

A 2D grain map has been created using Voronoi tessellation [117] with the chosen average grain size of 17 μm, which is somewhat between the average block size (8 μm) and the minimal PAG size (30 μm) in Eurofer97 according to the EBSD map presented in Figure 57 (or Figure 83). Then a 3D sample box of dimensions 100 × 100 × 50 μm^3 has been then established by extruding the 2D plane along the *z* axis on 20 μm twice, thus keeping the grain depth relative to the grain size. A one-grain layer extruded on 10 μm is finishing this composition to lower the CPU time, as no deformation is expected there anyway. These simplifications allowed the use of this geometry to simulate polycrystalline simulations, without allocation of a significant amount of time and efforts oriented toward better physical representation. The FEM setup obtained is presented in Figure 82.

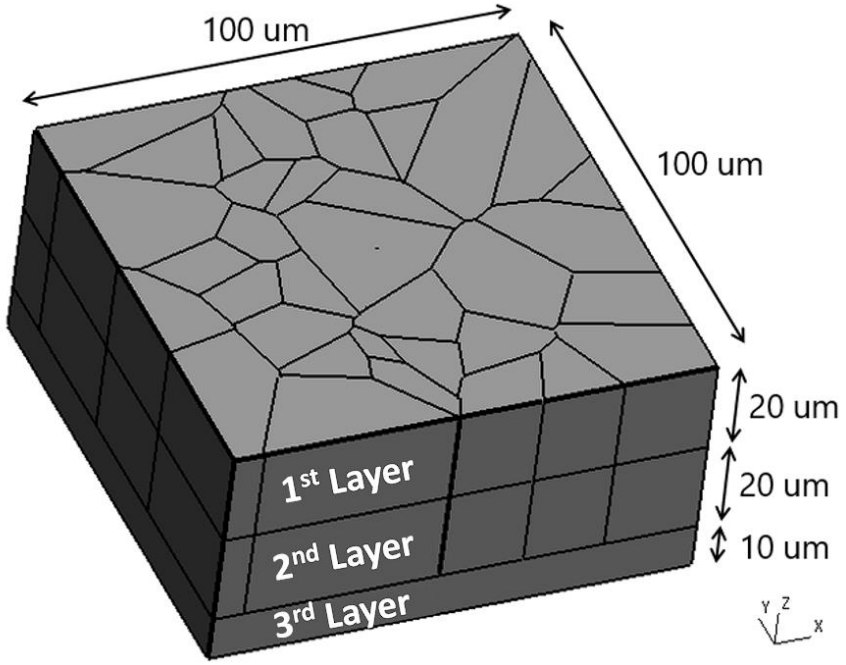

Figure 82. FEM geometry of the polycrystalline Eurofer97 specimen.

In Figure 83 the EBSD IPZF grain map of Eurofer97 (15º misorientation angle i.e. blocks) is compared to the FEM polycrystalline plane created by Voronoi tessellation. Some grains of the FEM geometry might seem larger than the real ones. This is because the chosen misorientation angle of the EBSD map is not high enough to see prior austenite grains.

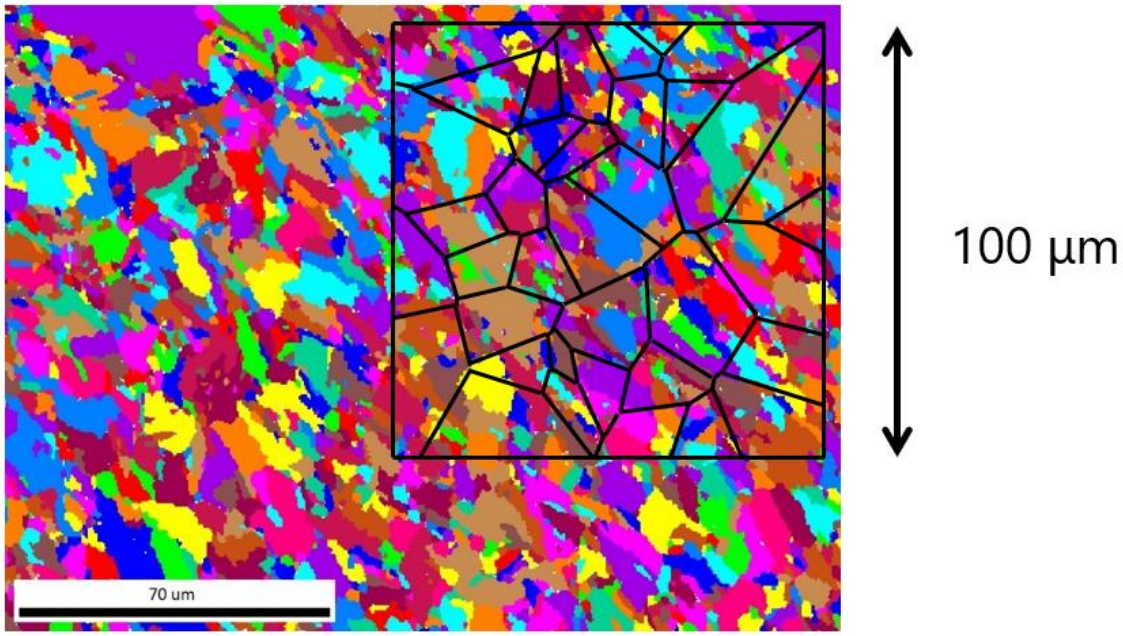

Figure 83. Comparison of the FEM geometry grain size and the EBSD map with 8 µm blocks.

Grain orientations for the FEM setup were randomly selected for each layer. The single grain representing Layer 3 in Figure 82 was set as [100]. The indenter is placed in the center of the surface. The indented grain in the center of Layer 1 was set as [101]. The surface grain orientations map is presented in Figure 84.

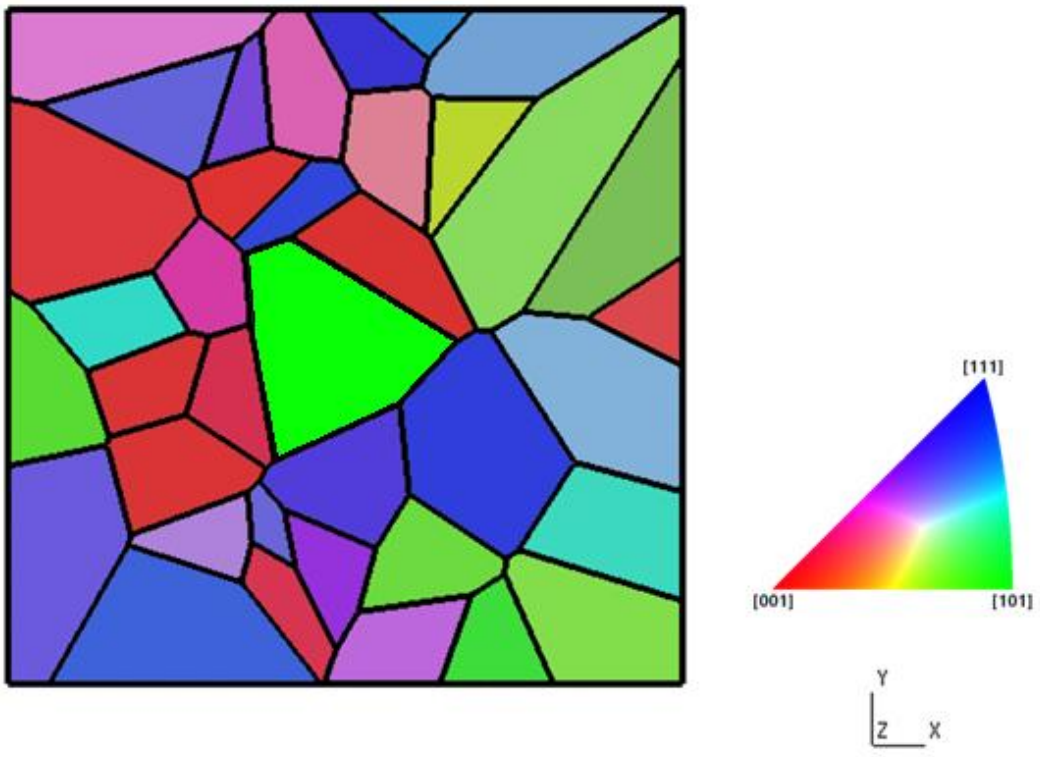

Figure 84. The surface grain orientations map in FEM.

The mesh was finely refined in the indenter contact area and roughly at the junctions of the grain boundaries, as can be seen in Figure 85. Overall, it consists of 114191 tetrahedral 1st-order elements.

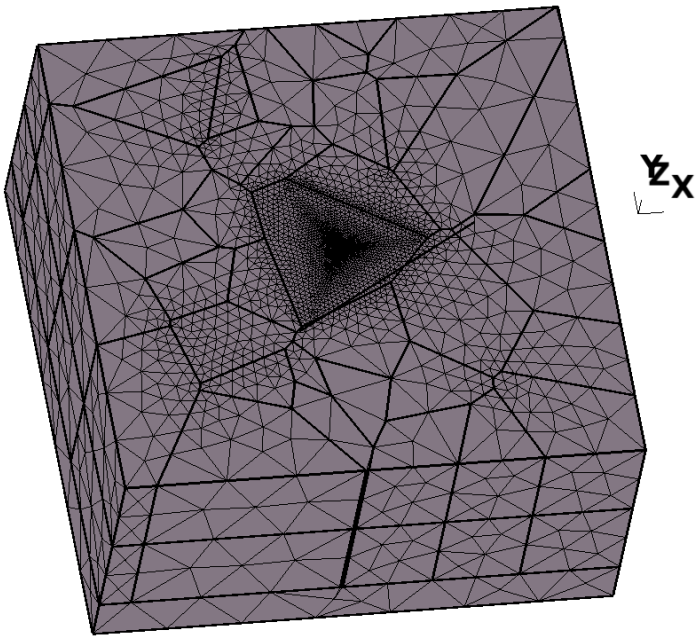

Figure 85. Meshed polycrystalline specimen box.

Indentation has been performed to h_{max} = 1.25 µm at room temperature which corresponds to the experiments presented in §4.2.3.1. The material law and subsurface geometry represent non-irradiated material. The obtained force-displacement curves are compared in Figure 86 with the corresponding simulations performed on the single crystal geometry previously presented in Figure 73(a). It should be noted that the single crystal specimen box has lower dimensions of 50 × 50 × 13 µm^3.

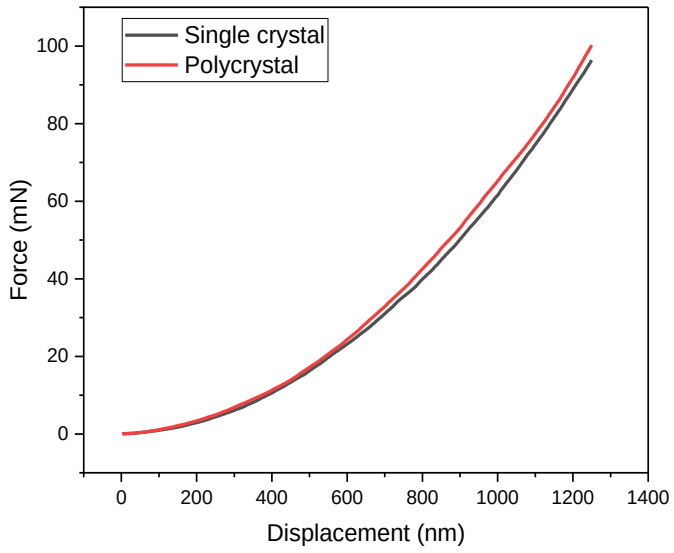

Figure 86. Force-displacement curves of the simulated nanoindentation process in single crystal (black) and polycrystal (red) Eurofer97.

Figure 86 clearly shows the negligible effect of the introduction of grains. The difference at h_{max} does not exceed 4% and comes from incompatibilities of grain orientations (i.e. slip systems misorientations) throughout the specimen. Therefore, it cannot represent the presence of the strain gradients in front of the grain boundaries, explaining the Hall-Petch effect, which would require implementing strain gradient crystal plasticity. The FEM stress and deformation maps are analyzed in Figure 87 and Figure 88.

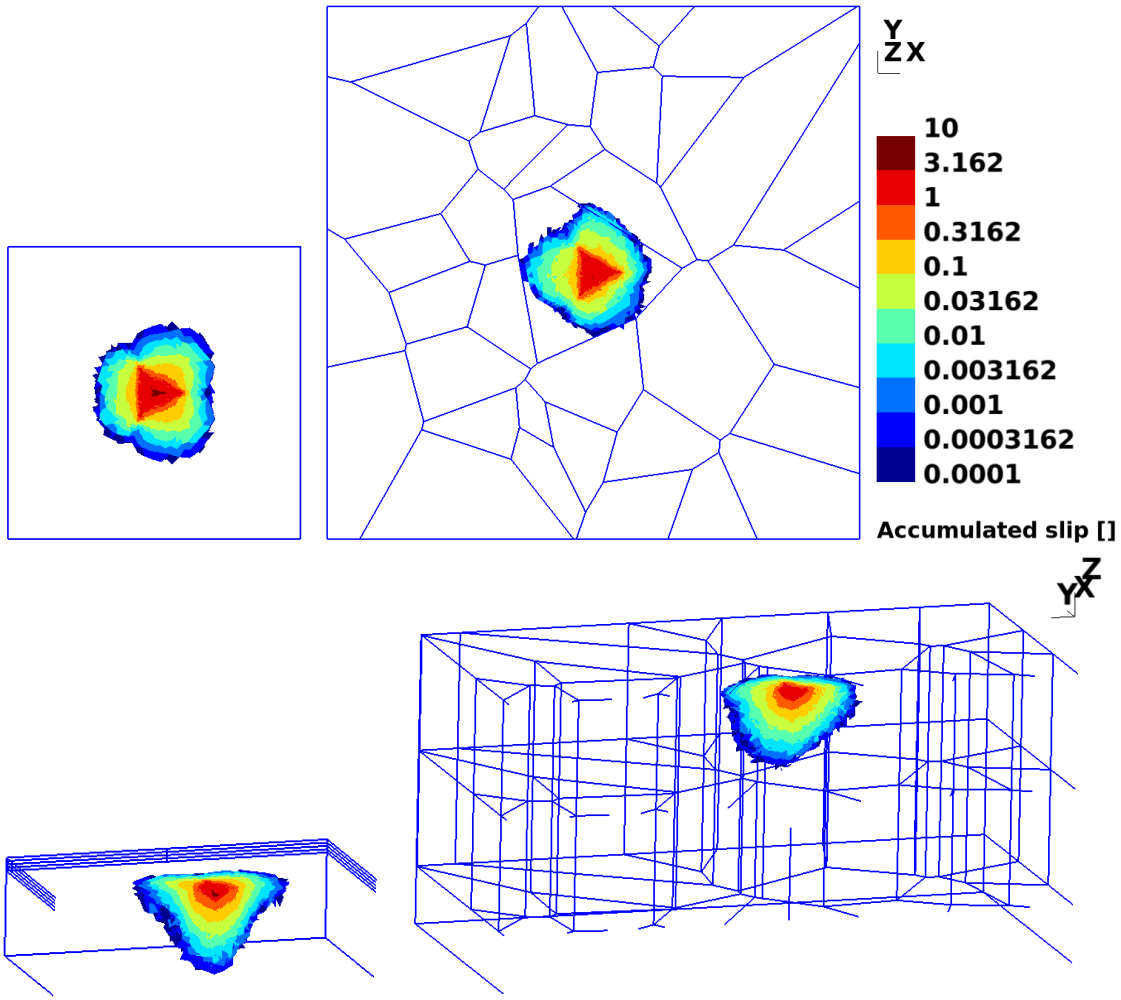

Figure 87. Accumulated slip FEM maps of single crystal and polycrystal geometries. All figures are taken at h = 1250 nm.

In any case, one can see in Figure 87 how misorientations of slip systems in different grains may lead to the changes in the distribution of deformation patterns. While it is evenly distributed and even shows some symmetry when observed from the surface plane in the single crystal, the polycrystal distribution is slightly suppressed along depth and randomly distorted in the whole shape. The effect of the adjacent grains is clearly observed.

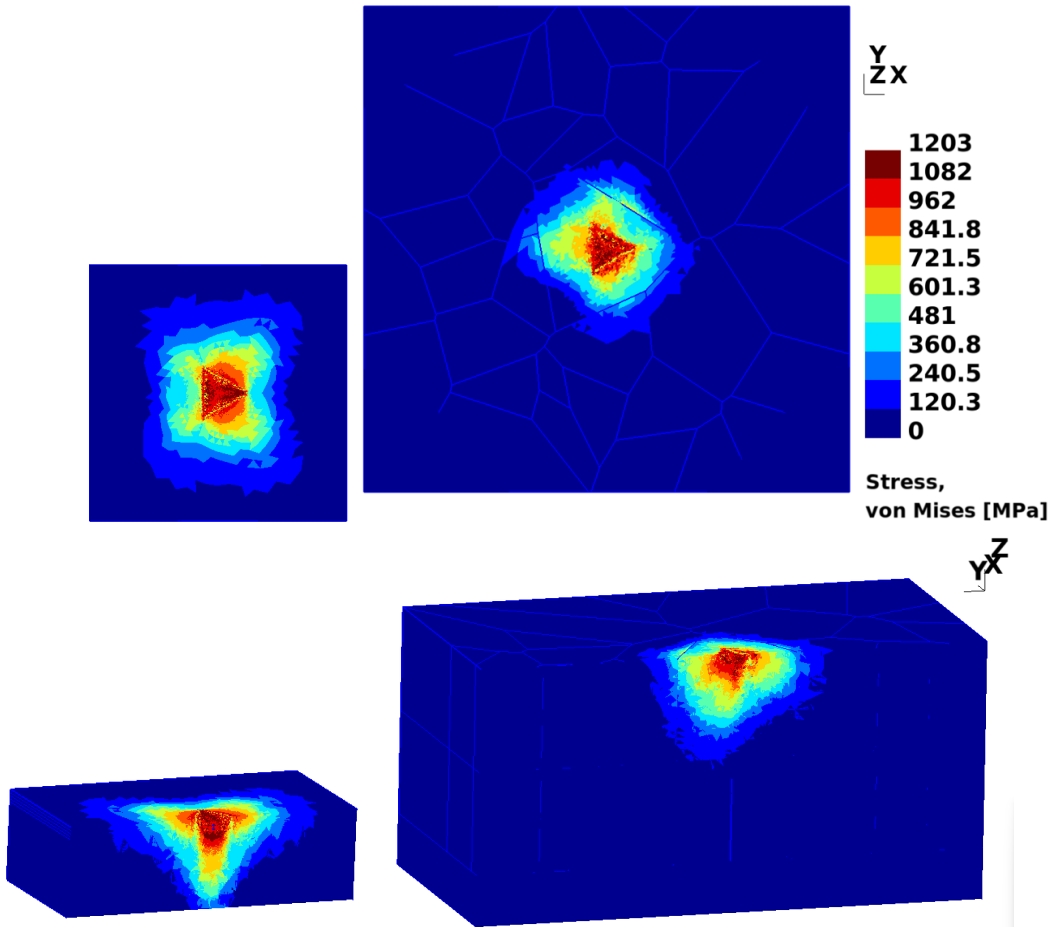

Figure 88. Equivalent stress FEM maps of single crystal and polycrystal geometries. All figures are taken at h = 1250 nm.

The stress profiles show the same behavior as the accumulated slip, which can be seen in Figure 88. Once again, the patterns are affected by the adjacent grains, which makes their distribution uneven.